Transport and deposition of inertial particles in a fracture with periodic corrugation

Tatiana Nizkaya

THÈSE

présentée et soutenue publiquement le 01/10/2012 en vue de l'obtention du grade de

Docteur de l'université de Lorraine

Intitulé: Mécanique - Génie Civil

par

Nizkaya Tatiana

"Transport and deposition of inertial particles in a fracture with periodic corrugation"

Jury:

H. Auradou (FAST - Université Paris sud, rapporteur)

F. Plouraboué (IMFT - Université de Toulouse, rapporteur)

J. Dusek (IMFSS - Université de Strasbourg, president)

JR. Angilella (LAEGO - Université de Lorraine, co-directeur)

M. Buès (LAEGO - Université de Lorraine, directeur).

Nancy, October 2012

To the memory of my father.

Acknowlegements

I would like to thank my supervisor Prof. Michel Buès for accepting and welcoming me at LaEGO with such a rich and interesting research topic. Also, I am endlessly grateful to my co-supervisor Dr. Jean-Régis Angilella for his guidance throughout these years, for all the inspirational discussions and thoughtful advices - but also for his wisdom and patience. Without his support and encouragement and this work could have not been finished.

I wish to thank Dr. Harold Auradou and Prof. Frank Plouraboué for accepting to review this thesis. I highly appreciate the interest and attention they paid to this work, their very valuable comments and their encouraging feedback. I am also grateful to Prof. Jan Dusek for presiding in the jury and raising some interesting questions during the defence.

Many thanks to my fellow PhD students and all the LaEGO team for their company and optimism, which created a nice working ambience.

Finally, I would like to thank my boyfriend Mike Tamm for his unconditional love and understanding - and for making things fun! The support of my family was also very important, despite the distance.

Abstract

It is well-known that inertial particles tend to focus on preferential trajectories in periodic flows. The goal of this thesis was to study the joint effect of particle focusing and sedimentation on their transport through a model 2D fracture with a periodic corrugation.

First, single-phase flow though the fracture has been considered: the classical results of the inertial lubrication theory are revisited in order to include asymmetric fracture geometries. Cubic corrections to Darcy's law have been found analytically and expressed in terms of two geometric factors, describing channel geometry.

For weakly-inertial particles in a horizontal channel it has been shown that, when inertia is strong enough to balance out the gravity forces, particles focus to some attracting trajectory inside the channel. The full trapping diagram is obtained, that predicts the existence of such attracting trajectory regime depending on the Froude number and on geometric factors. Numerical simulations confirm the asymptotic results for particles with small response times.

The influence of the lift force on particle migration has also been studied. In a vertical channel the lift is induced by gravity and leads to complex trapping diagrams. In the absence of gravity the lift is caused by inertial lead/lag of particles and can lead to chaotic particle dynamics.

Finally, for dust particles in a vortex pair it has been shown that particles can be trapped into one or two equilibrium points in a reference frame rotating with the vortices. A full trapping diagram has been obtained, showing that any pair of vortices can trap particles, independently of their strength ratio and the direction of rotation.

Résumé court

Il est bien connu que les particules inertielles dans un écoulement périodique ont tendance à se focaliser sur des trajectoires privilégiées. Le but de ce travail de thèse est d'étudier l'influence de cette focalisation sur le transport et la sédimentation de particules dans une fracture plane à rugosité périodique.

Tout d'abord, un écoulement monophasique dans une fracture est analysé asymptotiquement dans le cas de faible rugosité. Les résultats classiques de la théorie de la lubrification inertielle sont généralisés au cas de fractures avec des parois asymétriques. Les corrections non linéaires à la loi de Darcy sont calculées explicitement en fonction des facteurs géométriques de la fracture.

Le transport de particules dans une fracture horizontal est étudié asymptotiquement dans le cas de particules de faible inertie. Les particules se focalisent sur une trajectoire attractrice, si le débit d'écoulement est assez fort par rapport à la gravité. Un diagramme complet de focalisation a été obtenu, qui prédit l'existence de l'attracteur en fonction du nombre de Froude et des facteurs géométriques de la fracture. Les paramètres quantitatifs du transport ont été calculés également. L'influence de la force de portance sur la migration de particules a été étudiée également. Dans un canal vertical, la portance (provoquée par la gravité) modifie le nombre d'attracteurs et leurs positions. En absence de gravité, la portance peut provoquer une dynamique chaotique des particules.

En outre, le captage des particules par une paire de tourbillons a été étudié. Le diagramme d'accumulation obtenu démontre que toute paire de tourbillons peut être un piège à particules.

Contents

List of principal symbols

Length, time and velocity scales:

L_∞ length of the channel

L_0 period of corrugation

H_0 mean gap of the channel

A_0 average corrugation amplitude

a particle radius

U_0 mean flow velocity

T_0 hydrodynamic time

Physical properties:

ρ_f density of the fluid

ρ_p density of the particle

ν kinematic viscosity of the fluid

μ dynamic viscosity of the fluid

$\vec{g}$ gravity acceleration

Channel geometry:

$\phi_{1,2}(x)$ wall shapes

$h(x)$ half-aperture of the channel

$\phi(x)$ middle line of the channel

$\eta(x, z)$ cross-channel variable

$J_h, J_{\phi h}, J_\phi$ shape factors

$\beta = J_h/J_{\phi h}$ corrugation asymmetry factor

Non-dimensional numbers:

$\varepsilon = H_0/L_0$	channel aspect ratio (small parameter)
$\delta_0 = A_0/L_0$	non-dimensional corrugation
$R = \dfrac{2\rho_f}{2\rho_p + \rho_f}$	fluid/particle density ratio
$\mathrm{Re}_H = \dfrac{U_0 H_0}{\nu}$	Reynolds number of the channel
$\mathrm{Fr} = \dfrac{U_0^2}{L_0 g}$	Froude number
$G = \mathrm{Fr}^{-1}$	inverse Froude number
$\mathrm{St} = \dfrac{2\varepsilon \mathrm{Re}_H}{9}\left(\dfrac{a}{H_0}\right)^2$	Stokes number of the particle
$\tau = \dfrac{\mathrm{St}}{R}$	particle response time (small parameter)

Fluid and particle velocities:

$\psi(x,z)$	fluid streamfunction
$\vec{x}_p(t)$	particle position
$\vec{u}_f(\vec{x})$	fluid velocity field
$\vec{v}_p(t) = \dot{\vec{x}}_p$	particle velocity
$\vec{v}_s(t) = \dot{\vec{x}}_p - \vec{u}_f(\vec{x}_p)$	particle slip velocity
$\vec{v}_\tau(\vec{x})$	asymptotic particle velocity field
η_k	cross-channel coordinate of particle at the end of k-th corrugation period
$f(\eta_k) = \eta_{k+1} - \eta_k$	migration function (Poincaré map)

Chapter 1

Introduction

1.1 Inertial particles in earth sciences

Inertial particles can be found everywhere in natural and industrial flows: examples include dust, sand, clouds, plankton, air pollutants and sprays. Modeling such particle-laden flows is an important task in either fundamental and applied sciences. In most cases the particle velocity is not exactly equal to the local fluid velocity because of their finite mass and finite size. Therefore, their behavior can be very different from one of the tracers, that are simply advected by the flow, and prediction of their transport properties is a challenging task.

One of the most important features of inertial particles is their tendency to cluster in well-defined zones of the flow domain, leading to large local concentrations, as well as large collision and aggregation rates. This clustering effect can occur in all types of flows (confined and open, laminar and turbulent), but can take very different forms.

For example, one of the hypotheses explaining planet formation in accretion disks is trapping of dust by vortical structures. Indeed, it has been shown that the gravity force alone is not sufficient to initiate the formation of planetesimals [5][63][13], and that the hydrodynamics must play an important role in this process. Another example is clustering of droplets in a turbulent cloud that can enhance their coalescence and accelerate rain initiation (see, for example [71], [21] and others). Also, it is known that clustering of particles in turbulent flows can play an important role in pneumatic transport and powder

engineering [61]. Clustering of inertial particles affects their transport properties: the fact that particles accumulate on preferential trajectories can make them travel faster (or slower) than the single phase flow. In addition, this can also modify particle sedimentation velocity [42].

In geoscience, many flows through fractures carry tiny inertial particles like rock sediments or organic debris. In this case also, the finite size of the particles can affect the transport of these sediments. Even if the particles are non-brownian and much smaller than the gap of the channel, they can have complex dynamics leading to different regimes of transport and sedimentation. This thesis is devoted to the analysis of these regimes, in order to understand under which conditions long-term transport or deposition can occur. Following a previous thesis by S. Crosnier [16], we consider a model fracture with periodic corrugations.

1.2 Understanding particle clustering

To understand the mechanisms that lead to the complex behavior of inertial particles one often compares the kinematics of tracers and the dynamics of inertial particles (see, for example, the review paper by Cartwright *et al.* [12]).

Tracer particles are described by simple advection and (possibly) brownian diffusion[1]:

$$
\frac{d}{dt}\vec{x}_p(t) = \vec{u}_f(\vec{x}_p(t), t) + \vec{w}(t),
$$
$$
\vec{x}_p(0) = \vec{x}_0.
$$

(1.1)

where $\vec{u}_f(\vec{x}_p(t), t)$ is the fluid velocity field at the position of the tracer $\vec{x}_p(t)$ and $\vec{w}(t)$ are random fluctuations of the velocity. The divergence of the tracer velocity field is always zero in the incompressible flow: such particles never cluster. Moreover, tracers can collide only because of brownian diffusion: in the deterministic limit (when $\vec{w}(t) = 0$) particle trajectories never intersect.

An *inertial particle* has its own velocity $\vec{v}_p$ different from that of the fluid and is

---

[1]All the equations used in the examples of this section are written in non-dimensional variables based on some typical legth and velocity scales.

governed by a second-order motion equation of the form:

$$\begin{aligned}
\frac{d\vec{x}_p(t)}{dt} &= \vec{v}_p, \\
\frac{d\vec{v}_p(t)}{dt} &= -\frac{1}{\text{St}}\left(\vec{v}_p(t) - \vec{u}_f(\vec{x}_p(t))\right) + \vec{f}_1(\vec{x}_p, \vec{v}_p, t),
\end{aligned} \tag{1.2}$$

where St is a non-dimensional number measuring particle inertia, the term proportional to $\vec{v}_p - \vec{u}_f$ is the Stokes drag and $\vec{f}_1$ incorporates gravity and various other forces.

Equation (1.2) is a dynamical system in the 6D phase space of particle positions and velocities. Because of the drag, the divergence of the right-hand side of Eq. (1.2) is always negative. As a consequence, volumes of inertial particles in the 6D phase space shrink and, if the phase space is bounded, particles will converge to an attractor (see Fig. 1.1). This attractor is a manifold in this 6D position-velocity phase space, and can have different dimensions and structure depending on the flow and on the particle Stokes number St[2].
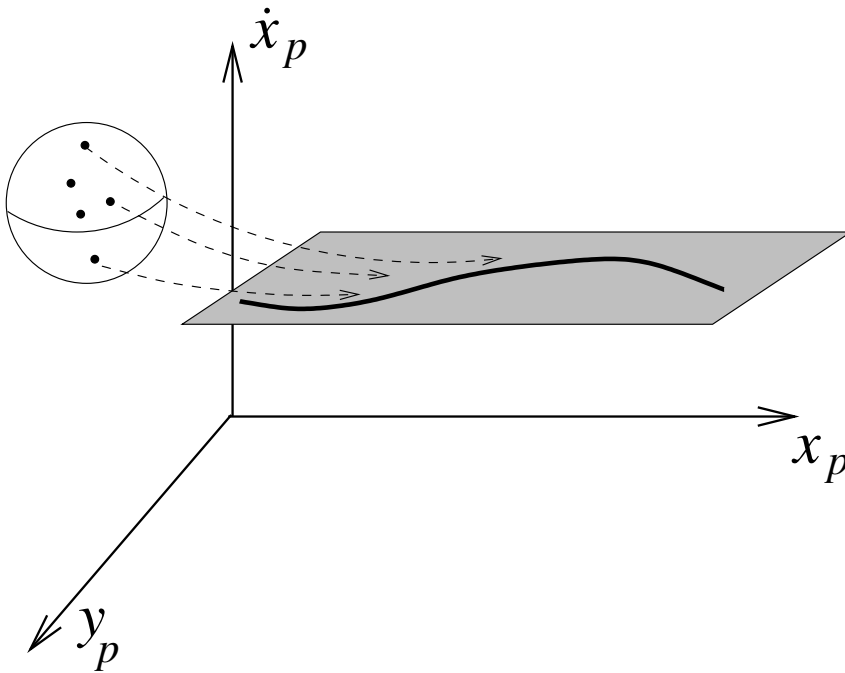
Figure 1.1: *The first mechanism: shrinking of phase volumes leading to accumulation of particles on the attractor.*

For larger St there is an additional effect (described by Falkovich *et al.* [21]) that can also lead to high particle concentrations and large collision rates. This effect is due

---

[2]Note that the attractor is not always visible in the physical space.

to the fact that trajectories of inertial particles (solutions of Eq. (1.2)) can intersect (i.e. two particles can occupy the same position with different velocities). This can lead to the appearance of "caustics" in the particle velocity field [70]. These caustics are formed by fronts of particles with different velocities that cross each other. The existence of such caustics does not require long-living clusters of particles in the physical space, but leads to very high collision rates.

A possible physical explanation for caustic formation is the interaction of particles with the vortical structures of the flow. At small St this leads to accumulation of heavy particles in the regions of small vorticity of the flow. For high St this leads to the appearance of the "slingshot effect" (described by Falkovich *et al.* [21]): a particle with high inertia is ejected from the vortical zones with a velocity that is cross-stream to other particles in the flow, which results in high collision rates (see Fig. 1.2).
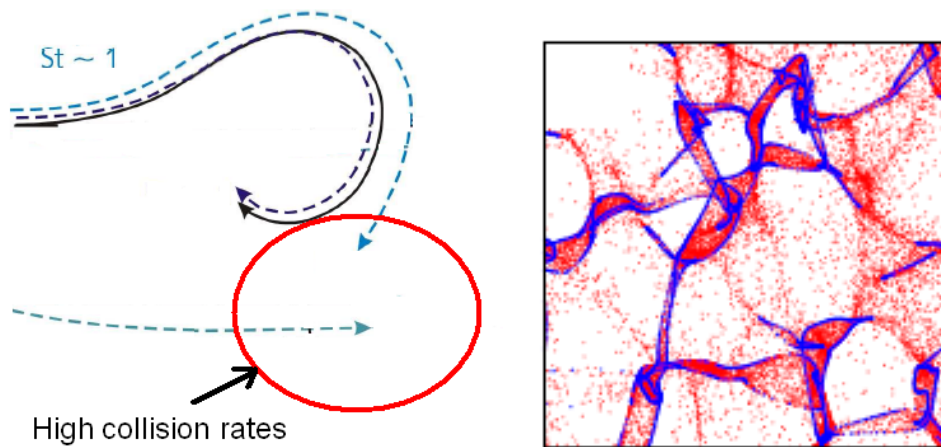
Figure 1.2: *The second mechanism: "slingshot" effect and caustics (simulations taken from Wilkinson and Mehlig [70]).*

In open flows or open domains the existence of the attractor is not guaranteed by the dissipative dynamics of Eq. (1.2), because the phase space is not bounded (particles can be centrifuged away to infinity). However, some studies of such flows (see Vilela & Motter [69], Peng & Dabiri [53]) have shown that attractors do exist in these cases and can lead to effective particle trapping. (This process is probably used by jellyfishes to capture plankton [53].)

1.3 Particle clustering in periodic channels

In flows through corrugated channels the clustering effect is most visible when the corrugation has a periodic structure. In this case the particle attractor always exists (for the reasons described above) and can take the form of an attracting trajectory. Some (or all) particles in the flow can focus on this trajectory, forming a compact beam.

1.3.1 Focusing effect in periodic channels

Historically, the first studies of particle clustering appeared in aerosol science, where this effect has important technical applications (it is used to create thin aerosol beams and filter particles from the air [17]). In aerosol-focusing devices a particle-laden flow runs through a convergent/divergent nozzle (or a succession of such nozzles), which makes particles focus to the center. Particle trajectories can be forced to intersect after only one nozzle (supercritical focusing forming a caustic) or to form a compact beam after many periods of acceleration/deceleration (focusing to an attractor due to periodicity of the flow). This effect was first studied theoretically in the 1950's by Robinson [55] and later by Israel & Friedlander [35] (and others, see Vainshtein *et al.* [66], Fernandez de la Mora [24] to name but a few). These authors found that different regimes of aerosol focusing are possible depending on the particle Stokes number St: for small St particles converge to the center uniformly, for larger St they can cross the center line several times.

The focusing behaviors described above are visible also when particles have densities comparable to that of the fluid. This was studied in a series of work by Maxey and his co-authors (Maxey & Corrsin [43], Rubin *et al.* [56], Maxey [42]), based on periodic cellular flows. They showed that both particles lighter and heavier that the fluid can focus to attracting trajectories (focusing is possible not only for aerosols). Therefore, we can expect the same focusing effect to occur for sediments in water flow through a periodic fracture.

1.3.2   Lift-induced particle migration

In channel flows there is an additional focusing mechanism, due to the hydrodynamic interaction of the particle with the shear flow and the walls (called the inertial[3] lift force).

Interaction of the disturbance flow (flow induced by the particle) with a channel wall creates a force (wall-induced inertial lift) that pushes particles away from the wall. A similar force results from interaction of the disturbance with the shear flow itself (shear-induced inertial lift). The direction of this latter depends on the slip velocity of the particle (particles leading the fluid are pushed to the walls and particle lagging the fluid are pushed to the center). In a channel with straight walls these forces are balanced out at some distance from the wall and make all particles focus to this equilibrium position[4].

This effect was first studied in the 1960's by Segré and Silberberg [59] for particles moving in a straight tube or radius R. They observed that neutrally-buoyant particles focus at a fixed distance $r = 0.62R$ from the center of the channel, forming a pinched ring. Later, lift-induced focusing in straight channel has been studied by many authors both theoretically (using asymptotic methods, see Ho & Leal [32], Hogg [33], Asmolov [3] and others), numerically (using direct numerical simulations [14], [15]) and experimentally [40].

In straight channels the lift force is the only cause of focusing: proper inertia of the particle is unimportant. However, in curved channels there is a combined effect of fluid and particle inertia that can lead to some non-trivial behavior. In particular, under the combined effect of lift and particle inertia, hydrodynamic sorting of particles (depending on their density) is possible. This sorting effect is the principal idea of inertial microfluidic devices, which have been developing rapidly in the past five years (see the works by Di Carlo *et al.* [18], Gossett and Di Carlo [28]).

This motivated the calculations of Chapter 4 of this thesis, where the lift force is taken into account.

---

[3]This force is indeed due to inertia: not of the particle itself, but of the fluid disturbed by the particle in its motion.

[4]In terms of the dynamical system Eq. (1.2) we can say that the lift force (hidden in the $\vec{f_1}$ term of Eq. (1.2)) affects the shape of the attractor in the 6D phase space of particle dynamics, making it visible in the physical space.

1.4 Particle-laden flows in corrugated fractures

Natural fractures have a complex geometry: they can be described by random fractal self-affine surfaces [8], [54]. This makes modeling fracture flows a challenging task, even if the flow equations are solved numerically. The principal problem is that the exact geometry of the fracture is unknown: it is difficult to measure and, most importantly, it changes from sample to sample [9]. The ultimate task is, therefore, to construct a theoretical model that would connect macroscopic transport properties of a fracture with some statistical properties describing its geometry [36].

In this thesis we study theoretically particle-laden flow in a very simple model fracture: a thin two-dimensional channel with smooth wall corrugations. However we try to stay in the spirit of studies mentioned above and express the macroscopic transport properties (non-Darcian corrections to the flow rate curves, particle focusing rates and deposition lengths) in terms of averaged factors describing the geometry of the fracture.

1.4.1 Non-Darcian effects in corrugated fractures

Fluid flow through rough fractures has always been an important topic in hydrogeology and related applications. The focus of interest in such studies is the relation between the (volumetric) flow rate Q through the fracture and the pressure drop ΔP applied at its ends:

$$Q = -\frac{KS}{\mu}\frac{\Delta P}{L_\infty},\tag{1.3}$$

where μ is the dynamic viscosity of the fluid, L_∞ is the length of the fracture, S is the area of its cross-section and K is the *hydrodynamic permeability* of the fracture (for fractures with plane parallel walls and gap H_0 we have $K = H_0^2/12$). For small flow rates permeability depends only on fracture geometry and the relation (1.3) is linear in Q.

Real $Q(\Delta P)$ curves, measured in experiments, deviate from the linear Darcy law as flow rates increase. These deviations appear long before the transition to turbulence and are due to the inertia of the fluid and wall corrugations. Analyses of experimental data (see, for example, [25]) reveal two non-darcian regimes depending on the Reynolds number $\mathrm{Re}_H = \dfrac{U_0 H_0}{\nu}$, where $U_0 = Q/S$ is the mean flow velocity. For small Re_H, when

inertial and viscous forces are of the same order of magnitude, deviations from Darcy law are cubic in Q. This regime is quite well understood now and its cubic nature is confirmed theoretically (see works of Mei and Auriault [47], Firdaouss *et al.* [25], Jacono *et al.* [36]).

For larger flow rates, when fluid inertia is dominant, experimental data suggests that deviations from Darcy's law are quadratic in Q (Forchheimer regime [26]). This quadratic[5] term is due to the appearance of the recirculation zones in the flow and to additional dissipation of energy in these zones. However, the physical mechanism of such dissipation is not completely understood yet. One of the possible explanations is given by Panfilov *et al.* [52] (see also Lucas *et al.* [39]). It consists in the fact that, in presence of geometrical singularities, single fluid jets can penetrate the separatrix between the core flow and the recirculation zone, and lose their kinetic energy in this zone. These complex effects are out of the scope of the thesis.

In this thesis we consider flows though thin channels with small and moderate Reynolds numbers, always staying in the first cubic zone. In Chapter 2 we will find the cubic corrections to Darcy's law for arbitrary (smooth) wall shapes and express them in terms of some integral factors, that describe the channel geometry.

1.4.2 Particle transport in corrugated fractures

For particle-laden flows, macroscopic behavior is described by the breakthrough curves of the particulate phase. Experiments show that these breakthrough curves for finite-size particles differ from those for passive tracers [50][51]. In particular, in some cases particles seem to propagate in the fracture faster than the fluid. A possible explanation of this effect consists in a combined effect of advection and brownian diffusion of particles, which leads to redistribution of particles over the cross-section of the channel (Taylor dispersion [64]). However, this mechanism does not work for macroscopic particles, which are not sensitive to brownian motion.

In this thesis we show (in a very simple fracture geometry) that particle inertia can

---

[5]To be more precise, this term is proportional to $|Q|Q$ and not to Q^2, because in an isotropic fracture the change of flow direction (sign of Q) should not modify the flow rate curve.

also lead to redistribution of particles across the channel and, therefore, to apparent acceleration or deceleration of particles relatively to the flow.

1.5 Outline of the thesis

The aim of this thesis is therefore to study the effect of inertial focusing on particle transport in a thin 2D corrugated channel. The thesis consists of six chapters. Chapter 2 is devoted to a single-phase flow in a thin channel with periodic corrugations. It follows closely the classical works of inertial lubrication theory, but generalizes the previous results to arbitrary wall shapes. In Chapter 3, the motion of weakly-inertial particles in this flow is studied using an asymptotic form of the Maxey-Riley equations. The main tool used in this chapter is the Poincaré map of particle positions at the end of corrugation periods, which contains all information on long-term particle behavior. Chapter 4 is devoted to particle migration driven by the lift force. Particle behavior at finite Stokes numbers (attractor splitting in Maxey-Riley dynamics and transition to chaos induced by the lift force) is considered in special sections within Chapters 3 and 4. Finally, Chapter 5 revisits the problem of trapping in unbounded domains, where the existence of the attractor is not guaranteed. Chapter 6 is the conclusion.

Chapter 2

Single-phase flow in a thin plane channel

The first thing we need to study particle transport is a model of the carrier flow between fracture walls. In this chapter we revisit the classical problem of inertial lubrication theory: fluid flow through a thin 2D channel with smoothly varying walls. Following the classical procedure, we obtain the second-order asymptotic solution, keeping the wall shapes arbitrary and independent. This allows us to consider a wider range of geometries than in previous studies and to question the influence of channel geometry on macroscopic flow properties. Using the asymptotic solution we calculate non-linear corrections to Darcy's law, which are cubic in flow rate and depend (up to second order of accuracy) on three integral shape factors concentrating all information on channel geometry. We also find the range of flow rates in which the local cubic law (LCL) model is valid on local and on macroscopic levels and show that these ranges are different.

2.1 Introduction

To understand how exactly corrugation of fracture walls can produce non-linear terms in the macroscopic equation (1.3), investigation of the flow structure on microlevel is unavoidable. Navier-Stokes equations describing the flow between fracture walls have no

analytical solution, except for the trivial case when walls are parallel plates. They can be investigated numerically (see, for example, the thesis of Brush [9] and the references within) or using asymptotic methods. If the typical gap of the channel H_0 is small compared to typical corrugation length L_0 (lubrication theory approximation) the solution of Navier-Stokes equations for the flow can be searched in form of an asymptotic expansion by powers of the small parameter $\varepsilon = H_0/L_0$ and channel Reynolds number Re_H. This approach has been developed by many authors (see [73] for a broader review), often in simplified 2D geometries that allow fully analytical solution[1].

For creeping flows ($\mathrm{Re}_H = 0$) the first-order solution is given by classical lubrication theory. Higher order approximations (up to 4th order in ε) can be found in Kitanidis and Dykaar [37]. This asymptotic solution provides viscous corrections to the permeability coefficient K in Darcy's law and reveals a non-trivial structure of the flow on local-level (non-inertial flow recirculation within corrugations). However, they give no information about non-linear corrections to the Darcy law at higher flow rates.

Effects of fluid inertia in thin 2D channels have been considered in classical works of Van Dyke [67], where he found the first inertial corrections to the solution given by lubrication theory. Second order corrections have been calculated by different authors for specific geometries. Hasegawa and Izuchi [31] calculated them for a channel with one corrugated and one flat wall. Borisov [7] found the solution for a channel with parallel walls. The mirror-symmetric case has been solved in the thesis by Crosnier [16] both for plane and radial fractures (the results for the radial fracture can be found in Buès *et al.* [10] for a radial). In this chapter we generalize these results to arbitrary wall shapes (with slopes limited by $\varepsilon \ll 1$) and express the inertial corrections to the flow rate curve $\Delta P(Q)$ in terms of three integral factors, containing all information on channel geometry.

Outline of the chapter. In this chapter we revisit the classical problem of a viscous flow through a thin 2D channel with slowly varying periodic walls, keeping their shapes arbitrary. In Section 2.2 we define the channel geometry and introduce non-dimensional variables and the small parameter of the problem ε. In Section 2.3 Navier-Stokes equations are written down in rescaled channel variables and are reduced to a single partial

---

[1]In the 3D case lubrication approximation can be applied as well, but the equations arising for the terms of the asymptotic expansion have to be solved numerically (see Jacono et al. [36]).

differential equation for the stream function $\Psi(x, z)$ and the second-order asymptotic solution is found for arbitrary wall shapes. We use it to derive a formula for the non-dimensional pressure drop as a function of Re_H, ε and some averaged geometric factors of the channel. Finally, in Section 2.4 these results are applied to a test family of wavy-walled channels (a benchmark problem that will be used for all simulations throughout the thesis). We compare the asymptotic solution with numerical computations performed with the Fluent software and verify that $\Delta P(Q)$ curve and velocity fields are in good agreement for small to moderate Reynold numbers.

2.2 Channel geometry, small parameter and the test problem

2.2.1 Small parameters in channel geometry

We consider a two-dimensional channel of the following form (see Fig. 2.1):

$$D = \{(X, Z) : X \in (0; L_\infty), Z \in (\Phi_1(X); \Phi_2(X))\},$$

where $\Phi_1(X), \Phi_2(X)$ are prescribed wall shapes with bounded local slopes: $|\partial \Phi_k / \partial X| \leq s$. We neglect microscopic roughness and take into account only smooth variations of channel walls, assuming that the wall slopes are always small: $s \ll 1$.

The major part of this thesis (Chapters 3 and 4) is devoted to periodic channels. For a periodic channel the natural length scale in X-direction is the channel period $L_0{}^2$: $\Phi_k(X + L_0) = \Phi_k(X)$. To define the other length scales in the channel we introduce the mean aperture of the channel:

$$H_0 = \frac{1}{L_\infty} \int_0^{L_\infty} (\Phi_2(X) - \Phi_1(X)) dX,$$

---

[2]For non-periodic channels a single corrugation can be defined as a piece of the wall between two local maximums of the wall shapes. The typical corrugation length can be defined as the average distance between two maximums, and the typical corrugation amplitude as the average of single corrugation amplitudes.
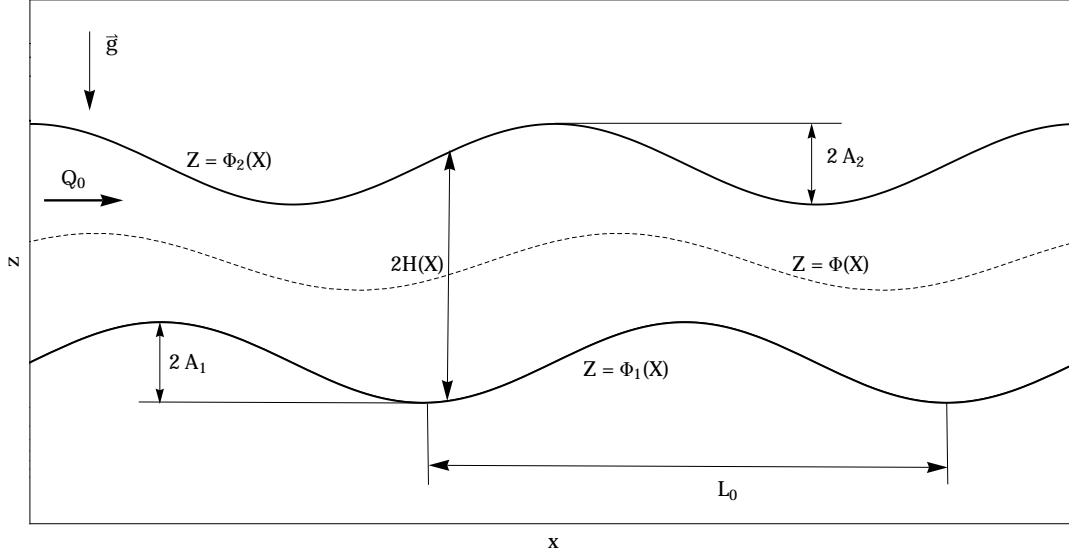
Figure 2.1: *Sketch of a periodic channel with corrugation period L_0 and mean aperture H_0. $Z = \Phi(X)$ is the middle line of the channel and $H(X)$ is the local half-aperture.*

the corrugation amplitudes of lower ($k = 1$) and upper ($k = 2$) walls (see Fig. 2.1):

$$A_k = \frac{1}{2} \left(\Phi_k^{max} - \Phi_k^{min} \right),$$

and the *average corrugation amplitude*:

$$A_0 = \frac{1}{2} \left(A_1 + A_2 \right).$$

Therefore, we can define the following non-dimensional parameters: the *aspect ratio of the channel*:

$$\varepsilon = \frac{H_0}{L_0},$$

and the non-dimensional average corrugation:

$$\delta_0 = A_0 / H_0.$$

Smoothness of corrugation implies that $A_1/L_0, A_2/L_0 \ll 1$ (and therefore $\varepsilon\delta_0 \ll 1$), but sets no restriction on the aspect ratio ε. We can, therefore, define two types of channel geometries, depending on the non-dimensional parameters. In channels of Type I (see
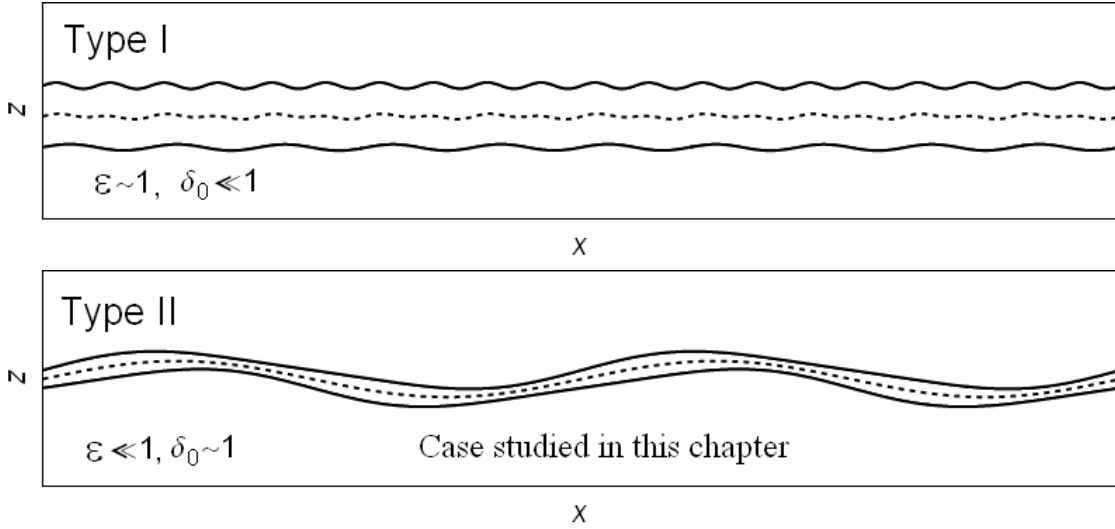
Figure 2.2: *Two types of channels with small wall slopes. Dashed line is the middle line of the channel.*

Fig. 2.2, top) corrugations are small compared to the gap of the channel, but the channel itself is not thin ($\delta_0 \ll 1$ and $\varepsilon \sim 1$). In the channels of Type II (see Fig. 2.2, bottom) the typical corrugation length is much larger than the mean gap of the channel (the channel is thin and the corrugations are "slow"), but the amplitudes of these slow corrugations can be comparable to the channel gap ($\delta_0 \sim 1$ and $\varepsilon \ll 1$).

Asymptotic solution of flow equations in channels of Type I has been considered by Tsangaris and Leiter [65] for a mirror-symmetric channel (with $\Phi_1(X) = -\Phi_2(X)$) and later by Zhou et al. [72] for a channel with one corrugated and one flat wall (with $\Phi_1(X) \equiv 0$) using asymptotic expansion in δ_0 and expansion of the wall shape into Fourier series. We do not consider such channels here.

We focus our attention on channels of second type. For these channels a fully analytical asymptotic solutions of 2nd order have been obtained by different authors in specific channel geometries: by Hasegawa and Izuchi [31] in a channel with one flat wall ($\Phi_1(X) \equiv 0$), by Crosnier [16] in a mirror-symmetric channel ($\Phi_1(X) = -\Phi_2(X)$) and by Borisov [7] in a channel with parallel walls ($\Phi_2(X) = \Phi_1(X) + H_0$) . Following these authors we perform asymptotic expansions of flow equations taking ε as small parameter - but keep the wall shapes $\Phi_1(X)$ and $\Phi_2(X)$ arbitrary and independent.

2.2.2   Quantifying channel geometry: the shape factors

Choosing corrugation length L_0 and mean aperture H_0 as the principal length scales, let us define non-dimensional variables in the following way:

$$x = X/L_0, \; z = Z/H_0, \; \phi_{1,2}(x) = \Phi_{1,2}(L_0 x)/H_0,$$
$$\delta_{1,2} = A_{1,2}/H_0, \; l_\infty = L_\infty/L_0 \tag{2.1}$$

In these variables the "small slopes" assumption implies that $\phi'_{1,2}(x) = O(1)$.

For the following it is convenient to redefine the geometry in terms of channel middle line:

$$\phi(x) = \frac{1}{2}\left(\phi_1(x) + \phi_2(x)\right)$$

and half-aperture of the channel[3]:

$$h(x) = \frac{1}{2}\left(\phi_2(x) - \phi_1(x)\right).$$

Looking ahead, let us define here the following integral shape factors, which will be used throughout the thesis:

$$\langle h^{-3} \rangle = \frac{1}{l_\infty} \int_0^{l_\infty} \frac{dx}{h^3(x)}, \qquad J_h = \frac{1}{l_\infty} \int_0^{l_\infty} \frac{(h'(x))^2 dx}{h^3(x)},$$
$$J_\phi = \frac{1}{l_\infty} \int_0^{l_\infty} \frac{(\phi'(x))^2 dx}{h^3(x)}, \quad J_{\phi h} = \frac{1}{l_\infty} \int_0^{l_\infty} \frac{\phi'(x) h'(x) dx}{h^3(x)}. \tag{2.2}$$

The first of them, $\langle h^{-3} \rangle$, is well-known as *apparent* or *hydrodynamic aperture* of the channel [73]. To clarify the physical meaning of the others they should be rewritten in terms of "corrugation norms" of the walls.

Indeed, let us introduce an aperture-weighted scalar product of two functions $a(x)$ and $b(x)$ in the following way:

$$\langle a, b \rangle_h = \frac{1}{l_\infty} \int_0^{l_\infty} \frac{a(x) \cdot b(x) dx}{h^3(x)},$$

---

[3]Note that aperture defined this way does not coincide with the distance between the walls at point x.

and let us denote the norm induced by this scalar product by $\|a\|_h = \sqrt{\langle a, a \rangle_h}$.

Then, the J-integrals can be rewritten in the following form:

$$J_h = \|h'\|_h^2, \quad J_\phi = \|\phi'\|_h^2, \quad J_{\phi h} = \|\phi_2'\|_h^2 - \|\phi_1'\|_h^2. \tag{2.3}$$

The physical meaning of these integrals is now clear: $J_h > 0$ is a measure of aperture variations, $J_\phi > 0$ measures the corrugation of the middle-line profile of the fracture and $J_{\phi h}$ measures the difference between wall corrugations. $J_{\phi h}$ is positive when the upper wall is more corrugated than the lower one, and negative in the opposite case.

The shape factors (2.3) contain all necessary information on fracture geometry: as we shall see later, in the asymptotic regime all transport properties (flow rate curves for the single-phase flow, focusing rates and propagation lengths for particles) will depend (to the leading order) on these four parameters.

2.2.3 Test problem: channel with sinusoidal walls

Most of the asymptotic results will be formulated for arbitrary shape functions $\phi(x)$, $h(x)$. To validate theoretical results and provide some illustrative examples, we define the following test problem.

Consider a channel with sinusoidal walls of the same wavelength L_0 and different amplitudes A_1 and A_2, shifted in horizontal direction by ΔX and in vertical direction by H_0:

$$
\begin{aligned}
\Phi_1(X) &= -H_0/2 + A_1 \sin\left(2\pi X/L_0 - \Delta X/2\right), \\
\Phi_2(X) &= H_0/2 + A_2 \sin\left(2\pi X/L_0 + \Delta X/2\right).
\end{aligned}
\tag{2.4}
$$

In non-dimensional variables (defined by Eq. (2.1) with mean gap H_0 and corrugation period L_0) the middle line $\phi(x)$ and the half-aperture $h(x)$ of the channel take the following form:

$$
\begin{aligned}
\phi(x) &= \delta_0 \left(\sin(2\pi x)\cos(\alpha/2) + \gamma\cos(2\pi x)\sin(\alpha/2)\right), \\
h(x) &= 1/2 + \delta_0 \left(\cos(2\pi x)\sin(\alpha/2) + \gamma\sin(2\pi x)\cos(\alpha/2)\right),
\end{aligned}
\tag{2.5}
$$

so that each channel of this family is defined by three non-dimensional parameters: the
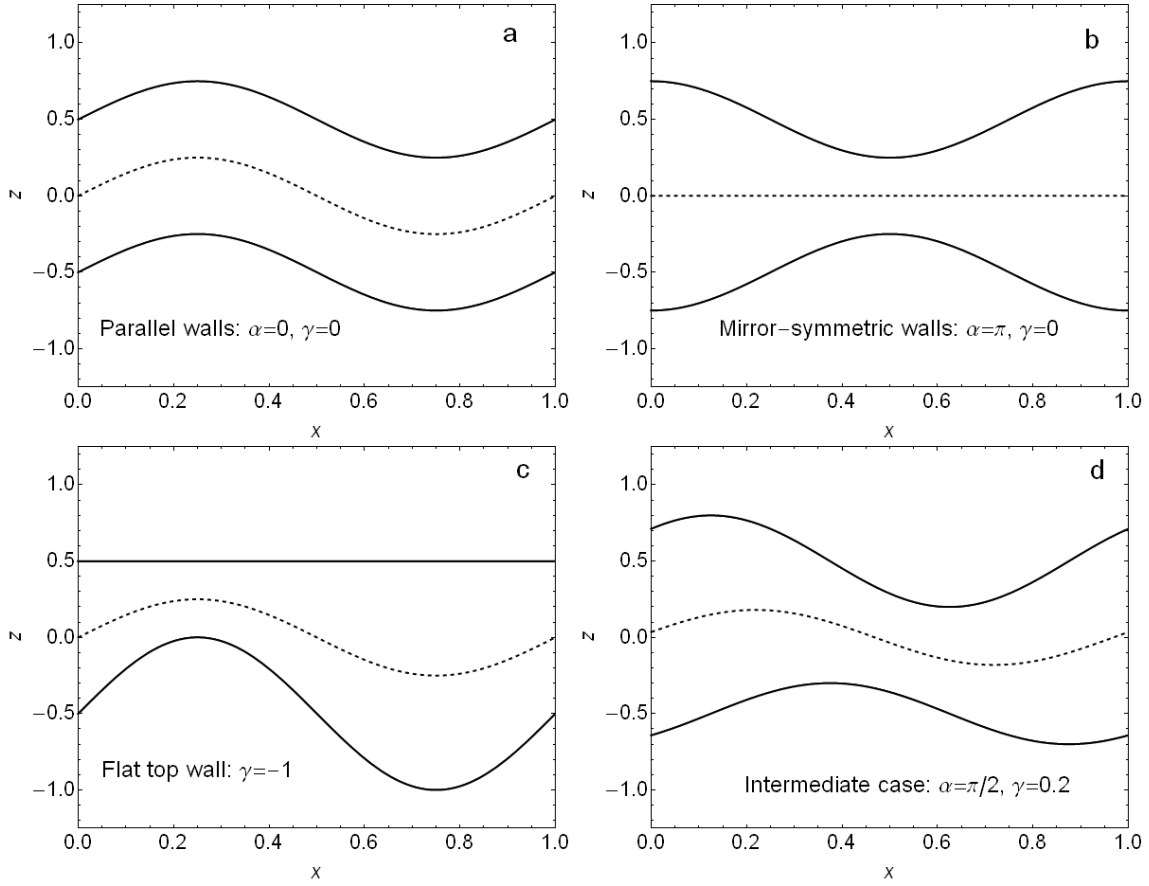
Figure 2.3: *Examples of test geometries defined by Eq. (2.5) with fixed average amplitude $\delta_0 = 0.25$ and different phase shifts α and wall corrugation ratios γ. Plots are in rescaled variables $x = X/L_0$, $z = Z/H_0$.*

average corrugation amplitude

$$\delta_0 = \frac{A_1 + A_2}{2H_0}, \tag{2.6}$$

the phase shift

$$\alpha = \frac{2\pi\Delta X}{L_0}, \tag{2.7}$$

and the wall corrugations asymmetry

$$\gamma = \frac{A_2 - A_1}{A_2 + A_1}. \tag{2.8}$$

Examples of channels for different values of α and γ are provided in Fig. 2.3. By varying α, γ and δ_0 we can obtain channels with all possible values of J-integrals (integral factors

defined by Eq. (2.3) and describing channel geometry). Two families will be of special importance in this thesis.

Channels with identical shifted walls ($A_1 = A_2$, $\Delta X \neq 0$).

In this case $\gamma = 0$ and α varies from $\alpha = 0$ (parallel walls, see Fig. 2.3, a) to $\alpha = \pi$ (mirror-symmetric walls, see Fig. 2.3, b).

For channels of this family $J_{h\phi} = \|\phi_2'\|^2 - \|\phi_1'\|^2 = 0$, because the wall shapes are identical. The other shape factor can be calculated analytically:

$$\langle h^{-3} \rangle = \frac{8(1 + \delta_\alpha^2)}{(1 - 4\delta_\alpha^2)^{5/2}}, \quad J_h = \frac{16\pi^2 \delta_\alpha^2}{(1 - 4\delta_\alpha^2)^{3/2}}, \quad J_\phi = 16\pi^2 \frac{(\delta_0^2 - \delta_\alpha^2)(1 + 8\delta_\alpha^2)}{(1 - 4\delta_\alpha^2)^{5/2}},$$
$$J_{\phi h} = 0,$$

(2.9)

where $\delta_\alpha = \delta_0 \sin(\alpha/2)$ can be called the *apparent amplitude of corrugation* by analogy with apparent aperture defined in [73]. Indeed, one can note that δ_α is equal to $(h_{max} - h_{min})/2$ and reflects the actual aperture variation better than δ_0, which is based on individual corrugation amplitudes of the walls.

Channels with different corrugation amplitudes ($\Delta X = L_0/2$, $A_1 \neq A_2$).

In this case $\alpha = \pi$ and γ varies from $\gamma = 0$ (mirro-symmetric channel, see Fig. 2.3, b) through $\gamma = \pm 1$ (a channel with one of the walls flat, see Fig. 2.3, c) to $\gamma = \pm\infty$ (channel with parallel walls, see Fig. 2.3, a).

The shape factors are:

$$\langle h^{-3} \rangle = \frac{8(1 + \delta_0^2)}{(1 - 4\delta_0^2)^{5/2}}, \quad J_h = \frac{16\pi^2 \delta_0^2}{(1 - 4\delta_0^2)^{3/2}},$$
$$J_\phi = \gamma^2 J_h, \quad J_{\phi h} = \gamma J_h.$$

(2.10)

Note that J_h does not depend on γ, so we can vary J_ϕ and $J_{\phi h}$ keeping J_h constant.

These two families of channel geometries with different parameters will be used in all numerical simulation throughout the thesis.

2.3   Asymptotic analysis of flow in a thin channel

2.3.1   Navier-Stokes equations in streamfunction formulation

In the general case fluid flows in the fracture are described by Navier-Stokes equations, accompanied by the incompressibility condition:

$$\rho_f \frac{D\vec{U}}{Dt} = -\vec{\nabla}P + \mu\Delta\vec{U} + \rho_f\vec{g},$$
$$\text{div}\vec{U} = 0,$$

$$(2.11)$$

where $\vec{U}$ is fluid velocity field, P is pressure, $\vec{g} = g\vec{e}_g$ is the gravity acceleration vector and ρ_f, μ are fluid density and dynamic viscosity respectively. $\dfrac{D}{Dt}$ denotes the material time derivative: $\dfrac{D\vec{U}}{Dt} = (\overline{\overline{\vec{\nabla}}}\vec{U}) \cdot \vec{U}$ for the steady flow.

We set the no-slip conditions on the fracture walls and consider the volumetric flow rate per unit length[4] Q:

$$\vec{U}(X, \Phi_1(X)) = 0, \qquad \vec{U}(X, \Phi_2(X)) = 0$$
$$\int_{\Phi_1(X)}^{\Phi_2(X)} U_x(X, Z)dZ = Q.$$

For a steady incompressible flow in two dimensions, the velocity field can be represented using the streamfunction $\Psi(X, Z)$:

$$U_x = \frac{\partial\Psi}{\partial Z}, \; U_z = -\frac{\partial\Psi}{\partial X}.$$

The Navier-Stokes equations can then be rewritten in the following form:

$$\frac{\partial\Psi}{\partial Z}\frac{\partial\Delta\Psi}{\partial X} - \frac{\partial\Psi}{\partial X}\frac{\partial\Delta\Psi}{\partial Z} = \nu\Delta\Delta\Psi,$$

$$(2.12)$$

---

[4]Keeping the same symbol Q, that was used at the beginning of this chapter for the volumetric flow rate.

with the following boundary conditions:

$$\frac{\partial \Psi}{\partial n_1} = 0, \quad \Psi = -Q/2 \text{ at } Z = \Phi_1(X) \forall x \in [0; L_\infty];$$
$$\frac{\partial \Psi}{\partial n_2} = 0, \quad \Psi = Q/2 \text{ at } Z = \Phi_2(X), \forall x \in [0; L_\infty] \tag{2.13}$$

where $\vec{n}_m = \dfrac{(-\Phi'_m(X), 1)}{\sqrt{1 + \Phi'_m(X)^2}}$, $m = 1, 2$ is the unit vector perpendicular to the wall.

We use rescaled non-dimensional variables defined by Eq. (2.1): $x = X/L_0$, $z = Z/H_0$. As x-velocity scale we take the mean flow velocity $U_0 = Q/H_0$ and use the rescaled one for the z-velocity:

$$\psi = \Psi/Q, \ u_x = U_x/U_0, \ u_z = \varepsilon U_z/U_0. \tag{2.14}$$

In these variables $u_x = \psi_{,z}$, $u_z = -\psi_{,x}$ (symbols following the comma in the index indicate partial derivatives) and equation (2.12) for the streamfunction takes the following form (see, for example, [6]):

$$\text{Re}_H \left(\varepsilon^3 \left(\psi_{,z}\psi_{,xxx} - \psi_{,x}\psi_{,xxz} \right) + \varepsilon \left(\psi_{,z}\psi_{,zzx} - \psi_{,x}\psi_{,zzz} \right) \right) = \varepsilon^4 \psi_{,xxxx} + 2\varepsilon^2 \psi_{,xxzz} + \psi_{,zzzz},$$
$$\tag{2.15}$$

where $\text{Re}_H = U_0 H_0/\nu$ is the flow Reynolds number. The total flow rate in these units is equal to unity: $\int_{\phi_1(x)}^{\phi_2(x)} u_x dz = 1$ and boundary conditions become

$$\frac{\partial \psi}{\partial z} - \varepsilon^2 \phi'_1 \frac{\partial \psi}{\partial x} = 0, \quad \psi = -1/2 \text{ at } z = \phi_1(x);$$
$$\frac{\partial \psi}{\partial z} - \varepsilon^2 \phi'_2 \frac{\partial \psi}{\partial x} = 0, \quad \psi = 1/2 \text{ at } z = \phi_2(x), \tag{2.16}$$

as wall normal vectors in these rescaled variables have the following form: $\vec{n}_m = \dfrac{(-\varepsilon\phi'_m(x), 1)}{\sqrt{1 + (\varepsilon\phi'_m)^2}}$.

For the moment ε can have any values (equations (2.15) and (2.16) are exact). In the following section we consider the limit when both $\varepsilon \ll 1$ and $\varepsilon \text{Re}_H \ll 1$ and construct the asymptotic solution of equation (2.15), keeping the wall shapes $\phi_1(x)$ and $\phi_2(x)$ arbitrary and independent.

2.3.2   Asymptotic solution of 2nd order

This rather technical section is devoted to the derivation of an analytical expression for the 2nd order asymptotic solution to Navier-Stokes equations in the limit $\varepsilon \ll 1$, $\varepsilon\mathrm{Re}_H \ll 1$.

Cross-channel coordinate. To simplify the problem it is useful to introduce a new variable – the cross-channel coordinate η:

$$\eta(x, z) = \frac{z - \phi(x)}{h(x)}, \qquad\qquad (2.17)$$

which maps the interior of the channel into a rectangle: $(x, \eta) \in [0, l_\infty] \times [-1; 1]$. To avoid confusion, the functions of these new variables (x, η) are marked by a tilde:

$$\tilde{\psi}(x, \eta) = \psi(x, z(x, \eta)),$$
$$\tilde{u}_z(x, \eta) = \frac{\partial\psi}{\partial z} = \frac{1}{h(x)}\frac{\partial\tilde{f}}{\partial\eta}, \qquad \tilde{u}_z(x, \eta) = \frac{\partial f}{\partial x} = \frac{\partial\tilde{f}}{\partial x} + \eta_{,x}\frac{\partial\tilde{\psi}}{\partial\eta},$$

where $\eta_{,x} = \dfrac{\partial\eta}{\partial x} = -\dfrac{h'(x)\eta - \phi'(x)}{h(x)}$. Derivatives of higher orders can be found by induction.

We search for the streamfunction in the form of an asymptotic expansion:

$$\tilde{\psi}(x, \eta) = \tilde{\psi}^0(x, \eta) + \varepsilon\tilde{\psi}^1(x, \eta) + \varepsilon^2\tilde{\psi}^2(x, \eta) + \dots \qquad\qquad (2.18)$$

The boundary conditions (2.16) in new variables read:

Lower wall $(\eta = -1)$:
$$\frac{1}{h(x)}\frac{\partial\tilde{\psi}}{\partial\eta} - \varepsilon^2\phi_1'(x)\left(\frac{\partial\tilde{\psi}}{\partial x} + \eta_{,x}\frac{\partial\tilde{\psi}}{\partial\eta}\right) = 0, \ \ \tilde{\psi}(x, \eta) = -1/2,$$

Upper wall$(\eta = 1)$:
$$\frac{1}{h(x)}\frac{\partial\tilde{\psi}}{\partial\eta} - \varepsilon^2\phi_2'(x)\left(\frac{\partial\tilde{\psi}}{\partial x} + \eta_{,x}\frac{\partial\tilde{\psi}}{\partial\eta}\right) = 0, \ \ \tilde{\psi}(x, \eta) = 1/2.$$

Substituting here the expansion (2.18) and taking into account the fact that $\dfrac{\partial\tilde{\psi}}{\partial x} = 0$ at

$\eta = \pm 1$, we get for successive $k = 0, 1, 2, ...$:

Lower wall $(\eta = -1)$:

$$\frac{\partial \tilde{\psi}^0}{\partial \eta} = 0, \quad \frac{\partial \tilde{\psi}^1}{\partial \eta} = 0, \quad \frac{\partial \tilde{\psi}^k}{\partial \eta} + (\phi_1')^2 \frac{\partial \tilde{\psi}^{k-2}}{\partial \eta} = 0, \ k \geq 2,$$

Upper wall $(\eta = 1)$:

$$\frac{\partial \tilde{\psi}^0}{\partial \eta} = 0, \quad \frac{\partial \tilde{\psi}^1}{\partial \eta} = 0, \quad \frac{\partial \tilde{\psi}^k}{\partial \eta} + (\phi_2')^2 \frac{\partial \tilde{\psi}^{k-2}}{\partial \eta} = 0, \ k \geq 2.$$

Applying the induction, we find that all conditions for $k \geq 1$ are trivial[5]:

$$\tilde{\psi}^0(x, \pm 1) = \pm 1/2, \ \frac{\partial \tilde{\psi}^0}{\partial \eta}(x, \pm 1) = 0,$$

$$\tilde{\psi}^k(x, \pm 1) = 0, \ \frac{\partial \tilde{\psi}^k}{\partial \eta}(x, \pm 1) = 0, \ k \geq 1. \tag{2.19}$$

Substituting the expansion (2.18) into the equation (2.15) and gathering the terms with equal powers of ε we come up with a set of equations for $\tilde{\psi}^k(x, \eta)$, which are listed below.

0th approximation (Local Cubic Law):

The leading-order term of Eq. (2.15) yields the following:

$$\begin{cases} \dfrac{1}{h^4(x)} \dfrac{\partial \tilde{\psi}^0}{\partial \eta^4} = 0; \\ \tilde{\psi}^0(x, -1) = -1/2, \ \dfrac{\partial \tilde{\psi}^0}{\partial \eta}(x, -1) = 0; \\ \tilde{\psi}^0(x, 1) = 1/2, \ \dfrac{\partial \tilde{\psi}^0}{\partial \eta}(x, 1) = 0. \end{cases}$$

Solution to this is the famous "local cubic law" (LCL) [73]:

$$\tilde{\psi}^0(x, \eta) = \frac{1}{4}\eta \left(3 - \eta^2\right). \tag{2.20}$$

Note that it does not depend explicitly on x, so its streamlines are defined by $\eta = const$.

---

[5]These trivial conditions could be derived directly by setting to zero the derivatives of Ψ in two independent directions (not necessarily orthogonal). This has not been done deliberately, to keep the possibility of including wall permeability or non-zero slip in the future (not in this thesis).

The velocity field in (x, η) reads:

$$\tilde{u}_x^0(x, \eta) = \frac{3}{4h(x)}\left(1 - \eta^2\right),$$
$$\tilde{u}_z^0(x, \eta) = \frac{3(\phi'(x) + \eta h'(x))}{4h(x)}\left(1 - \eta^2\right).$$
(2.21)

1st approximation:

Calculating $\psi^0(x, z) = \tilde{\psi}^0(x, \eta(x, z))$, inserting it into Eq. (2.15) and considering the coefficients of ε^1, we get:

$$\psi^1_{,yyyy} = \mathrm{Re}_H\left(\psi^0_{,z}\psi^0_{,zzx} - \psi^0_{,x}\psi^0_{,zzz}\right).$$

In (x, η) variables the boundary value problem takes the following form:

$$\begin{cases} \dfrac{1}{h^4(x)}\tilde{\psi}^1_{,\eta\eta\eta\eta} = \dfrac{9h'}{4h^4}\eta(1 - \eta^2)\mathrm{Re}_H, \\ \tilde{\psi}^1(x, -1) = 0,\ \tilde{\psi}^1_{,\eta}(x, -1) = 0 \\ \tilde{\psi}^1(x, 1) = 0,\ \tilde{\psi}^1_{,\eta}(x, 1) = 0 \end{cases}$$

and the solution is

$$\tilde{\psi}^1(x, \eta) = \mathrm{Re}_H\frac{3}{1120}h'(x)\eta(\eta^2 - 1)^2(5 - \eta^2).$$
(2.22)

This term describes the first inertial correction to the viscous flow. It depends only on the variation of the local gap $h(x)$ and not on the form of the center line $\phi(x)$.

2nd approximation:

Identifying terms with ε^2 we get the following equation:

$$\psi^2_{,yyyy} = 2\psi^0_{,xxzz} - \mathrm{Re}_H\left(\psi^0_{,z}\psi^1_{,zzx} - \psi^0_{,x}\psi^1_{,zzz} + \psi^1_{,z}\psi^0_{,zzx} - \psi^1_{,x}\psi^0_{,zzz}\right)$$

with boundary conditions (2.19). The solution can be split into parts induced by viscous and inertial terms: $\tilde{\psi}^2(x, \eta) = \tilde{\psi}^{2i}(x, \eta) + \tilde{\psi}^{2v}(x, \eta)$. The viscous part turns out to be

$$\tilde{\psi}^{2v}(x, \eta) = \frac{3}{120}\left(3a_1(x)\eta + 5a_2(x)\right)\left(\eta^2 - 1\right)^2,$$
(2.23)

where $a_1(x) = hh'' - 4(h')^2$ and $a_2(x) = h\phi'' - 6h'\phi'$ depend on both shape functions $h(x)$ and $\phi(x)$. Note, that for the mirror-symmetric channel ($\phi(x) \equiv 0$) this term gives exactly the 2nd order viscous correction from Kitanidis and Dykaar (see Eq. (37) in [37]).

The contribution of inertial forces is:

$$\tilde{\psi}^{2i}(x,\eta) = \frac{9\mathrm{Re}_H^2}{4480} \left(h'' h c_1(\eta) + (h')^2 c_2(\eta) \right) \eta(\eta^2 - 1)^2, \qquad (2.24)$$

where
$$c_1(\eta) = \frac{(\eta^2 - 1)(35\eta^4 - 280\eta^2 + 573) - 640}{6930},$$
$$c_2(\eta) = -\frac{(\eta^2 - 1)(98\eta^4 - 861\eta^2 + 1611) - 1264}{6930}.$$

The asymptotic solution obtained here can be applied to any channel geometry (periodicity not required) with small aspect ratio ε and smooth walls ($\phi_{1,2}(x)$ with bounded second derivatives). It embraces in a compact form some special cases, considered previously in the literature. Indeed, for a channel with flat bottom wall ($\phi_1 \equiv 0$) it coincides exactly (after a change of variables) with the solution obtained by Hasegawa and Izuchi (see Eq. (21)-(23) in [31]). For a channel with mirror-symmetric walls ($\phi(x) \equiv 0$) the velocity field derived from this asymptotic streamfunction coincides[6] with one obtained by Crosnier [16] (who solved the Navier-Stokes equations in natural variables $\vec{u}$ and p).

Special case: channel with parallel walls.

For channels with parallel walls ($h(x) \equiv 1/2$) both first order and second order inertial corrections (Eq. (2.22) and Eq. (2.24) respectively) are equal to zero. To study inertial effects in such channels it is necessary to consider higher-order terms of asymptotic expansion (2.18). The procedure applied in this section can be continued to higher orders, but calculations become too heavy to track them manually. The following section describes a recursive algorithm, that was implemented in Mathematica software to obtain the higher-order terms of expansion.

---

[6]After correcting an obvious misprint in [16].

2.3.3   Higher-order asymptotic terms

Generally, the boundary-value problem for k-th approximation has the following form:

$$
\begin{cases}
\dfrac{1}{h^4(x)}\dfrac{\partial \tilde{\psi}^k}{\partial \eta^4} = F_k(\psi^0, \psi^1, ...\psi^{k-1}), \\[2mm]
\tilde{\psi}^k(x, -1) = 0,\ \tilde{\psi}^k_\eta(x, -1) = 0, \\[2mm]
\tilde{\psi}^k(x, 1) = 0,\ \tilde{\psi}^k_\eta(x, 1) = 0.
\end{cases}
$$

To obtain the right-hand side F_k of this equation we should input the first k terms of the expansion Eq. (2.18) into Eq. (2.15) and collect the coefficients of ε^k. This can be easily done with the Mathematica or any other computer algebra software. The result is always polynomial in η:

$$
\tilde{F}_k(x, \eta) = \sum_{i=1}^{N(k)} a_k^i(x)\eta^i,
$$

where $a_k^i(x)$ are the coefficients and $N(k)$ is the order of the resulting polynomial. Once these coefficients are found, the solution can be calculated as:

$$
\tilde{\psi}_k(x, \eta) = \sum_{i=1}^{N(k)} h^4(x)a_k^i(x)p_i(\eta),
$$

where $p_i(\eta)$ is the solution of the following boundary problem:

$$
\begin{cases}
\dfrac{\partial^4 p_i}{\partial \eta^4} = \eta^i, \\[2mm]
p_i(\pm 1) = 0,\, p_{i\eta}'(\pm 1) = 0.
\end{cases}
$$

The correction to the velocity field is calculated in the following form:

$$
\tilde{u}_x(x, \eta) = \sum_{i=1}^{N(k)} h^3(x)a_k^i(x)p_i'(\eta),
$$
$$
\tilde{u}_z(x, \eta) = \sum_{i=1}^{N(k)} (h^3(x)a_k^i(x)(\phi' + \eta h')p_i'(\eta) + (h^4(x)a_k^i(x))'p_i'(\eta).
$$

Using this algorithm we have found asymptotic solution up to 6th order. The resulting formulas are too heavy to be written here, but they will be used in Section 2.4 to estimate

numerically the radius of convergence of the asymptotic series.

Special case: channel with parallel walls. Using this procedure, we can resolve the problem for channels with parallel walls. As we have seen in the previous section, inertial corrections for such channels are zero up to second order in ε. Applying this algorithm with $h(x) \equiv 1/2, \eta = 2(z - \phi(x))$, we find the leading order corrections for a parallel channel:

$$
\begin{aligned}
\tilde{\psi}_{par}(x, \eta) &= \frac{1}{4}\eta \left(3 - \eta^2\right) - \frac{\varepsilon^2}{8}\left(1 - \eta^2\right)^2 \phi''(x) + O(\varepsilon^4) + \\
&+ \frac{3\varepsilon^3 \mathrm{Re}_H}{1120}\left(b_1(\eta)\phi'\phi'' + b_2(\eta)\phi'''\right) + O(\varepsilon^4 \mathrm{Re}_H^2),
\end{aligned}
\tag{2.25}
$$

where $b_1(\eta) = \eta(\eta^2 - 1)^2(\eta^2 - 5)$ and $b_2(\eta) = 2/3(\eta^2 - 1)^2(\eta^4 + 2\eta^2 - 67)$. After appropriate rescaling, this solution coincides exactly with one obtained by Borisov (see Eq. (14) of [7]), who used the same method as here setting $h(x) = const$ from the very beginning.

Looking at Eq. (2.22-2.24) and Eq. (2.25) we could say that there are two different effects of fluid inertia: the first one is acceleration and deceleration of the fluid due to aperture variation (described by $h(x)$ and its derivations), and the second one (much weaker!) is some "centrifugation effect" due to the curved form of the channel (described by $\phi(x)$ and its derivations). Note that in a two-scaled channel with $h' = O(\varepsilon^2 \phi')$ the two effects can be of the same order of magnitude.

2.3.4 Flow rate curves: inertial corrections to Darcy's law

To find the inertial corrections to Darcy's law we should calculate the pressure drop for the asymptotic solution obtained above. To do this we define the mean pressure difference between the inlet $X_1 = 0$ and the outlet $X_2 = L_\infty$ of the channel: $\Delta P = \overline{P}(X_2) - \overline{P}(X_1)$, where:

$$
\overline{P}(X) = \frac{1}{H(X)} \int_{\Phi_1(X)}^{\Phi_2(X)} P(X, Z)dZ.
$$

Choosing the viscous lubrication pressure $P_0 = \mu U_0/\varepsilon H_0$ as pressure scale, and passing to channel coordinates (x, η), we get:

$$\bar{p}(x) = \frac{1}{2h(x)} \int\limits_{\phi_1(x)}^{\phi_2(x)} p(x, z)dz = \frac{1}{2} \int\limits_{-1}^{1} \tilde{p}(x, \eta)dz.$$

Now the non-dimensional pressure drop $\Delta p = \Delta P/P_0$ can be written as:

$$\Delta p = \int\limits_{0}^{l_\infty} \frac{d}{dx}\bar{p}(x)dx = \int\limits_{0}^{l_\infty} \left(\frac{1}{2} \int\limits_{-1}^{1} \frac{\partial}{\partial x}\tilde{p}(x, \eta(x, z))d\eta \right) dx,$$

where $\dfrac{\partial \tilde{p}(x, \eta(x, z))}{\partial x} = \dfrac{\partial p(x, z)}{\partial x}$ is the x-component of the pressure gradient.

The pressure gradient itself can be found from Navier-Stokes equations (2.11):

$$\frac{\partial p}{\partial x} = \left(\varepsilon^2 \frac{\partial^2 u_x}{\partial x^2} + \frac{\partial^2 u_x}{\partial z^2} \right) - \text{Re}_H\varepsilon \left(u_x \frac{\partial u_x}{\partial x} + u_z \frac{\partial u_x}{\partial u_z} \right).$$

Substituting the second-order solution, integrating over $\eta \in [-1; 1]$ and regrouping the terms by powers of Re_H, we get (assuming that the walls are smooth):

$$\begin{aligned}
\overline{\frac{\partial p}{\partial x}} &= -\frac{3}{2h^3} \left(1 + \left(\frac{(h')^2}{5} + (\phi')^2 \right) \varepsilon^2 \right) - \frac{3\varepsilon^2}{5} \left(\frac{h'}{h^2} \right)' + \left(\frac{1}{h^2} \right)' \frac{27\text{Re}_H\varepsilon}{140} - \\
&\quad - \frac{3}{2h^3} \left(\frac{26h'^2}{11} \right) \left(\frac{\text{Re}_H\varepsilon}{35} \right)^2 - \frac{234}{44} \left(\frac{h'}{h^2} \right)' \left(\frac{\text{Re}_H\varepsilon}{35} \right)^2.
\end{aligned}$$

Integrating this cross-channel average for $x \in [0; l_\infty]$ we get[7]:

$$\frac{\Delta p}{l_\infty} = -\frac{3}{2}\langle h^{-3} \rangle \left(1 + \varepsilon^2 C(\text{Re}_H, J_h, J_\phi) \right) + O\left(l_\infty^{-1} \right), \qquad (2.26)$$

where $\langle h^{-3} \rangle$ is the non-dimensional hydraulic aperture of the channel and

$$C(\text{Re}_H, J_h, J_\phi) = K_1 + K_3\text{Re}_H^2$$

---

[7]Full derivatives give the $O(l_\infty^{-1})$ terms which can be neglected on macrolevel, when $L_\infty \gg L_0$. For a periodic channel with $L_\infty = N \cdot L_0$ they are equal to zero exactly.

is the correction to the LCL law due to corrugation, which is defined by the *viscous correction coefficient* $K_1 = \dfrac{(J_h/5 + J_\phi)}{\langle h^{-3} \rangle}$ and the *inertial correction coefficient* $K_3 = \dfrac{26 J_h}{13475 \langle h^{-3} \rangle}$. Here J_h and J_ϕ are the shape factors defined by Eq. (2.3) on p. 33. We remind the reader that $J_h = \|h\|_h^2$ measures the aperture variations, $J_\phi = \|\phi\|_h^2$ measures the curvature of the middle line of the channel. We can see therefore, that at this order of accuracy the inertial coefficient to Darcy's law depends only on aperture variation, and not on the curved shape of the channel.

In dimensional variables the equation (2.26) takes the following form:

$$\frac{\Delta P}{L_\infty} = -\frac{12 \mu Q}{H_h^3} \left(1 + K_1 \varepsilon^2 + \varepsilon^2 K_3 \left(\frac{Q}{\nu} \right)^2 \right), \tag{2.27}$$

where $H_h = 2 H_0 (\langle h^{-3} \rangle)^{-1/3}$ is the *hydraulic aperture* of the fracture [73]. We can see, therefore, that corrections due to weak inertial effects are cubic in the flow rate Q, in agreement with many theoretical and experimental observations (see [36], [25], [47] and others).

Special case: channel with parallel walls. For a channel with curved parallel walls inertial terms are zero at this order of accuracy: $K_3 = 0$. One could suggest that in this case the relationship between the flow rate Q and pressure drop ΔP is no longer cubic in Q. However, calculating higher-order terms of asymptotic expansion (see Section 2.3.3), we obtain the following:

$$\frac{\Delta p}{l_\infty} = -12 \left((1 + K_1^{par} \varepsilon^2) + K_3^{par} \varepsilon^4 \mathrm{Re}_H^2 \right), \tag{2.28}$$

where $K_1^{par} = \int_0^1 (\phi'(x))^2 dx$, $K_3^{par} = \dfrac{1912}{13475} \int_0^1 (\phi''(x))^2 dx$. As we can see from here, the non-linear correction is still quadratic in Re_H for this special case (and therefore the dimensional pressure $P(Q)$ is cubic in flow rate Q).

The linear Darcy law is valid when inertial corrections introduced by Eq. (2.26) are small. This is often considered as a validity criterion for the LCL flow (2.20). In the following section we shall see, that this "global" criterion is not sufficient on microlevel and will formulate a "local" criterion, ensuring smallness of local velocity deviations.

2.3.5   The range of validity of the LCL flow

Usually (see, for example, [73] and [38]), the range of validity of the LCL flow is defined from the curve (2.26). This is justified for a single-phase flow: for most applications the $Q(\Delta P)$-curve is all we need to know. One demands deviations to be less than some tolerance: $K_3(\mathrm{Re}_H\varepsilon)^2/\langle h^{-3}\rangle < \mathrm{Tol}$ and obtains the following condition (the *global criterion*):

$$\mathrm{Re}_H\varepsilon < 35\sqrt{\frac{11\mathrm{Tol}\langle h^{-3}\rangle}{26J_h}} \tag{2.29}$$

However, to study inertial particles we need to make sure that the flow is correctly represented on local level as well, as such particles are very sensitive to the structure of the flow. Let us estimate the first inertial correction to the velocity field, defined by stream function $\psi_0 + \varepsilon\psi_1$ (see Eq. (2.20) and (2.22)). The corrected velocity field can be written in the following form:

$$\tilde{u}_1^x(x,\eta) = \tilde{u}_0^x(x,\eta)\left(1 + a(\eta)h'(x)\frac{\varepsilon\mathrm{Re}_H}{56}\right)$$
$$\tilde{u}_1^z(x,\eta) = -\tilde{u}_0^z(x,\eta)\left(1 + a(\eta)h'(x)\frac{\varepsilon\mathrm{Re}_H}{56}\right) - \tilde{u}_0^x(x,\eta)b(\eta)\eta h''(x)h(x)\frac{\varepsilon\mathrm{Re}_H}{56}. \tag{2.30}$$

where $a(\eta) = \dfrac{1}{5}\left(5 - 28\eta^2 + 7\eta^4\right)$, $b(\eta) = \dfrac{1}{5}\left(1 - \eta^2\right)\left(5 - \eta^2\right)$.

Deviations of horizontal velocity from unperturbed parabolic profile are negligible with a tolerance Tol, when

$$\mathrm{Re}_H\varepsilon < \frac{56\,\mathrm{Tol}}{\max|h'|}, \tag{2.31}$$

(taking into account that $\max[|a(\eta)|] = 1$). Another important parameter is the local slopes of fluid streamlines:

$$\frac{u_1^z(x,\eta)}{u_1^x(x,\eta)} = -h\eta_x' - h''hb(\eta)\eta\frac{\varepsilon\mathrm{Re}_H}{56} = \phi' + \eta\left(h' - h''hb(\eta)\frac{\varepsilon\mathrm{Re}_H}{56}\right) + O(\varepsilon^2\mathrm{Re}_H^2),$$

To obtain a treatable criterion, we have to compare the maximal perturbation to some typical slope s_0. The mean slope over a periodic channel is zero: $\langle h'\rangle = 0$, so we choose

the mean square deviation $\sigma(h') = \sqrt{\langle h'^2 \rangle}$ as this typical slope:

$$\mathrm{Re}_H \varepsilon < 56 \mathrm{Tol} \frac{\sigma(h')}{\max |h'' h|}. \tag{2.32}$$

The global criterion Eq. (2.29) and the local ones Eq. (2.31-2.32) can give sufficiently different estimates for Re_H (compare $\sqrt{\mathrm{Tol}}$ and Tol in the right-hand sides of these equations). This due to the fact that the first-order inertial corrections (linear in Re_H) give no contribution to the flow rate curve, but are non-negligble on the local level. Of course, all these estimates work only in the domain of convergence of the asymptotic series. We are not trying to find the radius of convergence theoretically, but will estimate it numerically in Section 2.4 for some specific channel geometries.

2.4   Application to the sinusoidal channel and numerical verification

In Section 1.3 we have seen that the corrections to the macroscopic Darcy law depend on channel geometry via integral shape factors defined by Eq. (2.3): for any given (smooth) wall shapes $\phi_{1,2}(x)$, one can calculate these shape factors and obtain the $Q(\Delta P)$ curve directly from Eq. (2.26). In this section we will see how the flow rate curves depend on natural geometric parameters in two special cases: channels with shifted sinusoidal walls of equal amplitudes and channels with different amplitudes of top and bottom walls.

2.4.1   Channel with shifted identical sinusoidal walls

Consider a family of channels with identical sinusoidal walls, shifted in x-direction by phase shift α. In non-dimensional variables such channels are described by Eq. (2.5) (on p. 35) with mean corrugation amplitude δ_0, assymetry ratio of wall corrugations $\gamma = 0$ (identical walls) and the phase shift $\alpha \in [-\pi, \pi]$.   The shape factors for this channel are
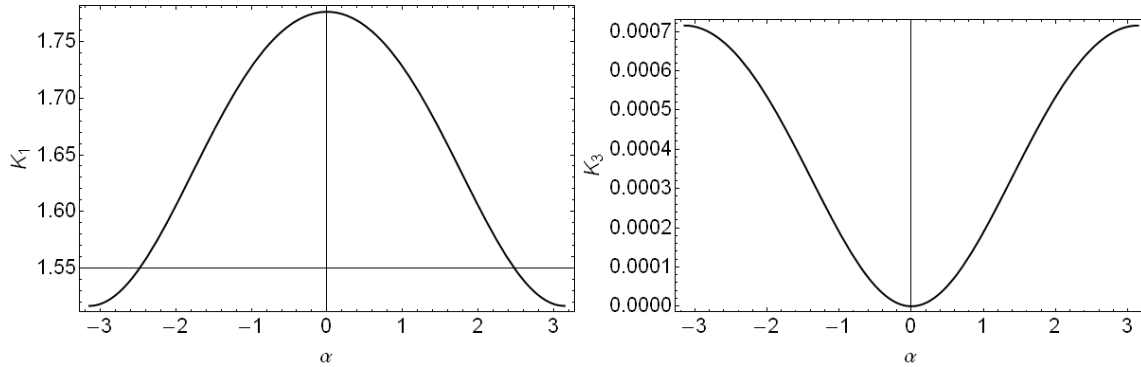
Figure 2.4: *Correction coefficients K_1 and K_3 for a fixed amplitude $\delta_0 = 0.25$ and identical walls ($\gamma = 0$), depending on the phase shift α. Viscous correction coefficient K_1 is maximal for a channel with parallel walls ($\alpha = 0$). The inertial one K_3 is maximal for a mirror-symmetric channel ($\alpha = \pi$).*

defined by Eq. (2.9) . Using Eq. (2.9) we can now calculate the first non-linear correction to the Darcy law as a function of δ_0 and α: $C(\delta_0, \alpha) = K_1(\delta_0, \alpha) + K_3(\delta_0, \alpha)\mathrm{Re}_H^2$. The correction coefficients K_1, K_3 at fixed $\delta_0 = 0.25$ and varying α are plotted in Fig. 2.4. The resulting flow rate curves (showing rescaled pressure drop $\mathrm{Re}_H \Delta p$ versus Re_H) are
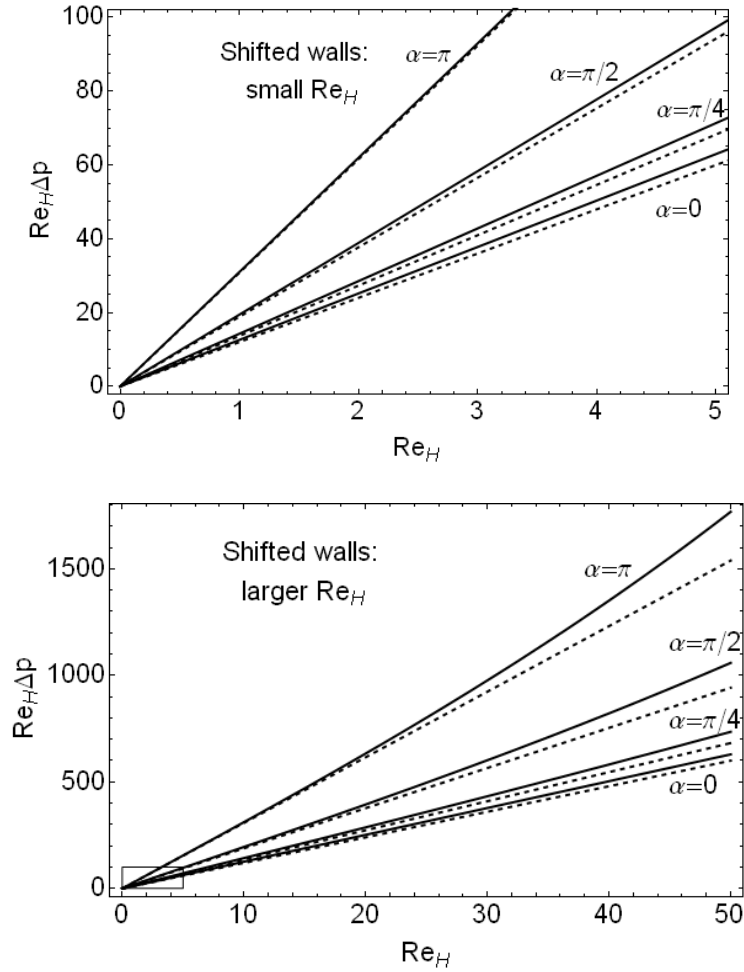
Figure 2.5: *Non-dimensional flow rate curves for a fixed amplitude $\delta_0 = 0.25$ and identical walls ($\gamma = 0$): rescaled pressure drop $Re_H \Delta p$ vs. Reynolds number Re_H for different phase shifts α. Dashed lines correspond to the LCL flow. For small Re_H the deviation from LCL is maximal for the channel with parallel walls. For moderate Re_H it is maximal for the mirror-symmetric channel.*

provided in Fig. 2.4.1. They show that for small Re_H relative deviations from the LCL flow are largest in a channel with parallel walls. For larger Re_H the situation reverses: non-linear effects are most important in a channel with mirror-symmetric walls. Indeed, the change in hydraulic permeability at vanishing Reynolds numbers is mainly due to curved shapes of the streamlines (fluid particles have to go a longer distance than in a straight channel). Parameter K_1, responsible for this effect, is maximal at $\alpha = 0$. For larger Reynolds numbers inertial effects due to repeated acceleration and deceleration of the fluid become important: these are most noticeable in a mirror-symmetric channel

(inertial correction K_3 is maximal at $\alpha = \pi$).

2.4.2   Channel with unequal amplitudes of wall corrugations

In this family the phase shift is fixed to $\alpha = \pi$, but the amplitudes of the upper and lower walls are different: $\gamma \neq 0$ (defined in Eq. (2.8)). They vary from a channel with flat bottom wall ($\gamma = -1$) through mirror-symmetric channel ($\gamma = 0$) to the channel with flat top wall ($\gamma = 1$). The mean amplitude δ_0 remains constant. The shape factors for this case are defined by Eq. (2.10) on p. 35. We remind that in this case J_h (and, therefore, the inertial correction K_3) does not depend on γ (see Fig. 2.6, right). This means that macroscopic behavior of the flow depends the difference in wall corrugations only through viscous correction K_1 (see Fig. 2.6, left) and this dependence is very weak (the correction is of the order of ε^2). The resulting flow rate curves for different values of γ are presented in Fig. 2.7 (one can see that they are almost identical).
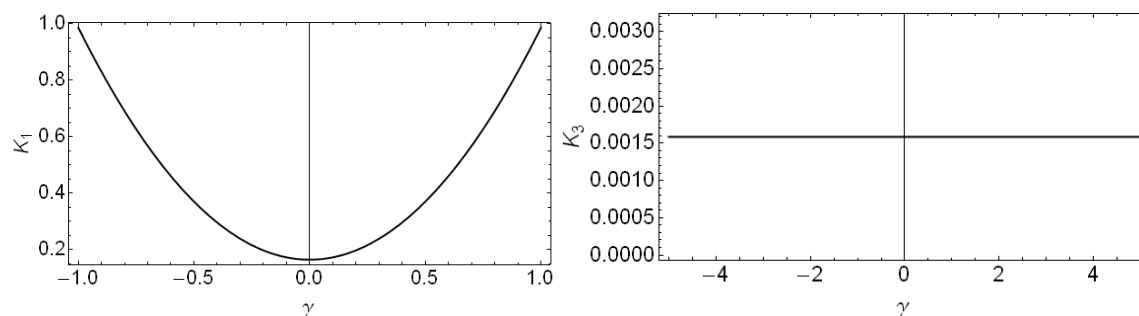

Figure 2.6: *Correction coefficients K_1 and K_3 for a fixed amplitude $\delta_0 = 0.25$, depending on the asymmetry parameter γ. Inertial correction coefficient K_3 does not depend on γ. Viscous correction coefficient K_1 is maximal at $\gamma = \pm 1$ (channel with one flat wall).*
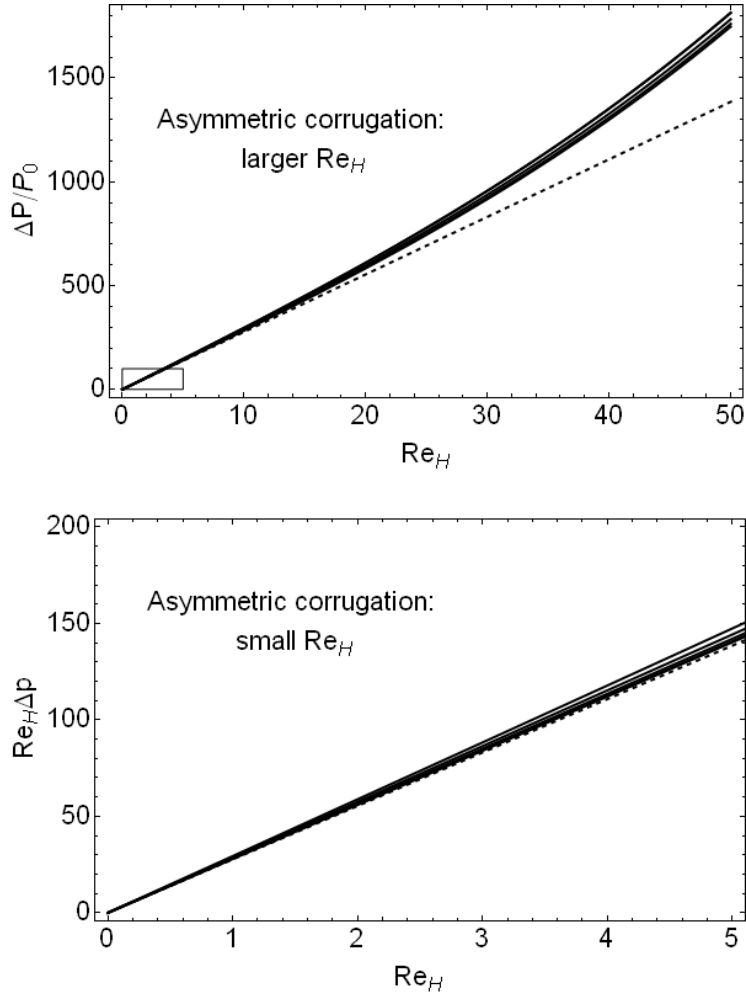
Figure 2.7: *Flow rate curves: rescaled pressure drop $Re_H \Delta p$ v.s. Reynolds number Re_H for different asymmetry parameters γ (at fixed $\delta_0 = 0.25$). Dashed lines correspond to the LCL flow. We can see that macroscopic behavior of the flow is almost insensitive to γ.*

2.4.3 Comparison with Fluent simulations

To validate the asymptotic solution we compared it to numerical simulations performed with Fluent V12 software. Computational domain contained three channel periods $l_\infty = 3$. Constant pressure was set on the inlet ($p_1(0, z) = \Delta p$) and outlet ($p_2(l_\infty, z) = 0$) of the channel. Calculations were performed on a triangular mesh of approximately 73000 nodes, using 2nd order numerical scheme with full coupling between pressure and velocity. For the points in the second and the third periods the periodicity conditions were satisfied almost exactly (the deviations were of order of rounding errors).

As benchmark problem we considered two types of sinusoidal wall corrugation (both with $\varepsilon = 0.1$ and mean corrugation amplitude $\delta_0 = 0.25$): a mirror-symmetric channel ($\alpha = 0$, $\gamma = 0$) and a channel with flat upper wall ($\alpha = \pi$, $\gamma = -1$).

For these channels the shape factors are (see Eq. (2.9-2.10)):

$$\langle h^{-3} \rangle^{mirr} = \langle h^{-3} \rangle^{flat} = \frac{272}{9\sqrt{3}},$$

$$J_h^{mirr} = J_h^{flat} = \frac{8\pi^2}{3\sqrt{3}},$$

$$J_\phi^{mirr} = 0, \;\; J_\phi^{flat} = \frac{8\pi^2}{3\sqrt{3}}.$$

To verify the predictions of Section 2.3.4 the flow rate curves in terms of non-dimensional rescaled pressure $Re_H \Delta p$ and have been constructed by running the simulation with different Δp, calculating the resulting flow rate Q and the corresponding Reynolds number $Re_H = Q/\nu$.

Asymptotic results suggest that the two channels used in simulations should be essentially equivalent for $Re_H > 1$. That is indeed what we observe on Fig. 2.8, where the simulation results for mirror-symmetric channel (red) and channel with flat top wall
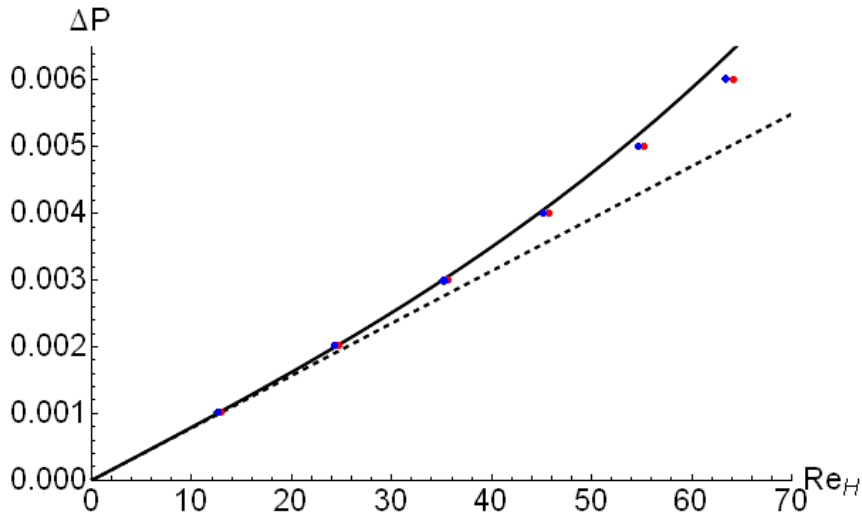

Figure 2.8: *Dimensional pressure drop ΔP versus flow Reynolds number Re_H for a mirror-symmetric channel (red) and a channel with top flat wall (blue). Dashed line corresponds to the LCL flow, solid line is calculated using the asymptotic model developed in this thesis, dots are numerical results exported from Fluent.*

(blue) are plotted along with the theoretical curve defined by Eq. (2.27) (solid curve) and the linear law (dashed line).

Flow streamlines for the LCL flow, the asymptotic solution and numerical simulation results are presented in Fig. 2.9. To compare the asymptotic solution to the numerical one on local level, the x-component of the dimensional velocity field $U_x(X, Z)$ has been exported for sections $X = 1.25$ (section AA) and $X = 1.5$ (section BB) and plotted along with the asymptotic solutions of increasing order at different Re_H numbers. The results for mirror-symmetric channel are presented in Fig. 2.10 and for the channel with flat top wall in Fig. 2.11. As expected, asymptotic solution shows good agreement with numerics for flow Reynolds numbers up to $\mathrm{Re}_H \sim 50$ (which corresponds to $\mathrm{Re}_H \varepsilon \delta_0 = O(1)$). For larger Re_H the asymptotic series diverges (taking into account higher-order terms does not improve the accuracy of the solution).

2.5 Conclusion

In this chapter we considered a single-phase flow through a thin two-dimensional channel with smooth walls of arbitrary shape. Expanding the streamfunction into series of small parameters $\varepsilon = H_0/L_0 \ll 1$ and $\varepsilon \mathrm{Re}_H \ll 1$ we have found a 2nd-order asymptotic solution of Navier-Stokes equations. Using this solution we have derived the first terms of a polynomial relation between the flow rate through the channel and the pressure drop applied at its ends ($\Delta P(Q)$). In full accordance with previous studies, the Q^2 term in this relation vanishes for periodic channels, and an explicit formula has been obtained for the Q^3 term. It depends only on the aperture variation J_h and does not depend on the form of the middle line of the channel. Note that for a parallel channel these corrections are zero and the $\Delta P(Q)$ curve appears linear. However, higher order asymptotics brings a correction proportional to $\varepsilon^3 \mathrm{Re}_H^2$ and therefore confirms the Q^3 correction in this case also. Comparison with numerical simulations by Fluent showed good agreement between numerical and asymptotic solutions both in velocity profiles and $\Delta P(Q)$-curves for Reynolds number less than some critical value. For larger Reynolds numbers the asymptotic series diverges and can no longer be used.
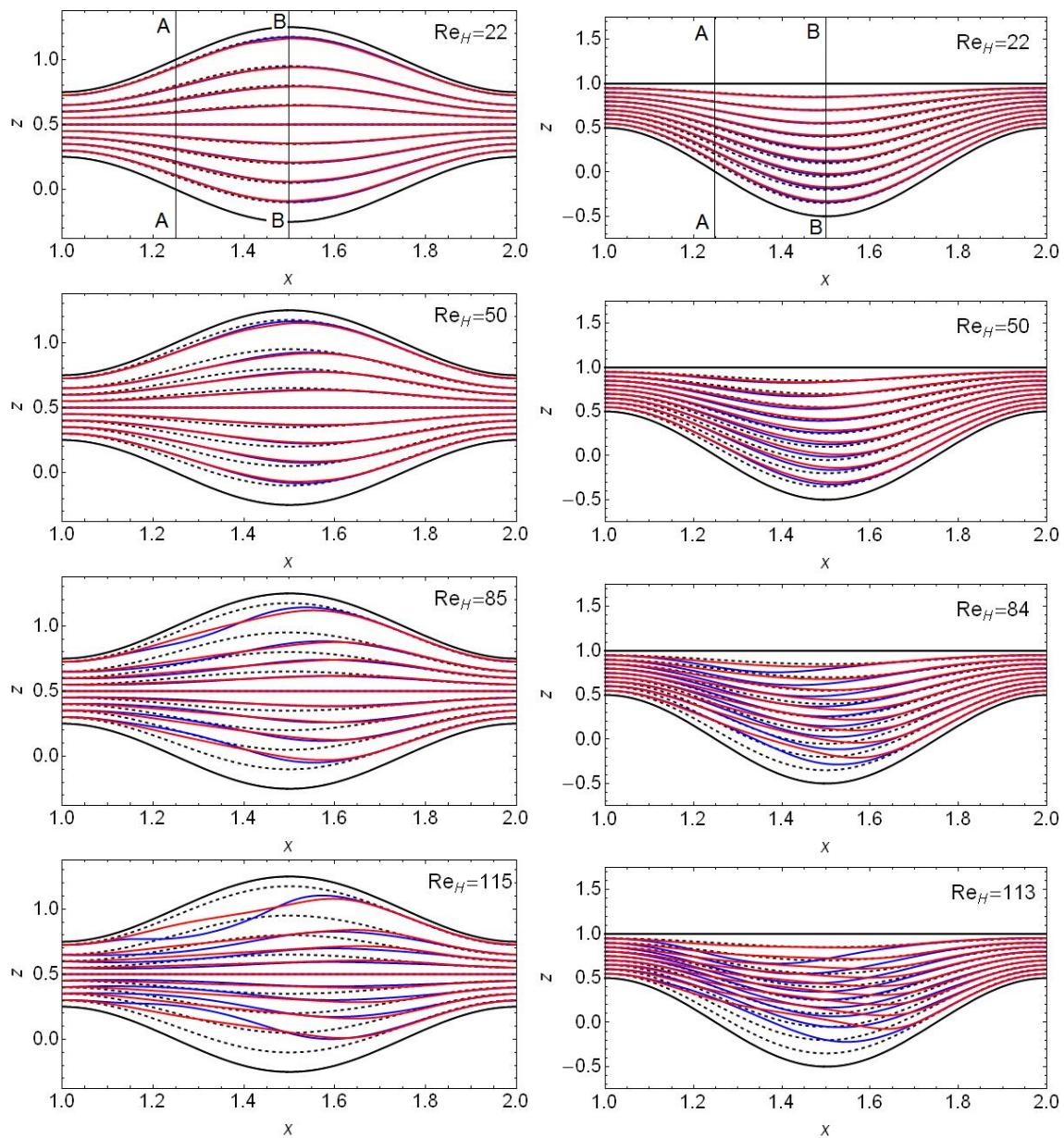
Figure 2.9: *Flow in mirror-symmetric channel (left) and channel with top flat wall (right) at different Reynolds numbers Re$_H$: streamlines for the LCL flow (black, dashed), 2nd order Navier-Stokes asymptotics (solid, blue) and numerical solution from Fluent (solid, red).*
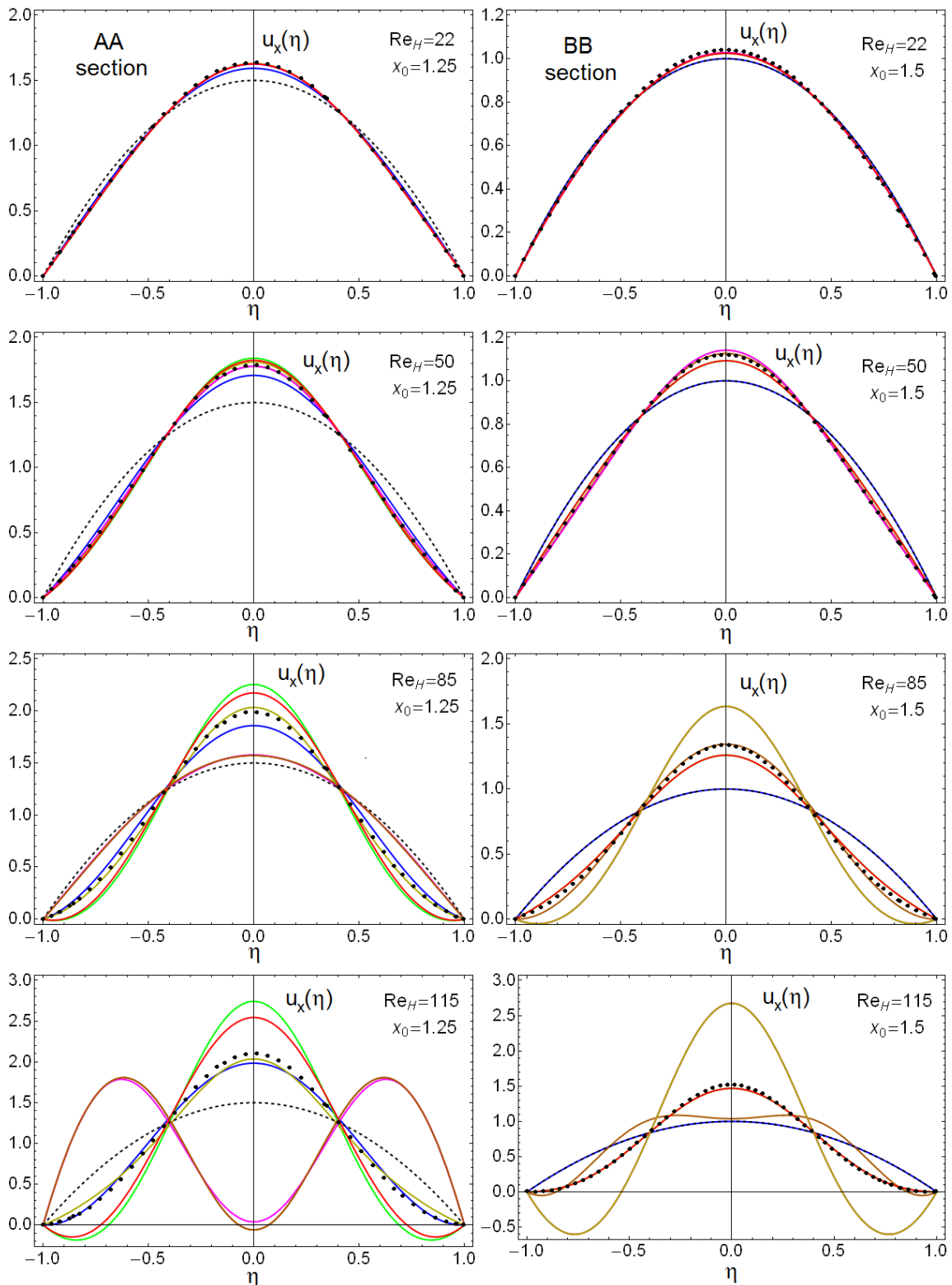
Figure 2.10: *Mirror-symmetric channel: asymptotic velocity profiles of increasing order (colored curves) and Fluent simulations (black dots) at different Re_H. For $Re_H = 22$ and $Re_H = 50$ asymptotic expansion converges to numerical profiles, for $Re_H > 50$ it diverges.*

Figure 2.11: *Channel with flat top wall: asymptotic velocity profiles of increasing order (colored curves) and Fluent simulations (black dots) at different Re_H. For $Re_H = 22$ and $Re_H = 49$ asymptotic expansion converges to numerical profiles, for $Re_H > 50$ it diverges.*

Chapter 3

Transport of weakly-inertial particles in a periodic channel

In the previous chapter we considered a single-phase flow through a channel with wavy walls. In this chapter we consider the motion of inertial particles immersed into this flow. Particles are assumed to be much smaller than th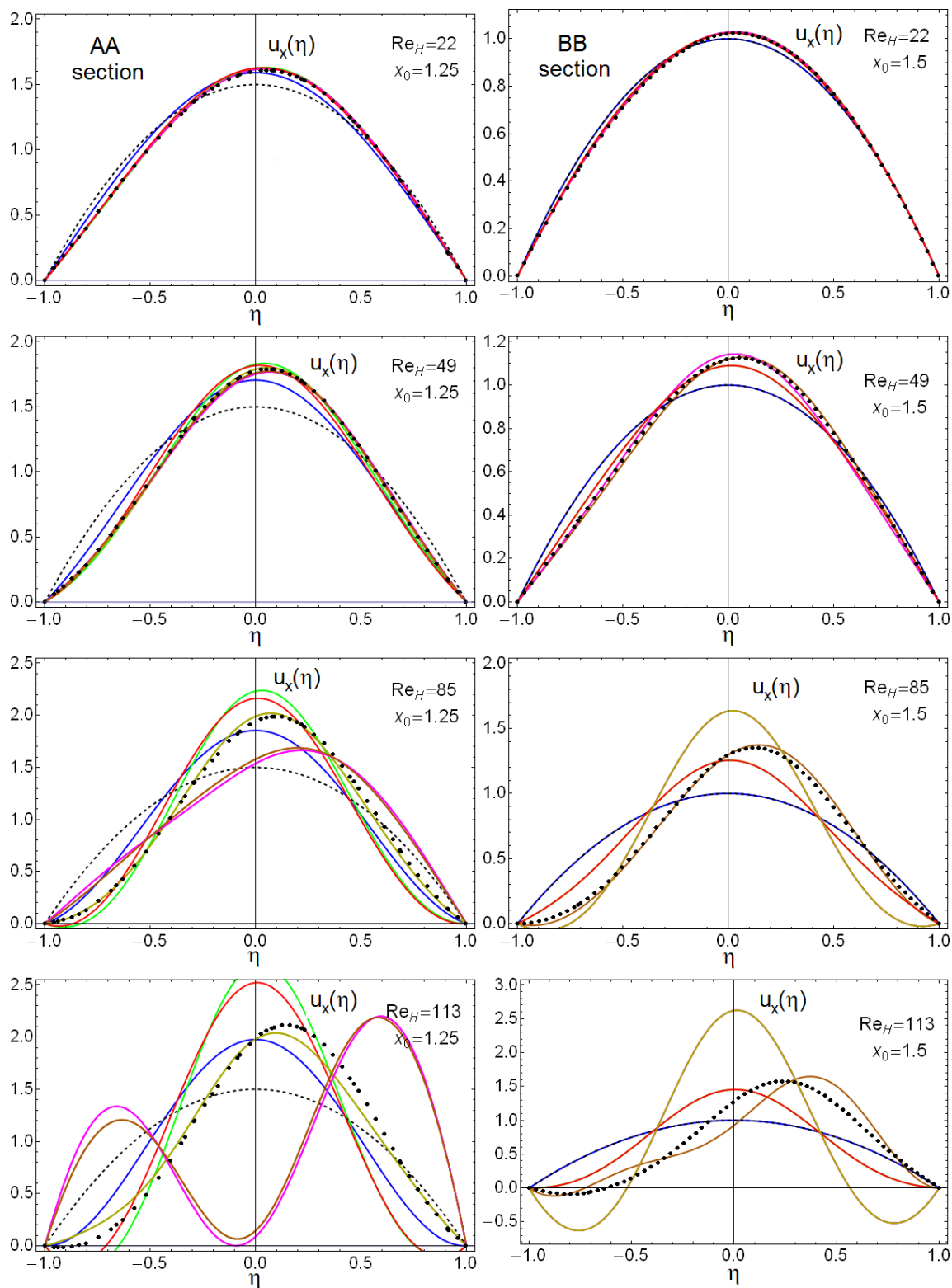e gap, non-brownian and isolated (they do not interact with each other and modify the flow only locally). Unlike passive tracers, inertial particles have the freedom to migrate between fluid streamlines and eventually focus to some optimal trajectories. The goal of this chapter is to investigate the possibility of this focusing effect in wavy channels and to estimate its influence on macroscopic transport properties. We begin by neglecting all the effects due to proper inertia of the fluid and use the LCL model for the flow and simplified Maxey-Riley equations for particle motion. In the limit of small particle response times (weakly-inertial particles), we reduce Maxey-Riley equations to the asymptotic form and construct a Poincaré map of particle positions at the end of each period. This map contains all information on long-term particle behavior. Using it, we find the conditions for particle focusing in the LCL flow and calculate inertial corrections to sedimentation length in presence of gravity. The main results of this chapter have been presented at the 20th Congrès Français de Mécanique in 2011 [49].

3.1   Introduction

As discussed in Chapter 1, small heavy non-brownian particles carried by a periodic flow tend to focus to some preferential trajectories. The general mechanism of such focusing has been described in Section 1.2. Any heavy inertial particle wants to make its trajectory straight, while interaction with fluid (drag force) tends to equilibrate particle and fluid velocities. When particle inertia is weak compared to drag, particles will follow fluid streamlines[1] closely - but only locally. Even if flow and particle velocities are close at every point, particles can slowly migrate across the stream and converge, after a long time, to some preferential trajectory, usually called the *attractor*. This trajectory is close to one of the fluid streamlines, that we call the *attracting streamline*. The attractor is common for all nearby particles: they all focus to it sooner or later.

Note that the classical definition of the attractor is more general than this one [29]: for the n-dimensional dynamical system the attractor can be any manifold of dimension $m < n$ to which solutions converge after a long time (see Fig. 1.1). In this sense there is always an attractor for inertial particles in a periodic flow, because particle dynamics is dissipative and occurs in a bounded region of four-dimensional phase space (because of periodicity). However, this attractor does not necessarily look like an attracting trajectory. For example, in a uniform flow all particles eventually take the velocity of the fluid (the phase volume shrinks to zero), but there is no focusing in the physical space. In this case the attractor is a two-dimensional hyperplane in the four-dimensional phase space $(X_p, Z_p, \dot{X}_p, \dot{Z}_p)$ which projects onto the whole physical domain.

The goal of this chapter is to study the influence of this focusing effect on particle transport in a corrugated channel. Wall corrugation imposes curved shapes upon fluid streamlines inside the channel. Following the argument above, we should expect heavy particles to focus to one of these streamlines (the least "curved" one) after many periods. However, the difference between particle and fluid density leads not only to inertial focusing, but also to particle sedimentation due to gravity. In a horizontal channel these effects work against each other and focusing is possible only when the flow rate is high. In this case a considerable part of particles can avoid sedimentation and travel long distances on

---

[1]We deal with a stationary flow and will make no difference between streamlines and fluid trajectories.

the attractor. For lower flow rates inertial effects are not strong enough to balance out the gravity, but can lead to slower particle sedimentation and to the increase of sedimentation length. In this chapter we find the explicit conditions for attractor existence, depending on the flow rate and channel geometry (trapping diagram). We also calculate the percentage of particles that avoid sedimentation (for high flow rates) and estimate the sedimentation length (for lower flow rates).

Particles are taken to be much smaller than the gap of the channel and their density is comparable to that of the fluid. In addition, we assume that they do not interact and do not modify the main flow. One can show that under these conditions the influence of inertia on particle motion is weak and, in the long term, particle velocities can be obtained by perturbation of the fluid velocity field. However, even if at any given point the difference between particle and fluid velocities is small, their long-term behavior is completely different.

For the moment proper inertia of the fluid is completely neglected: we use the LCL (Local Cubic Law) model for the flow and Maxey-Riley equations for particle motion [44]. Taking fluid inertia into account leads to the appearance of a cross-stream force (widely known as "lift") acting on particles that lead or lag the flow. Particle migration under the influence of lift will be considered in the next chapter.

Outline of the chapter

We start by defining particle motion equations. In Section 3.2 we write the full Maxey-Riley equations in non-dimensional variables and introduce the parameter measuring particle inertia - particle response time τ. Then we reduce them to an asymptotic form in the limit $\tau \ll 1$ and estimate by order of magnitude different terms of this asymptotic equation. These estimates suggest that for a weakly-corrugated channel we can neglect the Basset force, but should keep the Faxen corrections (which are often neglected under assumption that the particle size is small).

Having at hand the simplified motion equations, we proceed to study particle migration across the channel in Section 3.3. To do this we construct the Poincaré map of particle positions at the end of each corrugation period, where particle position is tracked by the η-variable defined in Chapter 2. This reduces the problem to calculation of a migration

function $f(\eta)$ which contains all information on long-term particle behavior. For the LCL flow $f(\eta)$ can be calculated explicitly and depends on channel geometry (via two integral shape factors) and on the non-dimensional gravity number (inverse of Froude number). We use it to construct the trapping diagram, that predicts focusing/sedimentation regimes depending on gravity number and channel geometry.

Finally, in Section 3.4 we apply the results of Section 3.3 to a channel with shifted sinusoidal walls and compare them to numerical simulation using the second-order Maxey-Riley equations [44].

3.2 Particle motion equations

3.2.1 The full Maxey-Riley equations

The Maxey-Riley equations (in the form derived in [44] with corrected added mass term [4]) read:

$$
\begin{aligned}
m_p \frac{d\vec{V}_p}{dt} &= (m_p - m_f)\vec{g} + m_f \frac{D\vec{U}_f}{Dt} - \frac{m_f}{2}\left(\frac{d\vec{V}_p}{dt} - \frac{D}{Dt}\left(\vec{U}_f(\vec{X}_p) + \frac{a^2}{10}\nabla^2\vec{U}_f\right)\right) \\
&- 6\pi a\mu\left(V_p - \vec{U}_f(\vec{X}_p) - \frac{a^2}{6}\nabla^2\vec{U}_f\right) \\
&- 6\pi a^2\mu \int\limits_{-\infty}^{t} \frac{1}{\sqrt{\nu\pi(t-t')}}\frac{d}{dt'}\left[\vec{V}_p - \vec{U}_f(\vec{X}_p) - \frac{a^2}{6}\nabla^2_X\vec{U}_f\right]dt',
\end{aligned}
$$

$$(3.1)$$

where $\vec{V}_p$ and $\vec{U}_f$ are the particle and fluid velocities respectively, $\vec{g} = g\vec{e}_g$, is the gravity acceleration, a and m_p are the radius and the mass of the particle and m_f is the mass of fluid displaced by the particle. This equation takes into account the following forces (in order of appearance): the gravity and buoyancy forces, Tchen's force due to pressure gradient of the unperturbed flow, the added mass force, the drag and the Basset force due to insteadiness of the disturbance flow around the particle.

The terms proportional to the laplacian of the velocity field ($\sim a^2\nabla^2\vec{U}_f$) are usually referred to as *Faxen corrections* [22] and are due to local non-uniformity of the fluid flow on the particle scale. They are very often neglected under assumption that particle size a

is small compared to typical length scale of the flow L_0. However, even if these terms are small compared to the fluid velocity $\vec{U}_f$, they can compete against particle slip velocity $\vec{V}_s = \vec{V}_p - U_f(\vec{X}_p)$, especially in weakly-inertial regime. The integral term (Basset force) is due to the non-stationarity of the disturbance flow around the particle. In this thesis we will assume this disturbance flow is quasi-steady, so (as shown in the next section) the Basset force can be neglected.

For the moment we keep all the terms in Eq. (3.1) and consider its asymptotic form in the limit of small particle response times (weakly-inertial regime). Then we estimate the contribution of each term in this asymptotic equation and formulate the conditions under which they can be neglected.

3.2.2 Asymptotic equations for small response times

In this chapter we use the corrugation period L_0 as a length scale for both spatial coordinates and the mean velocity of the unperturbed flow U_0 for both velocity components:

$$
\begin{aligned}
& x_p = X_p/L_0, \ z_p = Z_p/L_0, \ T_0 = L_0/U_0, \\
& v_p^x = V_p^x/U_0, \ v_p^z = V_p^z/U_0, \ u_f^x = U_f^x/U_0, \ u_f^z = U_f^z/U_0.
\end{aligned}
\tag{3.2}
$$

Note that non-dimensional variables defined this way are different from those used for the single-phase flow (see Eq. (2.1) and (2.14) of Chapter 2).

In non-dimensional variables defined by Eq. (3.2) the Maxey-Riley equations read:

$$
\begin{aligned}
\frac{d\vec{x}_p}{dt} &= \vec{v}_p, \\
\frac{d\vec{v}_p}{dt} &= -\frac{1}{\tau}\left(\vec{v}_s - \frac{\chi_L^2}{6}\nabla^2\vec{u}_f\right) + \left(1 - \frac{3R}{2}\right)\vec{G} + \frac{3R}{2}\frac{D}{Dt}\left(\vec{u}_f - \frac{\chi_L^2}{20}\nabla^2\vec{u}_f\right) + \\
&\quad + \frac{3\sqrt{R}}{\sqrt{2}\sqrt{\tau}}\int_{-\infty}^{t}\frac{1}{\pi(\sqrt{t-s})}\frac{d}{ds}\left(\vec{v}_s - \frac{\chi_L^2}{6}\nabla^2\vec{u}_f\right)ds,
\end{aligned}
\tag{3.3}
$$

where $\vec{v}_s = \vec{v}_p - \vec{u}_f(\vec{x}_p)$ is the non-dimensional slip velocity, $\chi_L = \dfrac{a}{L_0}$ is the non-dimensional particle radius and $R = \dfrac{2\rho_f}{2\rho_p + \rho_f}$ is the particle/fluid density ratio. The non-dimensional gravity vector $\vec{G} = \dfrac{\vec{e}_z}{\mathrm{Fr}}$, where $\mathrm{Fr} = \dfrac{U_0^2}{L_0 g}$ is the *Froude number* measuring

inertia forces compared to the force of gravity. The main parameter measuring particle inertia is the *non-dimensional response time* $\tau = \mathrm{St}/R$, where St is the *particle Stokes number* which can be written as $\mathrm{St} = \frac{2}{9}\mathrm{Re}_L\chi_L^2$ with $\mathrm{Re}_L = U_0 L_0/\nu$ or $\mathrm{St} = \frac{2}{9}\varepsilon\mathrm{Re}_H\chi_H^2$ with $\chi_H = \dfrac{a}{H_0}$ being the particle size related to the mean gap of the channel.

When $\tau \ll 1$, particles quickly forget their initial conditions and, in the long term, their velocities do not deviate much from that of a fluid point (*weakly-inertial regime*). For $\tau \gg 1$ particle motion is mostly governed by gravity (or other external forces), and interaction with fluid can be considered as a small correction (*ballistic regime*). In the intermediate case $\tau = O(1)$ particle dynamics can be very complex. In this thesis we consider particles that are much smaller than channel gap: $\chi_H \ll 1$. Therefore, the response time $\tau = \dfrac{2}{9}\dfrac{(\varepsilon\mathrm{Re}_H)\chi_H^2}{R}$ will always be small unless particles are much heavier than the fluid ($R \ll 1$) or flow Reynolds number is large ($\varepsilon\mathrm{Re}_H \gg 1$). For the rest of this chapter we focus on the asymptotic regime with $\tau \ll 1$, except in Section 3.5.

Motion equations (3.3) are singulary perturbed in the limit $\tau \to 0$:

$$\dot{\vec{x}}_p = \vec{v}_p,$$
$$\tau\dot{\vec{v}}_p = (\vec{u}_f - \vec{v}_p) + \tau\,(\ldots) + \tau^{3/2}\,(\ldots).$$

Physically it means that the system has two time scales: hydrodynamic time $T_0 = L_0/U_0$ and particle response time $\tau \cdot T_0$. It is known (see [41], [20]) that for small τ solutions of this equation will converge at an exponential rate $\exp(-t/\tau)$ to the solutions of the following first-order equation[2]:

$$\dot{\vec{x}}_p = \vec{v}_\tau(\vec{x}_p),$$
$$\vec{v}_\tau(\vec{x}_p) = \vec{u}_f(\vec{x}_p) + \tau\vec{v}_1(\vec{x}_p) + \tau^{3/2}\vec{v}_{3/2}(\vec{x}_p) + O(\tau^2),$$

(3.4)

with

$$\vec{v}_1(\vec{x}) = \left(\frac{3R}{2} - 1\right)\left((\vec{u}_f \cdot \vec{\nabla})\vec{u}_f - \vec{G}\right) + \frac{3R}{4(\varepsilon\mathrm{Re}_H)}\Delta\vec{u}_f + O(R\chi_L^2),$$
$$\vec{v}_{3/2}(\vec{x}) = \frac{3\sqrt{R}}{\sqrt{2}}\int_{-\infty}^{t}\frac{1}{\sqrt{\pi(t-s)}}\frac{d}{ds}\left(\vec{v}_1 - \frac{3R}{4(\varepsilon\mathrm{Re}_H)}\Delta\vec{u}_f\right)ds.$$

---

[2]In terms of dynamical systems this equation corresponds to the slow manifold: a 2D attracting manifold in the 4D phase space of particle positions and velocities.

We can see that the Faxen corrections arise in the first order term of the asymptotic expansion[3] and therefore can not be neglected a priori, unless particles are much heavier than the fluid ($R \ll 1$) or flow Reynolds number based on the corrugation is large ($\varepsilon \mathrm{Re}_H \gg 1$). The Basset term is proportional to $\tau^{3/2}$ and therefore can be neglected at small τ.

Particle behavior in the asymptotic regime is fully determined by the velocity field $\vec{v}_\tau(\vec{x}_p)$. Unlike the fluid velocity field, the divergence of $\vec{v}_\tau$ is non-zero [41]: particle flow is compressible. Particles can therefore accumulate on well-defined manifolds like limit cycles or equilibrium points. In a recent work by Haller and Sapsis [57] a necessary condition was formulated for the existence of a limit cycle τ-close to a closed fluid streamline S_0:

$$I_0(S_0) = \int_{S_0} \vec{v}_1 \cdot \vec{n} ds = 0,$$
$$I_1(S_0) = \int_{S_0} \frac{\partial}{\partial n} (\vec{v}_1 \cdot \vec{n}) \, ds < 0, \tag{3.5}$$

where $\vec{n}$ is the outer normal of the streamline. These conditions are based on the local rate of particle migration across the fluid streamlines. The former means that the net drift of a particle over a streamline period should be zero in the vicinity of the attractor. The latter manifests the fact that particle volumes shrink in the vicinity of the attractor. This criterion (generalized to non-inertial reference frames) is used in Chapter 5 to find the limit cycle for dust particles in a vortex pair.

Conditions (3.5) allow to find a closed fluid streamline S_0, that attracts nearby inertial particles (attracting streamline). In a periodic channel flow without recirculations there are no closed streamlines. However, an analogous criterion for particle focusing can be formulated using Poincaré map of particle positions at the end of each period.

---

[3]The term $O(R\chi_L^2)$ in $\vec{v}_1$ corresponds to Faxen correction to the added mass. This terms is always small and will be neglected everywhere.

3.3   Focusing and sedimentation of weakly-inertial particles in a periodic LCL flow

3.3.1   Poincaré map of particle motion through periodic channel

The best way to describe migration of a particle across the channel is to track its cross-channel coordinate $\eta_p(t) = \eta(x_p(t), z_p(t))$ (where $\eta(x, z)$ is defined on p. 38 by Eq. (2.17)). The instant migration rate can be defined as $\dfrac{d\eta_p}{dt} = \vec{\nabla}\eta \cdot \vec{v}_\tau$, which is easily calculated once the particle velocity field is known. However, the migration rate defined this way is not a very convenient parameter, because it can change sign many times along the particle trajectory and does not give immediate information on long-term particle behavior.
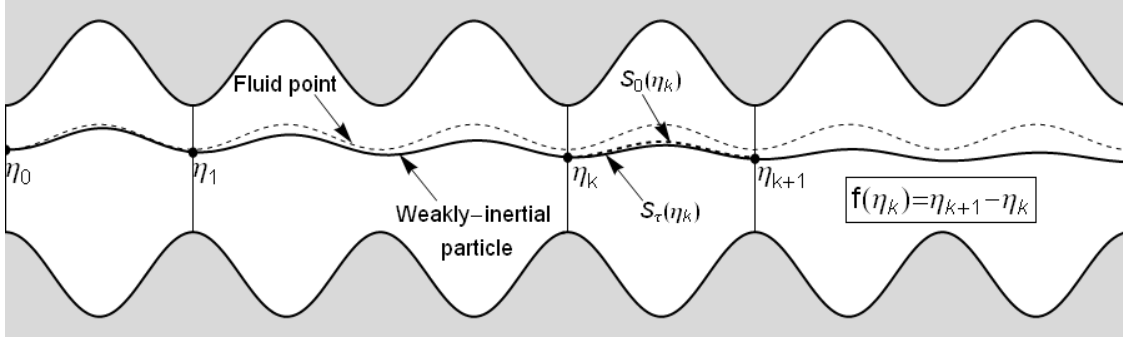

Figure 3.1: *Slow migration of weakly-inertial particles.   Locally, particle trajectory $S_\tau(\eta_k)$ does not deviate far from a streamline $S_0(\eta_k)$, but long-term behaviors are different (compare trajectories of a fluid point (dashed) and a particle (solid) released from the same point).*

To quantify the net particle migration at long term, we build a *Poincaré map* for the η-coordinates of the particle at the end of each corrugation period: $\eta_k = \eta(\vec{x}_p(t_k))$, at time t_k such that $x_p(t_k) = k \in \mathbb{N}$ (corrugation period is equal to 1 in non-dimensional variables). This sequence $\{\eta_k\}_{k=0}^\infty$ provides all necessary information about long-term focusing and sedimentation rates. At small τ particles are governed by first-order motion equations (3.4) so their trajectories depend only on initial positions (and not on initial velocities). Therefore, the η-coordinate of the particle at the end of each period satisfies the following recurrence formula:

$$\eta_{k+1} = \eta_k + f(\eta_k), \tag{3.6}$$

where $f(\eta_k) = \int\limits_{t_k}^{t_{k+1}} \vec{\nabla}\eta \cdot \vec{v}_\tau(\vec{x}_p(t))dt$ is the variation of η along the particle trajectory $S_\tau(\eta_k)$ starting at point (k, η_k). Assuming that the particle does not deviate much from a fluid streamline over one period, we can replace the integration over the trajectory $S_\tau(\eta_k)$ with integration over a fluid streamline $S_0(\eta_k)$ (see Fig. 3.1):

$$f(\eta_k) \approx \int\limits_{t_k}^{t_{k+1}} \vec{\nabla}\eta \cdot \vec{v}_\tau(\vec{x}_0(t))dt = \int\limits_{S_0} \vec{\nabla}\eta \cdot \vec{v}_\tau(\vec{x}_0(s))/|\vec{u}_f(\vec{x}_0)|ds.$$

Using this function it is easy to find the conditions of particle focusing and estimate the rates of particle migration.

"Focusing" implies that after many periods particles will accumulate on some attracting trajectory (which has to be periodic and $O(\tau)$-close to a fluid stream in the asymptotic regime).
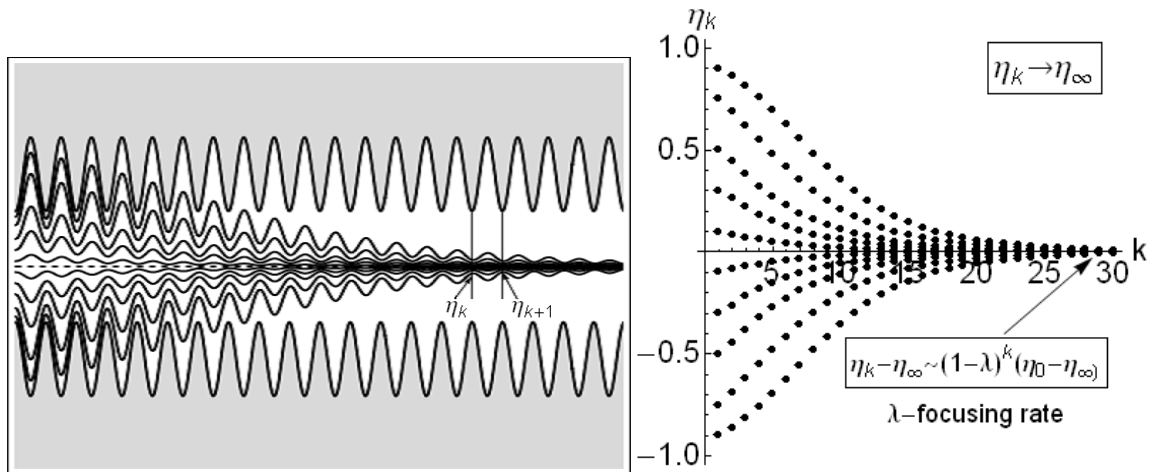
Figure 3.2: *Focusing of weakly inertial particles: particle trajectories $\vec{x}_p(t)$ converge to an attractor (left) and their Poincaré sections $\{\eta_k\}$ converge to a fixed point η_∞(right).*

This attracting trajectory (or, shorter, *attractor*) corresponds to a stable fixed point of the difference equation (3.6):

$$\eta_\infty : f(\eta_\infty) = 0, \, f'(\eta_\infty) < 0, \tag{3.7}$$

(the stability condition reads $|1 + f'| < 1$, but its second part $f'(\eta_\infty) > -2$ is satisfied

automatically under assumption that $f(\eta) = O(\tau) \ll 1$). One can show that for a flow without recirculations Eq. (3.7) coincide exactly with Haller-Sapsis integrals defined by Eq. (3.5).

The attractor does not necessarily trap all particles in the channel. The basin of attraction for η_∞ is bounded by the nearest unstable fixed points ("repellers"):

$$\eta_{rep} : f(\eta_{rep}) = 0, f'(\eta_{rep}) > 0. \tag{3.8}$$

Indeed, if particle trajectories do not intersect each other, $f(\eta)$ can not change its sign without crossing the zero and the direction of migration between η_∞ and neighboring η_{rep}'s is fully determined by the sign of $f(\eta)$ (see the sketch on Fig. 3.3). Therefore, to
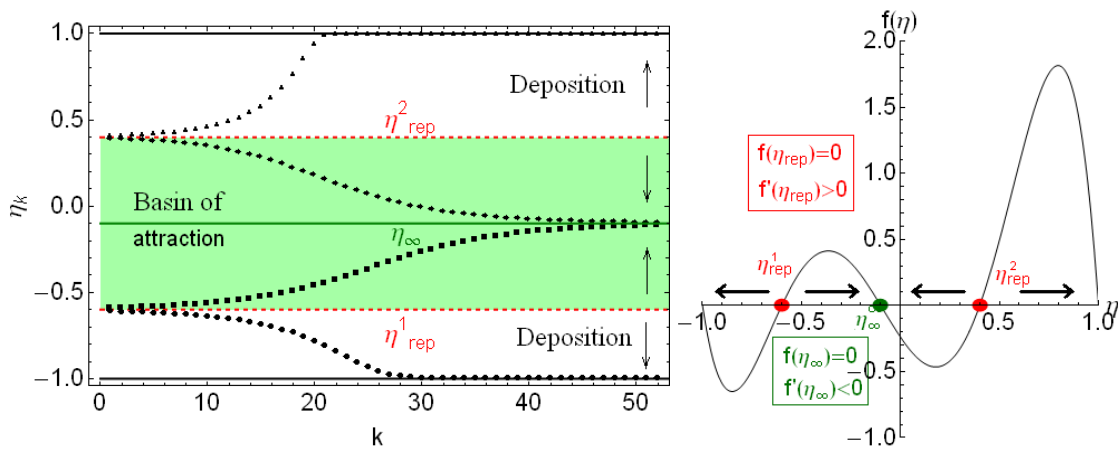
Figure 3.3: *Attractor η_∞ with its basin of attraction (left), and the corresponding migration function (right). Arrows indicate the direction of particle migration.*

make some general conclusions about particle behavior it is sufficient to find the roots of $f(\eta)$ and identify their type ("attractor" or "repeller"). Different regimes of particle behavior correspond to different number and type of roots. In the following sections we will use this idea to construct focusing diagrams that predict asymptotic particle behavior in the LCL flow through channels of different geometry.

Using the Poincaré map we can also estimate how fast do particles converge to the attractor. Expanding the right-hand side of the difference equation (3.6) in the vicinity of

the fixed point:

$$f(\eta_k) = f(\eta_\infty) + (\eta_k - \eta_\infty)f'(\eta_\infty) + O(\eta_k - \eta_\infty)^2,$$

we are led to (for $k \gg 1$):

$$\eta_k - \eta_\infty = (1 - \lambda)^k(\eta_0 - \eta_\infty). \tag{3.9}$$

The constant $\lambda = -f'(\eta_\infty)$ can be considered as a "trapping rate" of the attractor. The characteristic non-dimensional focusing time T_f can be found from the equation $(1 - \lambda)^k = \exp{(-k/T_f)}$ for large k.

Moreover, we can estimate the number of periods it takes for a particle to migrate from point η_1 to η_2, provided that there are no fixed points on its way ($f(\eta) \neq 0 \; \forall \eta \in [\eta_1; \eta_2]$):

$$n(\eta_1, \eta_2) \approx \int_{\eta_1}^{\eta_2} \frac{d\eta}{f(\eta)} + O(1). \tag{3.10}$$

This approximation is obtained by replacing the finite-difference Eq. (3.6) with its differential counter-part under assumption that $|f(\eta)| \ll 1$. This formula will be useful for calculation of maximal propagation length for sedimenting particles.

In the following section we calculate the Poincaré map $f(\eta)$ for the LCL flow and use it to find the conditions for particle focusing in a periodic channel.

3.3.2 Migration function for the LCL flow

In this section we calculate the migration function $f(\eta)$ for the LCL flow. The stream function of the LCL flow in non-dimensional variables (3.2) is defined by Eq. (2.20):

$$\tilde{\psi}(\eta) = \frac{\varepsilon}{4}\left(3\eta - \eta^3\right),$$

where $\eta(x_p, z_p) = \dfrac{z_p/\varepsilon - \phi(x_p)}{h(x_p)}$ is the cross-channel coordinate and ε arises because of different velocity scales used here and in Chapter 2.

To calculate the migration function $f(\eta)$ we take into account the fact that the stream function $\tilde{\psi}(\eta)$ does not depend on x_p explicitly. It means that fluid point trajectories $S_0(\eta_k)$ are nothing but η isolines: $\eta(x_0(t), z_0(t)) \equiv \eta_k$. The migration functions in this case is easy to calculate:

$$f(\eta_k) \approx \int\limits_{S_0(\eta_k)} \vec{\nabla}\eta \cdot \vec{v}_\tau(\vec{x}_0(s))/|\vec{u}(\vec{x}_0(s))|ds \approx \frac{\tau}{\Psi'(\eta_k)} \int\limits_0^1 \frac{(\vec{\tilde{v}}_1(x', \eta_k) \cdot \vec{n})}{\tilde{u}_x(x', \eta_k)}dx' + O(\tau^{3/2}),$$

(3.11)

where $\vec{n} = \vec{\nabla}\psi/|\vec{\nabla}\psi|$ is the normal vector to the fluid streamline and $\vec{\tilde{v}}_\tau$ is the particle velocity field expressed in channel variables $\vec{v}_\tau(x, z) = \vec{\tilde{v}}_\tau(x, \eta(x, z))$. The first correction to particle velocity:

$$\vec{v}_1(\vec{x}) = \left(\frac{3R}{2} - 1\right)\left((\vec{u}_f \cdot \vec{\nabla})\vec{u}_f - \vec{G}\right) + \frac{3R}{4(\varepsilon \text{Re}_H)}\Delta\vec{u}_f$$

(3.12)

can be calculated as a function of x and η. The fluid velocity field can be represented in (x, η) variables:

$$\tilde{u}_f^x(x_p, \eta_p) = \frac{\tilde{\psi}'}{\varepsilon h(x)}, \quad \tilde{u}_f^z(x_p, \eta_p) = \frac{\tilde{\psi}'(h'\eta + \phi')}{h(x)}.$$

Substituting it into Eq. (3.11), integrating over the channel period and taking into account the periodicity of $h(x)$, $\phi(x)$, we get[4]:

$$f(\eta) \approx \tau \left(\frac{3R}{2} - 1\right) \frac{9\varepsilon^2 J_h}{8\tilde{\psi}'(\eta)}p(\eta; \beta, \gamma_z) + O\left(\tau^{3/2}\right),$$

(3.13)

where

$$p(\eta; \beta, \gamma_z) = (\eta + \beta)(\eta^2 - 1)^2 + \gamma_z$$

(3.14)

is a structure polynomial that defines the type and number of roots of $f(\eta)$.

---

[4]Note that Faxen corrections and the term proportional to G_x integrate to zero over a period. That means that longitudinal gravity and "parabolicity" of the velocity profile give no contribution to net particle migration.

The structure of the migration function depends on two parameters:

$$\beta = J_{\phi h}/J_h = \frac{||\phi_2'||_h^2 - ||\phi_1'||_h^2}{||h'||_h^2} \tag{3.15}$$

is the *corrugation asymmetry factor* of the channel and

$$\gamma_z = \frac{8 G_z}{9 \varepsilon J_h} \tag{3.16}$$

is the *rescaled gravity number*.

The geometry factors J_h and J_ϕ are the same as defined by Eq. (2.3) in Chapter 2: $J_h = ||h'||_h^2$ measures the aperture variation, and $J_{\phi h} = ||\phi_2'||_h^2 - ||\phi_1'||_h^2$ is the difference between corrugation norms for the upper and lower walls. The aperture variation J_h is always positive. Therefore, the corrugation asymmetry factor β is positive when the upper wall is more corrugated than the lower one, and negative in the opposite case.

To define different regimes of particle behavior depending on the corrugation asymmetry factor β and the gravity number γ_z, we should find the structure of the function $p(\eta; \beta, \gamma_z)$. More precisely, we need to know the number and type of its roots, because it is in these points that the direction of migration changes. These roots are investigated in the next section.

3.3.3 Particle focusing in the absence of gravity

In the absence of transversal gravity ($\gamma_z = 0$) the migration function $f(\eta)$ has three roots: $\eta = \pm 1$ (channel walls) and $\eta_* = -\beta$.

When $|\beta| < 1$ (the difference in wall corrugations is smaller than the aperture variation: $|J_{\phi h}| < J_h$), the root $\eta_* = -\beta$ lies inside the channel and corresponds to a fixed point of the Poincaré map (see Eq. (3.6)). To find out if this fixed point is stable, we calculate the derivative of the migration function at this point:

$$f'(-\beta) = -\tau \left(\frac{3R}{2} - 1 \right) \frac{3\varepsilon J_h}{4} (1 - \beta^2), \; |\beta| < 1 \tag{3.17}$$

When $J_h \neq 0$ (channel walls are not parallel), it is always negative when $R < 2/3$ and

always positive when $R > 2/3$: heavy particles are focused to the streamline $\eta_\infty = -\beta$ and light particles are repulsed to the walls.

When $|\beta| > 1$ (difference in wall corrugations is larger than the aperture variation: $|J_{\phi h}| < J_h$) the root $\eta_* = -\beta$ does not belong to the channel and $f(\eta)$ does not change sign. Heavy and light particles migrate in opposite directions and approach the walls without touching them. More precisely, heavy particles go to the wall with smaller corrugation norm $||\phi_i'||_h$ and light particles go in the opposite direction.

The physical sense of this behavior is the following. Weakly inertial particles are bound to follow fluid streamlines at least approximately, but they can slowly migrate between them and choose the one they like best. In our model the principal driving force of this migration is the different curvatures of fluid streamlines. Heavy particles, following a curved trajectory, experience a centrifugal force that makes them migrate to the zones where streamline curvature is minimal. In contrast, light particles migrate to zones with high streamline curvature, driven there by a centrifugal pressure gradient of the flow (leading to a centripetal Tchen's force). This is, in particular, what we observe when $|\beta| \geq 1$: heavy particles approach the"flatter" wall , while light particles go to the "wavier" one. When $\beta = 0$ (walls with equal corrugation norms), particles focus to a trajectory equidistant from both wall and when $0 < |\beta| < 1$ the attractor is shifted towards the "flatter" wall.

Special case: channel with curved parallel walls. There is a special case when $J_h = 0$, that corresponds to a channel with parallel walls ($h(x) \equiv 0$, see Fig. 2.3, a on p. 34). In this case $J_{\phi h}$ is also equal to zero and there is no migration: $f(\eta) \equiv 0$. This is due to the simplified form of the flow model and to the asymptotic motion equations we use in this chapter. Indeed, in the LCL flow between parallel walls all streamlines are exactly parallel, so there are no preferential zones and no migration. However, Navier-Stokes simulations[5] showed that there is migration in parallel channels when the flow Reynolds number is not small (see also the work [24] by Fernandez de la Mora[6]). Indeed, taking into account proper inertia of the unperturbed flow breaks the symmetry between

---

[5]Performed by E. Candel during her Master's project in LAEGO.

[6]In Appendix A we revisit this work and confirm analytically the existence of the attractor for weakly-inertial particles in potential flow in parallel geometry.

fluid streamlines and creates a source of inertial particle migration. Large inertia of the particles can also lead to focusing in such a channel: for moderate τ the asymptotic motion equation (Eq. (3.4) on p. 62) becomes unstable and some particle focus to an attractor that is no longer close to fluid streamlines (see Section 3.5).

Another important effect that is not taken into account is particle migration due to the lift force. In fact, even in straight channels particles are known to migrate and focus to some equilibrium positions inside the channel. This happens as a result of the interaction of inertial particle wake with channel walls and the non-uniform main flow. The lift effect will be discussed in more details in Chapter 4.

3.3.4 Focusing/sedimentation regimes in presence of gravity: the trapping diagram

In presence of gravity the migration function defined by Eq. (3.13) can have different number of roots depending on γ_z (see Fig. 3.4).

The zones with different number of roots are separated by critical curves in the (β, γ_z) plane, that can be found from the following set of equations: $p(\eta; \beta, \gamma_z) = 0$, $p'_\eta(\eta; \beta, \gamma_z) = 0$, where $p(\eta; \beta, \gamma_z)$ is the structure polynomial defined by Eq. (3.14) and $p'_\eta = \partial p / \partial \eta$. These equations can be solved analytically:

$$
\begin{aligned}
\eta_{cr}(\beta) &= \frac{2\beta \pm \sqrt{5 + 4\beta^2}}{5}, \\
\gamma_z^{cr}(\beta) &= -(\eta_{cr}(\beta) + \beta)(\eta_{cr}(\beta)^2 - 1)^2.
\end{aligned}
\tag{3.18}
$$

The resulting curves separate the parameter plane (β, γ_z) into several zones. Combining zones with the same number and type of roots in $[-1; 1]$, we obtain the trapping diagram, that predicts particle behavior for any pair of β and γ_z. This diagram is plotted in Fig. 3.5. In zones I and III the migration function $f(\eta)$ has no roots in $\eta \in [-1; 1]$. In this case gravity dominates over inertial effects, and the direction of migration is the same all over the channel: heavy particles sink and light particles float up. In zone II the equation $f(\eta) = 0$ has two roots $\eta_\pm \in [-1, 1]$. The upper one $\eta_+(\beta, \gamma_z)$ attracts heavy
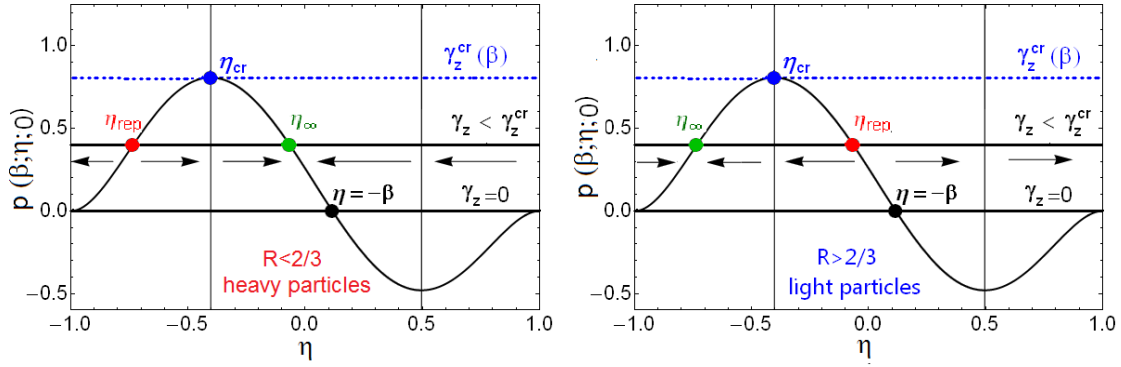
Figure 3.4: *Critical gravity number and focusing for heavy (left) and light (right) particles. Arrows indicate the direction of migration (see Eq. 3.13).*
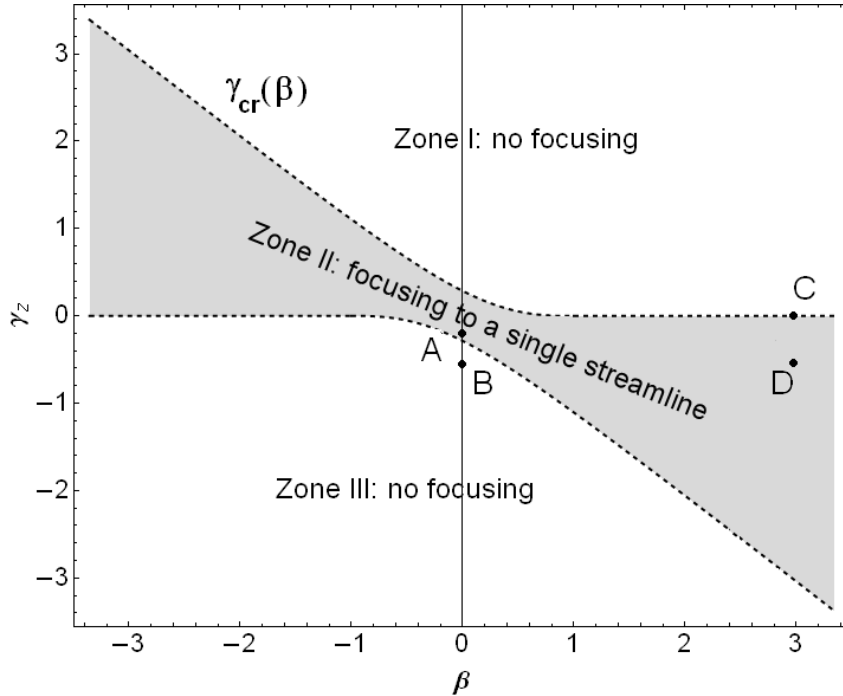
Figure 3.5: *The trapping diagram for a horizontally aligned channel. Here $\beta = -J_\phi/J_h$ is the corrugation asymmetry factor (difference between wall corrugation norms related to the aperture variation), $\gamma_z = G_z/J_h$ is the rescaled gravity number (the inverse Froude number related to aperture variation).*

particles and repels the light ones and the lower one $\eta_-(\beta, \gamma_z)$ attracts the light ones and repels the heavy (see Fig. 3.4).

Therefore, for any channel with small periodic corrugation ($\varepsilon \ll 1$) and any value of flow Froude number we can predict the focusing/sedimentation regime for weakly inertial

particles ($\tau \ll 1$). To do this we should calculate the J_h and $J_{\phi h}$ integrals for the channel, then find the values of β and γ_z using Eq. (3.11-3.16) and locate the resulting point on the tapping diagram in Fig. 3.5. Examples will be provided in Section 3.4 on p. 78.

3.3.5   Quantifying focusing and sedimentation

In this section we define and calculate (using the migration function $f(\eta)$) some important quantities that characterize particle focusing and sedimentation. For the sake of simplicity we consider only heavy particles ($R < 2/3$) and assume that gravity is directed downwards ($\gamma_z < 0$).

Focusing rate. The efficiency of focusing can be measured by the trapping rate of the attractor (defined by Eq. (3.9)):

$$\lambda = -f'(\eta_\infty) = -\tau \left(3R/2 - 1\right) \frac{3\varepsilon J_h}{4} \frac{p'_\eta(\eta_\infty; \beta, \gamma_z)}{(\eta_\infty^2 - 1)}, \tag{3.19}$$

where η_∞ is the position of the attractor (so that $f(\eta_\infty) = 0$). The trapping rate depends on the attractor position η_∞ and therefore (implicitly) on the gravity number γ_z.

One could expect that λ is maximal in the absence of gravity and decreases monotonously with γ_z, turning to zero at the critical point $\gamma_z = \gamma_z^{cr}$. However, this is not always true. Indeed, let us find the optimal trapping rate for a given β by solving the equation $\dfrac{d\lambda}{d\eta_\infty} = 0$:

$$\eta_\infty^{opt}(\beta) = -2\beta/5$$
$$\lambda_{max} = -\tau \left(3R/2 - 1\right) \frac{3\varepsilon J_h}{4} \left(1 + 4\beta^2/5\right)$$

Note that, when $\beta \neq 0$, this "optimal" attractor position does not coincide with attractor position at $\gamma_z = 0$ ($\eta_\infty^0 = -\beta$). This means that focusing is not necessarily optimal in the absence of gravity. For channels with $-5/2 < \beta < 0$ focusing can be enhanced by gravity and there is an optimal gravity number $\gamma_z^{opt} < 0$ (defined by the equation $p(\eta_\infty^{opt}(\beta), \beta, \gamma_z^{opt}) = 0$) at which the best trapping rate is achieved. However, this "optimal" attractor will not capture all the particles: some of them will be deposited on the walls because of the gravity.
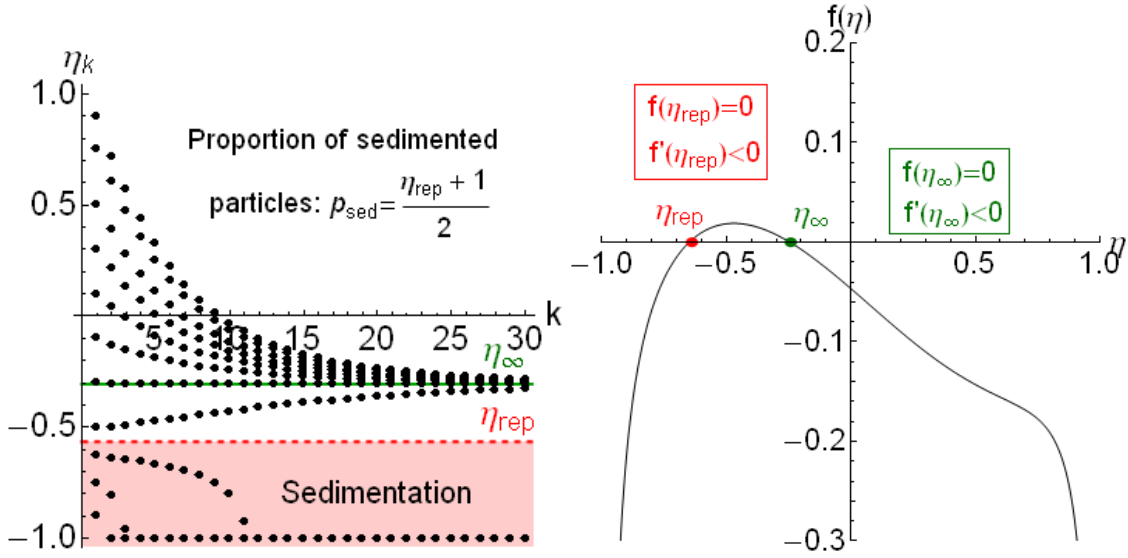
Figure 3.6: *Partial sedimentation regime ($G < G_{cr}$). Poincaré map of particle positions (left) and the migration function $f(\eta)$(right).*

Percentage of particles that avoid sedimentation. Another important property of the particle attractor is the size of its basin of attraction. Let us calculate the percentage of heavy particles that avoid sedimentation being trapped by the attractor. Following the direction of particle migration (defined by the sign of $f(\eta)$, see Fig. 3.6) we conclude that all heavy particles with initial positions $\eta_0 < \eta_{rep}$ are deposited on the lower wall and all the rest are trapped by the attractor η_∞. Therefore, the basin of attraction for heavy particles is $B_+(\gamma_z) = \{\eta_0 : \eta_0 > \eta_{rep}(\gamma_z)\}$ and we can calculate the percentage of trapped particles for a spatially uniform initial distribution:

$$P_{tr}(\gamma_z) = \frac{1}{N_P} \int\limits_{B_+(\gamma_z)} \rho_0(x, z)dxdz = (1 - \eta_{rep}(\gamma_z))/2, \qquad (3.20)$$

where $\rho_0(x, z) = N_P/\varepsilon$, N_P is the total number of particles and ε is the area of one channel period in non-dimensional variables.

The percentage of sedimented particle is, therefore:

$$P_{sed}(\gamma_z) = 1 - P_{tr}(\gamma_z) = (1 + \eta_{rep}(\gamma_z))/2. \qquad (3.21)$$

Note that that the percentage of trapped particles P_{tr} does not turn into zero at the
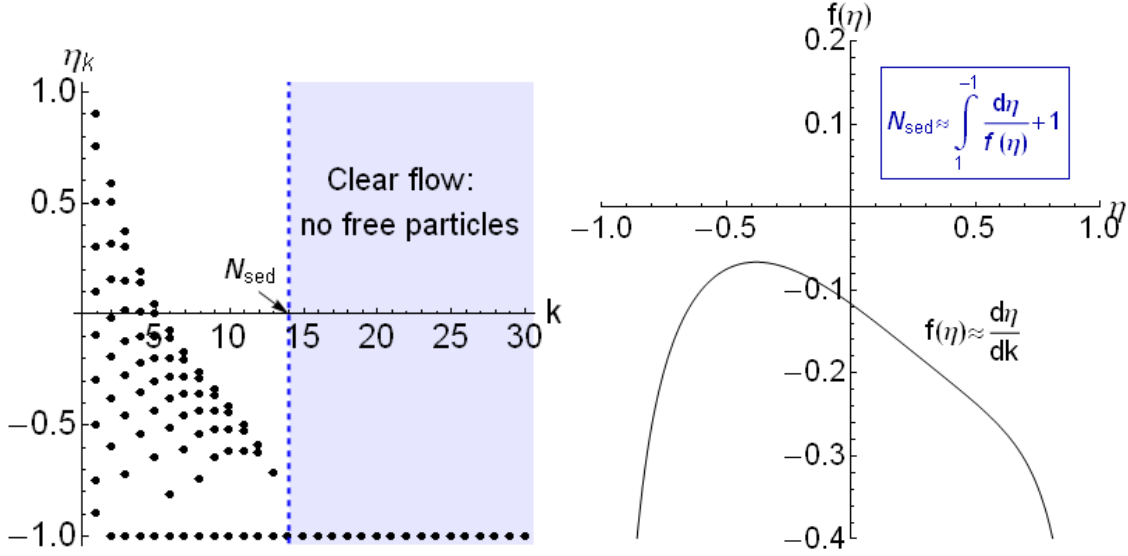
Figure 3.7: *Total sedimentation regime $(G > G_{cr})$. Poincaré map of particle positions (left) and the migration function $f(\eta)$(right).*

critical point $\gamma_z = \gamma_z^{cr}$. No matter how weak the attractor is, particles situated above the streamline $\eta = \eta_\infty$ can not cross it, because $f(\eta_\infty) = 0$. Therefore, whenever the attractor exists it traps no less than $(1 + \eta_{cr}(\beta))/2$ particles.

Maximal propagation length

When gravity is larger than critical $(\gamma_z > \gamma_z^{cr})$ all heavy particles end up on the lower wall sooner or later. The important parameter in this case is the propagation length: the distance a particle can go before deposition. This length can be estimated as the number of periods needed for a particle to migrate from its initial position η_0 to the bottom wall (using Eq. (3.10) with $\eta_1 = \eta_0$ and $\eta_2 = -1$):

$$N(\eta_0) = \int_{\eta_0}^{-1} \frac{d\eta}{f(\eta)}. \tag{3.22}$$

The *maximal deposition length* can be found by setting $\eta_0 = 1$ (this particle is the last to be deposited, see Fig. 3.7):

$$N_{sed} = N(1).$$

For $X > L_0 N_{sed}$ (in dimensional variables) the flow is clear - there is not a single particle in suspension (see Fig. 3.7).

Note, that in sub-critical regime ($\gamma_z < \gamma_z^{cr}$) the integrand in Eq. (3.22) contains a singularity at $\eta = \eta_\infty$ (because $f(\eta_\infty) = 0$). This means that for particles with $\eta_0 > \eta_{cr}$ the propagation length is infinite: these particles are trapped by the attractor and are never deposited.

The effect of focusing on particle resuspension. Now let us consider the resuspension of particles that were glued to the walls initially, but are set free at $t = 0$ (this can happen due to the sudden change of ionic forces, e.g. in case of saline injection). We do not take into account the hydrodynamical interaction of particles and the wall (wall-induced lift), so that the fate of such particle can be tracked easily: particles released at the bottom wall will stay where they are; particles released at the upper wall join the flow and can be trapped by the attractor or redeposited, depending on the flow rate.

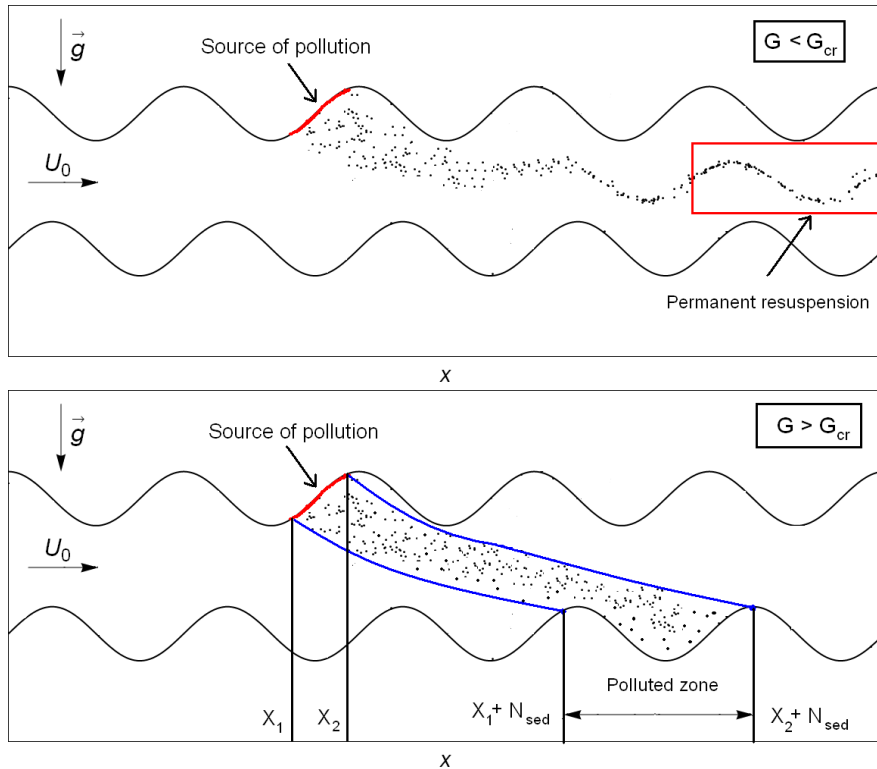
Figure 3.8: *Sketch of particle resuspension from a compact source at supercritical flow rates ($G < G_{cr}$, top) and subcritical flow rates ($G > G_{cr}$, bottom).*

Consider the situation when the flow is polluted by a dirty spot on the upper wall (particles released at $\eta = 1$ and $x \in [x_1; x_2]$). When $\gamma_z < \gamma_z^{cr}$, all these particles get

trapped by the attractor and can be found at any distance from the starting point: the whole flow is contaminated (see Fig. 3.8, top). When $\gamma_z > \gamma_z^{cr}$ all particles will be deposited at some distance from the source, polluting a finite length of the bottom wall (see Fig. 3.8, bottom).

The propagation length for the pollution can be found using the formula Eq. (3.22) for the maximal propagation length (translating the origin of the coordinate system from $x = 0$ to $x = x_1$). Depending on fracture geometry it can be either greater or smaller than for a non-corrugated channel. In particular, the propagation length is larger than in a straight channel when $\beta < 0$ (the upper wall is less corrugated than the lower one). Inversely, when $\beta > 0$ (the upper wall is more corrugated than the lower), the propagation length is smaller than in a straight channel[7].

3.4 Numerical verification of trapping diagrams and re-suspension regimes

In this section we verify the asymptotic results of Section 3.3, comparing them to the results of numerical simulations of particle motion. To simulate particle motion we make use of the second-order Maxey-Riley equations (see Eq. (3.3) on p. 61), neglecting the Basset term for the sake of simplicity. These equations are solved numerically using the 4th order Runge-Kutta method with adaptive time step (function NDSolve of Mathematica). The parameters used in all calculations are the following: particle response time $\tau = 0.01$, the density ratio is either $R = 2/7$ (particles are 3 times heavier that the fluid) or $R = 1$ (particles 2 times lighter than the fluid). The non-dimensional channel gap $\varepsilon = 0.5$ and the corrugation amplitude is fixed to $\delta_0 = 0.2$. Particles are injected at random positions inside the channel with no-slip initial conditions.

---

[7]This result can be obtained by expanding the $f(\eta)$ in Eq. (3.22) for small ε and calculating the cross-channel mean for the corrugation-induced term of the migration function.
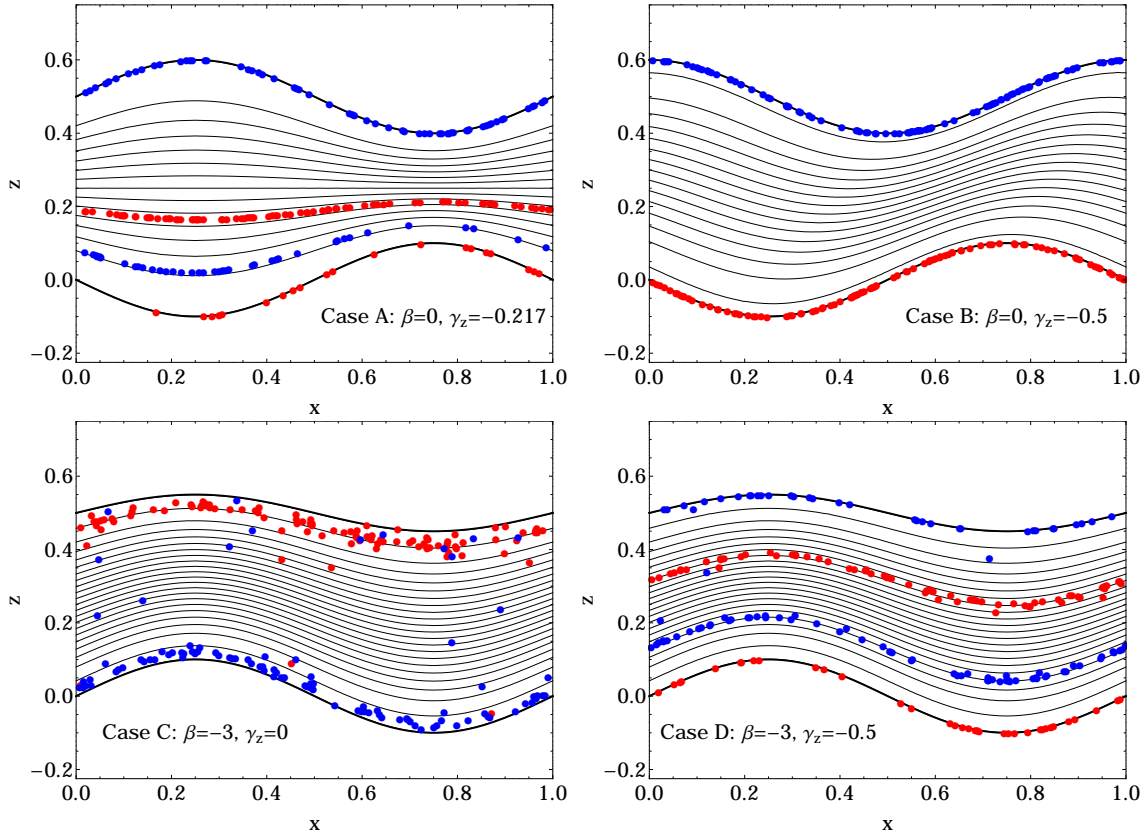
Figure 3.9: *Particle clouds at $t = 100$ illustrating different regimes for heavy ($R = 2/7$, red dots) and light ($R = 1$, blue dots) particles.*

3.4.1 Trapping diagram and particle clouds

We start by testing the predictive power of the trapping diagram constructed in the previous section. As a benchmark we use the standard test problem defined in Section 2.5: a channel with sinusoidal walls with varying phase shift α and corrugation asymmetry γ (see Eq. (2.5) on p. 33). This two-parameter family provides channels with any values of shape factors $J_h(\alpha, \gamma)$ and $J_{\phi h}(\alpha, \gamma)$. Varying the gravity number G_z we can, therefore, cover all possible values of $\beta = J_{\phi h}/J_h$ and $\gamma_z = \dfrac{8G_z}{9\varepsilon J_h}$. Four test cases have been considered, corresponding to points A, B, C and D on the trapping diagram (see Fig 3.5 on p. 72). The resulting particle clouds for $t = 100$ convective times are provided in Fig. 3.9. They show that particle attractors do exist when their existence is predicted by the diagram.
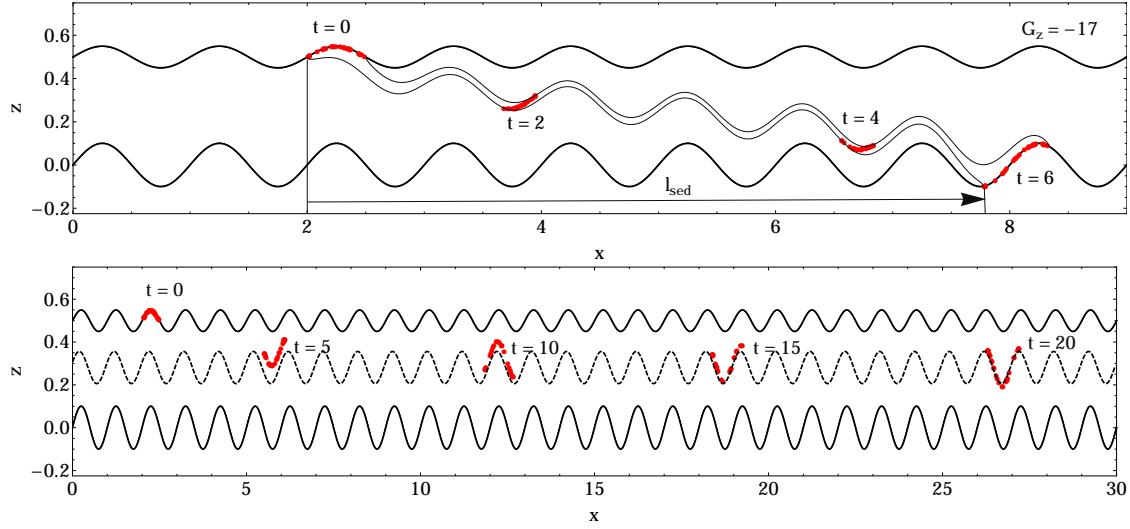
Figure 3.10: *Evolution a particle cloud resuspended from the upper wall for subcritical (top) and supercritical (bottom) flow rates. In subcritical case all particles are deposited at a finite distance that can be found from Eq. (3.22). Note that in the supercritical case the velocity of particle propagation is higher than the mean velocity of the fluid.*

3.4.2 Particle resuspension regimes

To illustrate particle resuspension we have chosen a channel with $\alpha = 0$ and unequal amplitudes of wall corrugation $\delta_1 = 2\delta_2$ (which corresponds to $\gamma = -1/3$). The average corrugation amplitude is set to $\delta_0 = 0.25$ and $\varepsilon = 0.5$. In this case the critical gravity number is equal to $G_z^{cr} \approx 0.65$.

We choose two gravity numbers for our simulation: (1) $G_z = 17 \gg G_z^{cr}$ and (2) $G_z = 0.45 < G_z^{cr}$. Our theory predicts that in the first case all particles will be deposited after $N_{sed} \approx 6$ periods (see Eq. (3.22)) and that in the second case particles will focus on the attracting streamline $\eta_{cr} = 0.112$ (see Eq. (3.13)). This is exactly what we observe in Fig. 3.10 that shows the evolution of resuspension cloud in time. Note also, that particle velocity on the attractor (averaged over one channel period) is larger than the mean velocity of the fluid : $\bar{v}_\tau^x \approx \bar{u}_f^x(\eta_\infty) > 1$. This can be seen very clearly in Fig. 3.10 (bottom), having in mind that the non-dimensional time $t = T/T_0$ is based on the mean velocity of the flow and corrugation length $T_0 = U_0/L_0$.

3.4.3 Channel with shifted sinusoidal walls: transport properties and their asymptotic estimates.

In this chapter we check the asymptotic estimates of particle transport properties in a channel with identical sinusoidal walls shifted in x-direction with phase shift α (which corresponds to Eq. (2.5) with $\gamma = 0$). In non-dimensional variables this corresponds to the following shape functions:

$$\phi(x) = 1/2 + \delta_0 \sin{(2\pi x)} \cos{(\alpha/2)}$$
$$h(x) = 1/2 + \delta_0 \cos{(2\pi x)} \sin{(\alpha/2)},$$

where $\delta_0 = A/H_0$ is the non-dimensional corrugation amplitude (equal for both walls). Phase shift α takes values from $[0; \pi]$, with $\alpha = 0$ corresponding to a channel with parallel walls and $\alpha = \pi$ to a mirror-symmetric channel. Note that the upper and the lower walls are exactly identical, so that $J_{\phi h} = ||\phi'_2||^2_h - ||\phi'_1||^2_h = 0$. Therefore, for any phase shift α the corrugation asymmetry factor is always zero: $\beta = 0$.

The theoretical trapping diagram (in natural variables α and $G = -G_z$) for $\delta_0 = 0.2$ is presented on Fig. 3.11 (top). This diagram has been obtained from Eq. (3.18) with $\beta = 0$ and Eq. (2.9) giving the dependence $J_h(\alpha)$ for the shifted channel. Using this diagram we choose four cases A', B', C' and D' to illustrate different focusing-sedimentation regimes. Particle clouds at $t = 100$ for each of these cases are shown in Fig. 3.12. As expected, in a channel with parallel walls (Fig. 3.12, Case A') particles stay dispersed all over the channel ($f(\eta) \equiv 0$ in this case). Shifting the walls with a finite phase shift (Fig. 3.12, Case B') makes all particles focus on the central line $\eta_\infty = 0$, as predicted by Eq. (3.7). In presence of gravity (Fig. 3.12, Case C') some of the particles converge to an attractor, while others are deposited onto the wall. For $G > G_{cr}$ theory predicts that all particles should be deposited: this is indeed observed in Fig. 3.12 (Case D').

To calculate the focusing rate $\lambda(G)$ given by Eq. (3.19) and the percentage of trapped particles $P_{tr}(G)$ given by Eq. (3.20) we find the roots $\eta_\pm(G, \alpha)$ of the function $f(\eta) = 0$ numerically on a grid G. For our set of parameters the $\lambda(G)$ curves are plotted on Fig. 3.11 (bottom) for different phase shifts α. Black dots indicate focusing rates, estimated
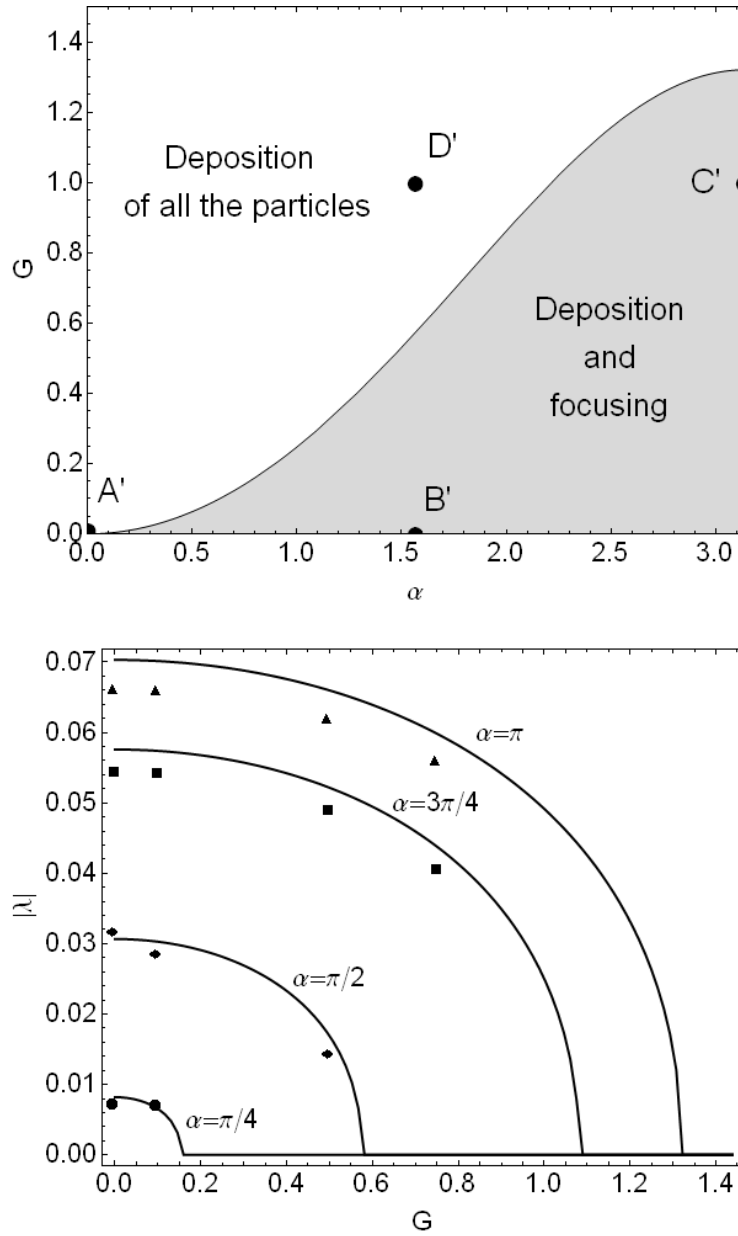
Figure 3.11: *Focusing/deposition diagram with cases A', B', C', D' located (top). Focusing rate λ as a function of phase shift $\alpha \in [0; \pi]$ at different gravity levels G (bottom). Curves are obtained using Eq. (3.19), points correspond to numerical simulations at $\tau = 10^{-3}$.*

from the numerical solution: for a single particle a distance to the attractor was measured at the end of each period and the limit

$$\tilde{\lambda} = \frac{1}{\tau(3R/2 - 1)} \lim_{k \to \infty} \ln \left(\frac{\eta_{k+1} - \eta_\infty}{\eta_k - \eta_\infty} \right)$$

Figure 3.12: *Particle clouds at* $t = 100$ *illustrating different focusing/sedimentation regimes in a channel with shifted walls (heavy particles:* $R = 2/7$*).*

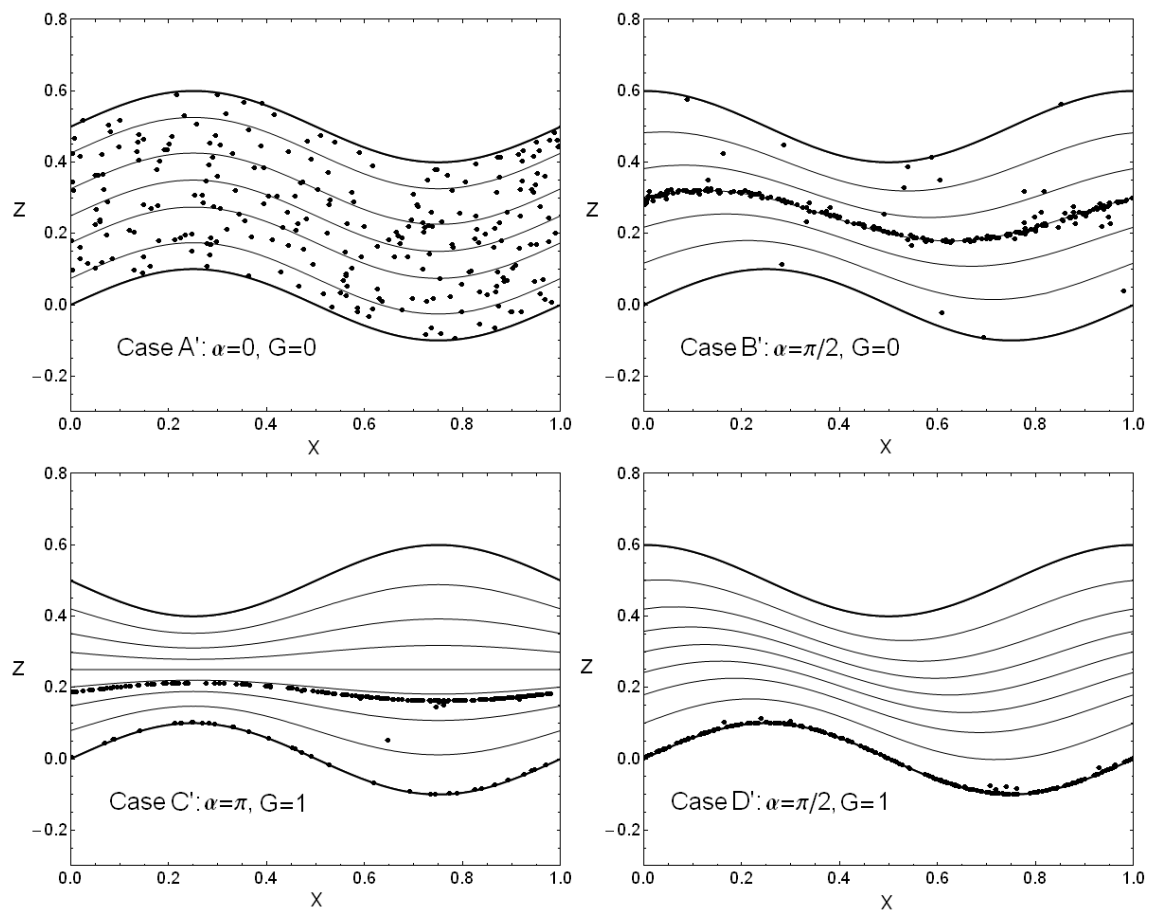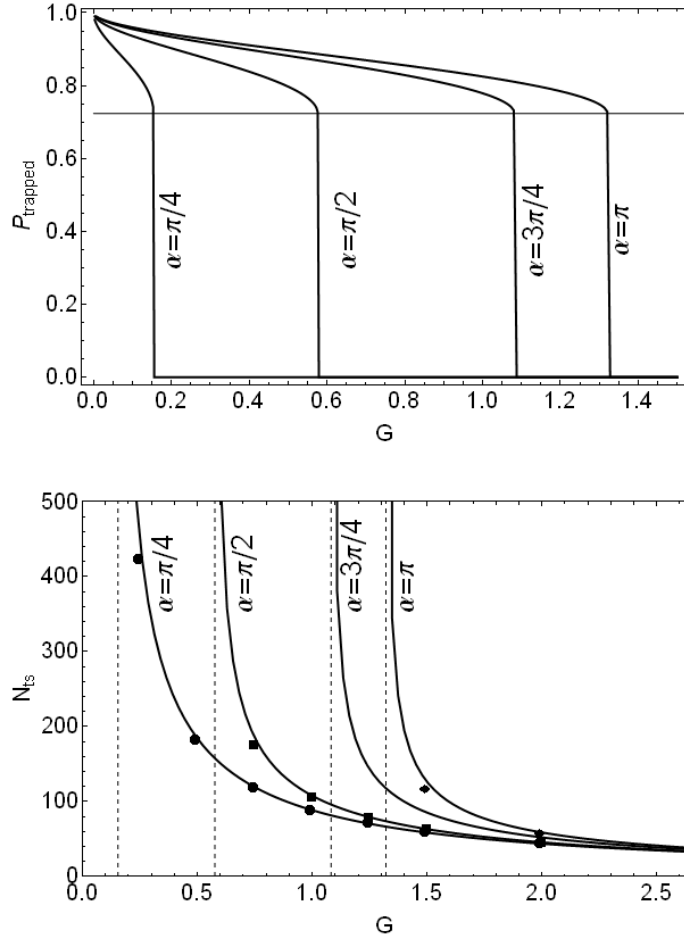Figure 3.13: *Percentage of particles trapped by the attractor (top) and maximal propagation length in periods (bottom) as function of gravity number G for various phase shifts α. Curves are obtained using Eq. (3.20) and Eq. (3.10) respectively, points on the lower plot correspond to numerical simulations at $\tau = 10^{-2}$.*

was estimated. A good correspondence could be obtained for $\tau = 10^{-3}$. The theory developed in this thesis can therefore predict accurately the trapping efficiency. As expected, for $\tau = 10^{-2}$ the difference between the theory and simulation was more important.

The percentage of particles trapped by the attractor depending on the gravity is plotted in Fig. 3.13 (top). At the critical $G = G_{cr}$ the percentage of trapped particles drops "abruptly" from its minimal value $(1 + 1/\sqrt{5})/2$ to zero, because the attractor ceases to exist at this point.

An estimate for the maximal propagation length (the maximal distance a particle can run before deposition) is given by Eq. (3.10). The integral from Eq. (3.10) was calculated

numerically on a fine grid of $G \in [G_{cr}(\alpha), 2G_{cr}(\pi)]$ for $\alpha = i\pi/4$, $\{i = 1..4\}$. Fig. 3.13 (bottom) shows the results of these calculations (solid lines) compared to numerical simulations (distance run by one particle released at the upper wall) for $\tau = 10^{-2}$ (black dots). One can see that the maximal propagation length depends on the gravity parameter G in a strongly non-linear way and diverges at $G = G_{cr}$. The effect phase shift on propagation length is important only when G is close to its critical value: for $G > 2G_{cr}(\pi)$ it can be safely neglected (all curves merge into one).

Comparison with numerical results showed that generally the asymptotic theory works quite well for small τ. If we increase the particle response time τ, theoretical predictions become less accurate, but the qualitative properties of particle dynamics do not change until we reach some critical value τ_{cr}, at which the slow manifold (Eq. (3.4)) becomes unstable. Particle behavior at larger τ will be discussed in the next section.

3.5   Particle behavior at finite response time: bifurcation of the attractor

In this section we assume $\tau = O(1)$ and consider a simplified form of Maxey-Riley equations, neglecting the gravity and all higher-order terms (leaving only the drag, the added mass and the pressure gradient term):

$$
\begin{aligned}
\frac{d\vec{x}_p}{dt} &= \vec{v}_p \\
\frac{d\vec{v}_p}{dt} &= -\frac{1}{\tau}(\vec{v}_p - \vec{u}_f) + \frac{3R}{2}\frac{D\vec{u}_f}{Dt},
\end{aligned}
\tag{3.23}
$$

so that for a given velocity field $\vec{u}_f$ everything is governed by two parameters: particle response time τ and density ratio R.

Let us calculate some particle trajectories for different channel geometries (mirror-symmetric, shifted and parallel) and see how their long-term behavior changes with τ (all other parameter are fixed: $R = 2/5$, $\delta_0 = 0.25$ and $\varepsilon = 0.1$ for shifted and mirror-symmetric channels). Initial velocities of the particles (that become important in this
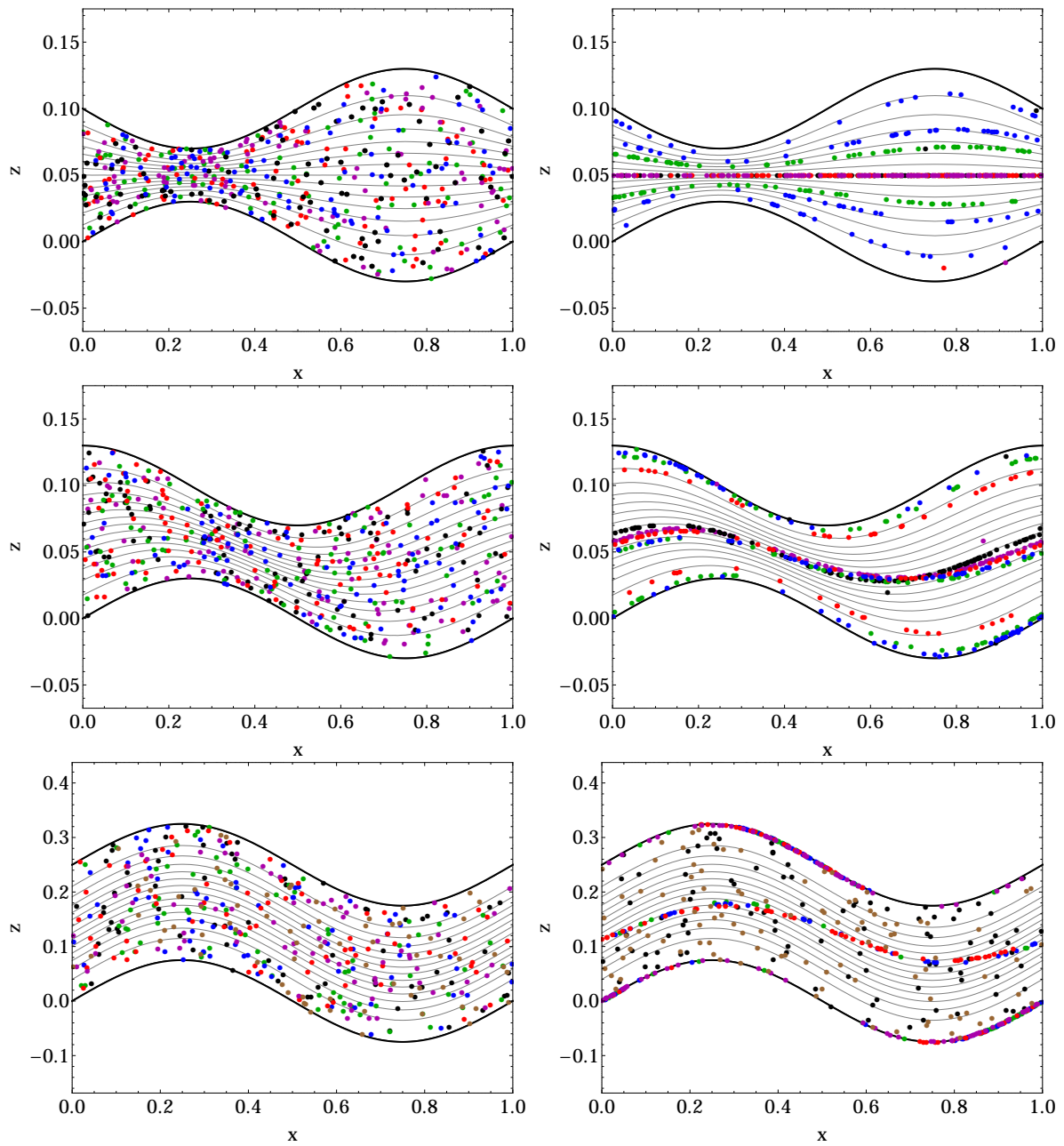
Figure 3.14: *A mixture of particles with different τ in a mirror-symmetric channel, a channel with shifted walls and a channel with parallel walls. There are different regimes of particle behavior depending on τ.*

regime) are taken equal to fluid velocity at their positions. The resulting clouds[8] at initial time (left) and at $t = 100$ (right) are shown in Fig. 3.5.
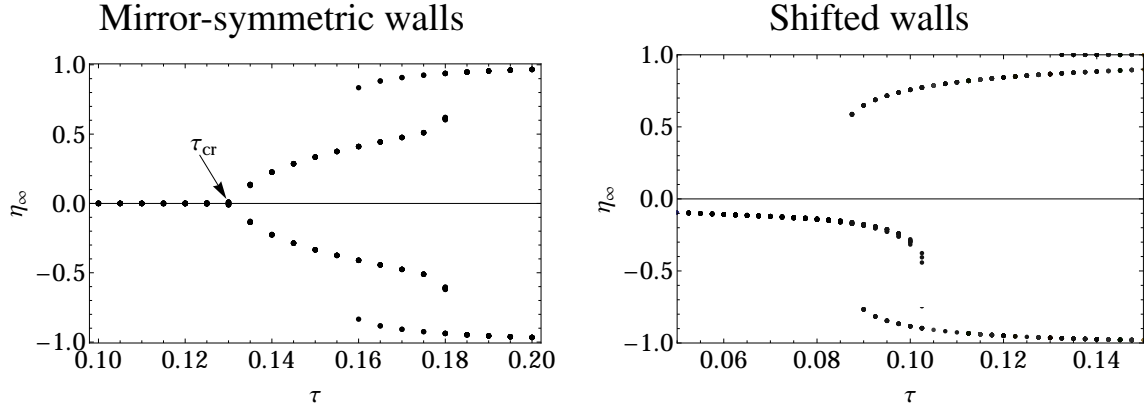

Figure 3.15: *Positions of particle attractors η_∞ depending on particle response time τ for a mirror symmetric channel (left) and a channel with shifted walls (right). This is not a period doubling diagram: each point corresponds to an attractor of unit spatial period.*

In a mirror-symmetric channel (Fig. 3.5, top) the asymptotic theory predicts focusing of particles to the axis of symmetry. This is what happens to particles with $\tau = 0.01; 0.1; 0.12$ (black, magenta and red particles in Fig. 3.5, top). At some critical response time $\tau_{cr} \approx 0.135$ this asymptotic attractor becomes unstable and particles focus on two (or even four) symmetrical attractors (see green ($\tau = 0.015$) and blue ($\tau = 0.017$) particles in Fig. 3.5, top). A similar effect is observed in a channel with shifted walls (Fig. 3.5, middle), where two additional attractors appear suddenly at finite distance from the asymptotic one.

Using the Poincaré section of particle cross-channel positions at the end of each period $\{\eta_k\}$, we can locate and plot all the existing attractors[9] $\eta_\infty = \lim_{k \to \infty} \eta_k$ depending on the particle response time τ. The resulting diagrams (obtained by numerical simulation of particle trajectories) are provided in Fig. 3.15. Note that this is not a period-doubling diagram: each point on this plot corresponds to an attractor with unit spatial period. Different attractors coexist at the same time and have separate basins of attraction.

We see that in a mirror-symmetric channel (Fig. 3.15, (left)) the asymptotic attractor

---

[8]Note that this is not a "dense cloud" of particles: particles do not interact in our model, they are just plotted together for convenience.

[9]Note that in this case attractors do not correspond to fluid streamlines $\eta = const.$ η_∞ is just a projection of some periodic trajectory on $x = k$.

$\eta_\infty = 0$ experiences a pitchfork bifurcation at $\tau_{cr} \approx 0.135$ and splits in two symmetrical branches. Each of these branches goes later through another bifurcation (apparently of subcritical type), that leads to the coexistence of four[10] particle attractors at the same time. In a channel with shifted walls (Fig. 3.15, (right)) the position of the asymptotic attractor depends smoothly on τ for $\tau < \tau_{cr}$, when it suddenly disappears, going through a bifurcation of subcritical type. Note that for $\tau > 0.13$ some of the particles get deposited on the upper wall ($\eta_{\text{inf}} = 1$).

Special case: channel with parallel walls. This effect leads also to particle focusing in a channel with curved parallel walls. As we remember, asymptotic theory predicted no focusing in such a channel. Indeed, particles with τ smaller than some critical value $\tau_{cr} \approx 0.115$ (black and brown in Fig. 3.5, bottom) remain dispersed over the channel even after many periods. However, particles with $\tau > \tau_{cr}$ (blue, green, magenta and red in Fig. 3.5, bottom) focus on a single trajectory, unless they hit a wall before.

3.6 Conclusion

The goal of this chapter was to study the focusing and sedimentation of weakly inertial particles (non-dimensional response time $\tau \ll 1$) in a flow through a channel with slow periodic corrugation (channel aspect ratio $\varepsilon \ll 1$) under the influence of gravity. Using the asymptotic expansion for particle velocity at small response times we have constructed the Poincaré map for particle positions at the end of each channel period and calculated explicitly the migration function $f(\eta)$, which fully determines particle migration across the channel at long times.

Asymptotic particle behavior depends on three non-dimensional parameters: the gravity number G (inverse of the Froude number) and two shape factors of the channel, $J_h = ||h'||_h^2$ (measuring the aperture variation) and $J_{\phi h} = ||\phi'_2||_h^2 - ||\phi'_1||_h^2$ (measuring the difference in corrugations of the upper and the lower walls)[11].

In the absence of gravity ($G = 0$) there are two types of particle behavior depending

---

[10]Probably, this "branching" process continues at larger τ, but we could not observe the resulting attractors because their basin of attractions are very small (most of the particles launched with no-slip initial conditions end up on the walls).

[11]The definition of the norm $||.||_h$ can be found on p. 33.

on channel geometry. In channels with $|J_{\phi h}| < J_h$ heavy particles focus to an attracting streamline at $\eta_\infty = -J_{\phi h}/J_h$ and light particles are repulsed from this streamline and go to the walls. In channels with $|J_{\phi h}| > J_h$ heavy particles go to the "less corrugated" wall[12] and light particles go in the opposite direction.

In presence of gravity ($G > 0$) two regimes of particle sedimentation are possible: for subcritical flow rates ($G > G_{cr}$) gravity dominates over the focusing effect and all particles are deposited onto the walls (heavy particles go to the lower wall, light particles go to the upper wall). For supercritical flow rates ($G < G_{cr}$) some particles (both light and heavy) can avoid deposition and travel long distances, trapped on the attracting streamline.

The main result of this chapter is the full trapping diagram that predicts all possible regimes of particle focusing and sedimentation depending on the rescaled gravity number $\gamma_z = \dfrac{8G_z}{9\varepsilon J_h}$ and the corrugation asymmetry factor $\beta = J_{\phi h}/J_h$ (see Eq. (3.18) and Fig. 3.5). Also, analytical estimates are found for the focusing rate of the attractor, the percentage of particles avoiding sedimentation (at supercritical flow rates) and the maximal propagation distance of the particle flow (at subcritical flow rates).

Numerical verification showed good agreement between asymptotic and simulation results for small response times ($\tau = 0.01$). Theoretical predictions become less accurate as we increase τ but the qualitative behavior does not change until we reach some critical value τ_{cr}, at which the slow manifold (Eq. (3.4)) becomes unstable. At this point the asymptotic attractor experiences a bifurcation, splitting into branches or disappearing. Typically, the new attractor branches are well separated in space from the asymptotic one, which implies some kind of hydrodynamic sorting between the particles with subcritical and supercritical values of τ. This critical behavior requires a special theoretical study. It has been left as a perspective to this thesis.

Note on experiments. Let us estimate some physical parameters at which focusing in a horizontal channel can be observed. For a channel with equal wall corrugations ($\beta = 0$) the critical rescaled gravity number is equal to $\gamma_z^{cr} = \dfrac{16}{25\sqrt{5}}$. Substituting this value into Eq. (3.16), recalling the definition of the inverse Froude number $G = \dfrac{L_0 g}{U_0^2}$ and expressing

---

[12]More precisely, the one with the smaller value of corrugation norm $||\phi_i||_h$.

the mean velocity in terms of Re_H, we get:

$$\frac{H_0^3 g}{\nu^2} < \frac{18 J_h (\varepsilon \mathrm{Re}_h)^2}{25\sqrt{5}}.$$

The LCL flow model used in this section is valid only for small $\varepsilon \mathrm{Re}_h$. More precisely, the global validity criterion (see Eq. (2.29) on p. 46 of Chapter 2) suggests that the LCL model (with a 10% tolerance) is valid up to $J_h(\varepsilon \mathrm{Re}_h)^2 \approx 80$. This gives the following estimate for the size of the channel:

$$H_0 < 25 \left(\frac{\nu^2}{g} \right)^{1/3}.$$

The final result depends on the viscosity of the carrier fluid. For example, in water focusing is theoretically possible only for very thin channels with $H_0 < 0.3mm$, in a 50%-mixture of water and glycerin for $H_0 < 1cm$ and in certain oils up to $H_0 \approx 10cm$.

Chapter 4

Influence of the lift force on particle migration

In the previous chapter we studied the behavior inertial particles governed by the Maxey-Riley motion equations. These equations neglect any inertial effects in the disturbance flow around the particle. Taking these inertial effects into account leads to the appearance of a new source of cross-stream particle migration: the inertial lift force. To study the joint effect of particle focusing due to both corrugation and lift-induced migration, we should incorporate the lift force into the particle motion equations. This can not be done easily, because the lift depends not only on local parameters, but also on the whole structure of the flow. However, when the flow Reynolds number is high and the particle is far from channel walls, the lift force can be approximated by a local formula and added as a new term to the Maxey-Riley equations. In this chapter we reconstruct the asymptotic equation and the Poincaré map taking into account this new term and show that in presence of gravity in the x-direction, lift-induced migration can be non-negligible. We also construct focusing diagrams for the LCL flow in a vertical channel (keeping in mind that their predictive power is limited by the quality of lift approximation).

4.1   Introduction

In the previous chapter we observed focusing of particles in a wavy channel under the influence of their proper inertia. This is not the only possible focusing mechanism in channel flows. Indeed, it is well-known now that particles do focus in narrow channels with straight walls, where particle inertia could never lead to migration (because all the streamlines are straight). Cross-stream particle migration was first observed by Poiseuille in 1836, who noticed that blood corpuscles in a pipe flow avoid near-wall zones. Later, similar behavior has been observed in various non-biological flows, both for buoyant and non buoyant particles. However, the first extensive and rigorous study of this effect came only in 1962, when Segré and Silberberg [59] carried out their famous experiment. They studied the motion of a rigid neutrally-buoyant sphere transported in a pipe of constant radius R and demonstrated that such spheres focus to a ring at a distance of about $r = 0.62R$ from the center of the pipe. This effect was called the "tubular pinch effect" and became a subject of vivid discussions for many years. The first theoretical explanation followed in 1965 with the famous work by Saffman [58]. Saffman supposed that lateral migration observed by Segré and Silberberg [59] could be driven by a lift force, resulting from inertial interaction of particle wake with the background shear flow. He considered a particle in slow relative motion through a simple shear flow and showed that particles moving faster than the fluid experience a lateral force, that pushes them to the slower zones of the flow. Inversely, particles lagging behind the fluid are pushed to faster zones. Saffman also supposed that neutrally buoyant particles would migrate to the center of the channel, because of the curvature of the velocity profile. Saffman's theory did not explain the Segré-Silberberg experiment completely, because it did not take into account the influence of the walls. Later, lift-induced particle migration in Poiseuille flow has been studied in a wide range of flow Reynolds numbers. The case $\mathrm{Re}_H \ll 1$ has been considered by Vasseur & Cox [68] and Ho & Leal [32], for $\mathrm{Re}_H = O(1)$ see Hogg [33] and Schonberg & Hinch [60], and for $\mathrm{Re}_H \gg 1$ see Asmolov [3].

The goal of this chapter is to estimate the influence of the lift on particle focusing in a corrugated channel. For a channel with corrugated walls we should expect a combined

effect of focusing due to proper inertia of the particles and lift-induced focusing due to inertia of the disturbed flow. The most interesting case is the vertical channel with fluid flowing downward: in this case heavy particles will lead the flow and the lift force will push them to the walls - in contrast with centrifugal forces that make them converge to a preferential streamline inside the channel (as shown in Chapter 3). To find the conditions for particle focusing we have to incorporate the lift force into the particle motion equations.

It is difficult to incorporate the lift force into the particle motion equations, because it depends not only on local parameters, but also on the whole structure of the flow. This is why there is no generally used equation for the lift: it has to be calculated *ad hoc* for each specific flow configuration (e.g. shear flow over a wall, Poiseuille flow, rotational flow). Moreover, it is not always possible to represent fluid inertia effects as an additive force in the particle motion equation (Candelier and Angilella [11]).

However, when the unperturbed flow is close to unidirectional (as in the present work, because $\varepsilon \ll 1$) and cross-stream migration is slow (and it is, because $\tau \ll 1$) the flow around the particle can be considered as stationary and the lift force depends only on current particle position and slip velocity. Moreover, for very small $\varepsilon \ll 1$ the lift force in the LCL flow can be approximated by the well-known results for the Poiseuille flow between plane parallel walls.

The simplest situation is when the flow Reynolds number is high. In this case it is possible to "forget" about the part of the flow at some distance from the particle (the typical length scale being $l_f = H_0/\sqrt{\mathrm{Re}_H}$) and to approximate the flow at this scale by simple shear or parabolic flow. For a Poiseuille flow between the plane walls Asmolov showed [3] that far from both walls (the distance from the wall $d > H_0/\sqrt{\mathrm{Re}_H}$) the lift force acting on a particle is indeed close to that for a particle moving in unbounded parabolic flow. The lift force in this case depends on two local parameters, characterizing the flow at particle position. If the particle is far enough both from the walls and from the center of the channel, the curvature of the velocity profile can be neglected too and one can use Saffman's formula for the simple shear flow. Close to a wall ($d \ll H_0/\sqrt{\mathrm{Re}_H}$) the lift can be found by approximating the flow with a wall-bounded shear flow.

Therefore, in this chapter we assume that the flow Reynolds number Re_H is high and exclude the near-wall zones from consideration, justifying the use of a linear additive lift force. The high Reynolds numbers requirement seems to be in contradiction with the assumptions made in previous chapters. However, if the channel aspect ratio ε is small (very slow corrugation), the parameter $\varepsilon \mathrm{Re}_H$ can remain small even for sufficiently high Re_H.

Outline of the chapter

In Section 4.2 we provide the classical results for the lift acting on a particle in unidirectional unbounded flows: the simple shear flow (Saffman's formula) and the unbounded parabolic flow (Asmolov's formula). This formulas for the lift can be used when the flow is close to unidirectional, cross-stream particle migration is slow and particle is far from the walls ($d > H_0/\sqrt{\mathrm{Re}_H}$). In this case the lift depends only on local properties of the flow and can be included in the Maxey-Riley equations in the form of an additive force. We start by using the Saffman's formula for the lift, based on the local value of the shear rate. In Section 4.3 we calculate the Poincaré map of particle motion and obtain the trapping diagrams for a vertical channel. These diagrams are verified numerically on a few test problems. In Section 4.5 we consider Asmolov's approximation for the lift, that takes into account the parabolicity of the velocity profile. In this case no analytical expression for the migration function is available, but the Poincaré map can be calculated numerically for any given geometry. Comparing the migration functions with Saffman's and Asmolov's lift approximations we see that for small τ the difference between them is small, which justifies the results of Section 4.3 (under condition that particles are far from the walls).

4.2   Saffman's approximation for the lift force

Consider a simple shear flow $\vec{U}(\vec{X}) = (U_f(Z), 0)$ and a particle moving parallel to the fluid with the velocity V_p. In the coordinate system translating with the particle (X', Z')

the undisturbed flow takes the following form:

$$U_f'(Z') = -V_s + K \cdot Z',$$

where $V_s = V_p - U_f(Z_p)$ is the particle slip velocity, $K = \dfrac{dU_f}{dZ}$ is the shear rate of the flow. Here $X' = X - X_p(t)$, $Z' = Z - Z_p(t)$, where $\dot{X}_p(t) = V_p$ and $Z_p(t) \equiv const$, because particle velocity is parallel to the flow. This flow is defined by two non-dimensional numbers: the Reynolds number based on particle slip velocity $\mathrm{Re}_s = \dfrac{V_s a}{\nu}$ and the Reynolds number based on the shear rate $\mathrm{Re}_K = \dfrac{|K|a^2}{\nu}$.

Under these conditions, the Navier-Stokes equations for the disturbance flow around the particle can be solved using the method of matched asymptotic expansions, which is based on separating the flow around the particle into the inner zone where viscous forces dominate and the outer zone where particle can be represented as a point force perturbation. This approach has been used by Saffman in [58], who obtained the following formula for the lift force in a simple shear flow (in dimensional variables)[1]:

$$\vec{F}_L^{saff} = -C_L^0 a^2 (\mu \rho_f)^{1/2} K^{1/2} \mathrm{sgn}(K) V_s \vec{e}_z,$$

where $C_L^0 = 6.46$ is the lift coefficient.

Now let us follow a weakly-inertial particle, moving in the vicinity of a streamline $\eta = \eta_0$ in the LCL flow at moderate Reynolds numbers Re_H (but small $\varepsilon \mathrm{Re}_H$). As discussed in the previous section, a particle does not "see" the flow at distances sufficiently larger than some typical length $l_f \sim H_0/\sqrt{\mathrm{Re}_H}$. Therefore, if the particle is far both from the walls and from the center of the channel, we can approximate the flow around it by a unidirectional shear flow in Frenet coordinate frame $(\vec{s}(\vec{X}_p), \vec{n}(\vec{X}_p))$ attached to the streamline. In this coordinate system the unperturbed flow around the particle can be approximated by linear shear and consider the tangential component of particle slip velocity (which is much larger than the normal one if $\varepsilon \ll 1$). The Saffman's formula for

---

[1]This formula was derived under assumption that $\mathrm{Re}_s \ll \sqrt{\mathrm{Re}_K}$. Later, McLaughlin [45] (and independantly Asmolov [2]) extended this result to arbitraty $\alpha = \mathrm{Re}_s/\sqrt{\mathrm{Re}_K}$, introducing the modified lift coefficient C_L as a function of α.
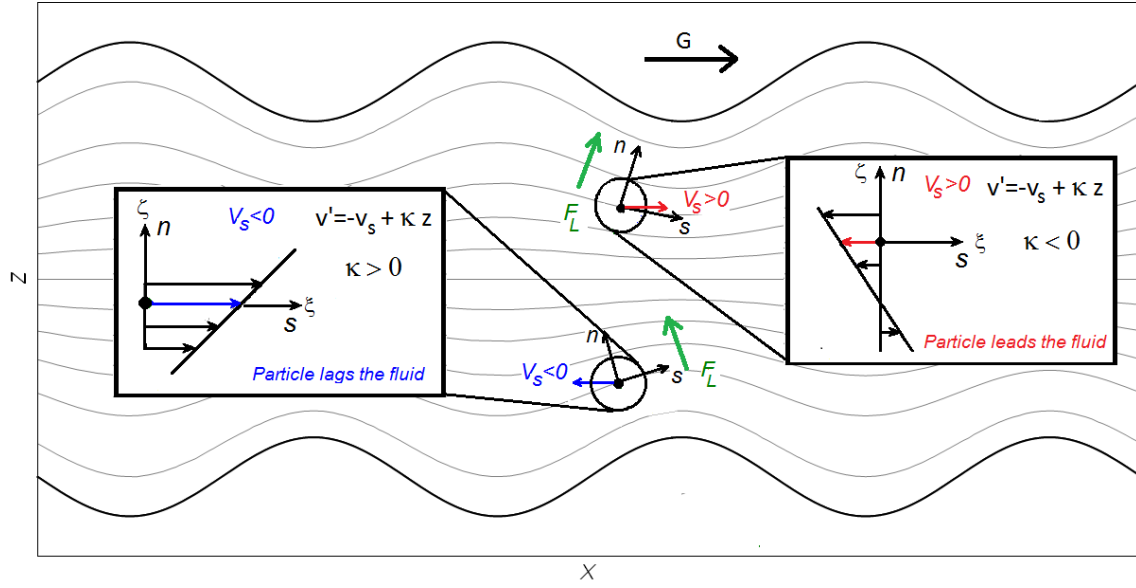
Figure 4.1: Saffman's lift acting on particles lagging or leading the fluid. "Slow" particles are pushed to the center, "fast" particles are pushed to the walls.

the lift in this case reads:

$$\vec{F}_L = -C_L^0 a^2 (\mu \rho_f)^{1/2} K^{1/2} \mathrm{sgn}(K) \left(\vec{V}_s \cdot \vec{s} \right) \vec{n},$$

where the local shear in the LCL flow can be rewritten as:

$$K = \frac{\partial(\vec{U}_f \cdot \vec{s})}{\partial n} \approx -\frac{U_0}{H_0} \left(\frac{8}{3h(x)} \eta_p + O(\varepsilon^2) \right),$$

where $\eta_p = \eta(\vec{X}_p / L_0)$ is the cross-section coordinate of the particle (see Chapter 2).

4.3   Particle focusing in a vertical LCL flow

4.3.1   Maxey-Riley equations with lift

To model particle motion we use the Maxey-Riley equations adding Saffman's lift as a new term. We neglect Faxen corrections here, assuming that they are small compared to the gravity force directed along the flow. Particle motion equations then take the following

form:

$$\frac{d\vec{v}_p}{dt} = -\frac{1}{\tau}\vec{v}_s + \left(1 - \frac{3R}{2}\right)\vec{G} + \frac{3R}{2}((\vec{u}_f\nabla)\vec{u}_f) - \frac{3C_L\sqrt{R}}{\sqrt{2}\sqrt{\tau}}\sqrt{|\kappa|}\text{sgn}(\kappa)(\vec{v}_s \cdot \vec{s}(\vec{x}_p))\vec{n}(\vec{x}_p),$$

(4.1)

where $\kappa = -\frac{8\eta_p}{3h(x)} + O(\varepsilon^2)$ is the local shear rate at particle position $\eta_p = \eta(x_p, z_p)$,

$\vec{s} = \frac{\vec{u}_f}{|u_f|}$ is the tangent vector to fluid streamlines at point $\vec{x}_p$, and $\vec{n}$ is the direct normal vector respectively.

The asymptotic equation then takes the following form:

$$\begin{aligned}\dot{\vec{x}}_p &= \vec{v}_\tau, \\ \vec{v}_\tau &= \vec{u}_f + \tau\vec{v}_1 + \tau^{3/2}\vec{v}_{3/2},\end{aligned}$$

(4.2)

where

$$\vec{v}_1 = \left(\frac{3R}{2} - 1\right)\left((\vec{u}_f\nabla)\vec{u}_f - \vec{G}\right),$$

$$\vec{v}_{3/2} = \frac{3\sqrt{R}}{\sqrt{2}}C_L(\vec{v}_1, \vec{x}_p)\sqrt{\kappa}\text{sgn}(\kappa)(\vec{v}_1 \cdot \vec{s}(\vec{x}_p))\,\vec{n}(\vec{x}_p).$$

In the following section we use this asymptotic equation to calculate the Poincaré map of particle motion in the LCL flow, using Saffman's approximation for the lift ($C_L = 6.46$).

4.3.2 Poincaré map in the LCL flow with lift

To calculate the migration function $f(\eta)$ we use the expansion (4.2):

$$\eta_{k+1} - \eta_k = f(\eta_k) \approx \frac{\varepsilon}{\psi'(\eta_k)}\left(\tau I_0(\eta) + \tau^{3/2}I_{3/2}(\eta)\right)ds + O(\tau^2),$$

where $I_0 = \int\limits_{S_0}(\vec{v}_1 \cdot \vec{n})ds$ and $I_{3/2} = \int\limits_{S_0}(\vec{v}_{3/2} \cdot \vec{n})ds$. For the LCL flow and Saffman's lift these integrals can be calculated explicitly:

$$\begin{aligned}I_0(\eta) &= \left(\frac{3R}{2} - 1\right)(P(\eta) + G_z), \\ I_{3/2}(\eta) &= \frac{3C_L^0}{\sqrt{2}}\sqrt{\varepsilon R}\left(\frac{3R}{2} - 1\right)(G_xL_G(\eta) + L_I(\eta)),\end{aligned}$$

(4.3)

where P, L_G, L_I represent different sources of cross-stream migration. These sources are listed below:

Corrugation induced particle migration:

$$P(\eta) = \frac{9\varepsilon}{4}(\eta^2 - 1)^2(\eta J_h + J_\phi),$$
$$J_h = \int\limits_0^1 \frac{(h')^2}{h^3}dx, \;\; J_{h\phi} = \int\limits_0^1 \frac{\phi' h'}{h^3}dx. \tag{4.4}$$

This term is responsible for particle migration because of the focusing effect, that has been studied in Chapter 3.

Lift-induced migration due to buoyancy:

$$L_G(\eta) = -\frac{2\sqrt{2}}{\sqrt{3}}\overline{h^{-1}}\sqrt{|\eta|}\mathrm{sgn}(\eta) + O(\varepsilon),$$
$$\overline{h^{-1}} = \int\limits_0^1 \frac{1}{h(x)}dx. \tag{4.5}$$

This is migration due to the lift force acting on particles that lead or lag the fluid because of the gravity. It can be directed to the center of the channel or to the walls (depending on the direction of gravity).

Lift-induced migration due to acceleration and deceleration of particles:

$$L_I(\eta) = -\frac{27\varepsilon}{32}(J_a\eta^2 + J_b\eta + J_c)(\eta^2 - 1)^2\sqrt{|\eta|}\mathrm{sgn}(\eta),$$
$$J_a = \int_0^1 \frac{(h'(x))^3}{h^4(x)}dx, \;\; J_b = \int_0^1 \frac{2(h'(x))^2\phi'(x)}{h^4(x)}dx, \;\; J_c = \int_0^1 \frac{h'(x)(\phi'(x))^2}{h^4(x)}dx. \tag{4.6}$$

Fluid in the corrugated channel is repeatedly accelerated and decelerated, mostly because of the aperture variations. Inertial particles react to these changes of fluid velocity with a delay, which makes them lead or lag the fluid in different zones of the channel. This lead (or lag) produces a lift force than can create migration, which is represented by this term.

To estimate these terms by the order of magnitude we take into account the fact that $\phi_{1,2}(x) = O(1)$ and $\phi'_{1,2}(x) = O(\delta)$, where δ is the typical corrugation amplitude. This yields: $P(\eta) = O(\varepsilon\delta)$, $L_G(\eta) = O(G_x)$, $L_I(\eta) = O(\varepsilon\delta^3)$ and therefore

$$f(\eta) = \frac{\tau\varepsilon}{\Psi'(\eta_k)}\left(\frac{3R}{2} - 1\right)\left(O(G_z) + O(G_x\sqrt{\tau\varepsilon R}) + O(\varepsilon\delta) + O(\varepsilon\delta^3\sqrt{\tau R})\right).$$

We can see that the last term, corresponding to $L_I(\eta)$, is always negligible for small St and/or δ (contribution of the lift force due to inertial lag is unimportant in the asymptotic regime). We will ignore this term in the following sections.

Therefore, in a horizontal channel the lift force can be neglected in the core flow (we exclude the near-wall zones here), because the only source of tangential slip velocity is the inertial lag, and lift-induced migration due to this inertial lag is always small. In presence of gravity in the x-direction the lift force can be non-negligible and can compete with centrifugal forces induced by wall corrugation. For simplicity we consider only vertically-aligned channels ($G_z = 0$, $G_x = O(\delta\sqrt{\text{St}})$), assuming that channel walls are not parallel. Using the focusing conditions in Eq. (3.7) we will find the range of gravity numbers G_x in which particle focusing is possible, depending on channel geometry.

4.3.3 Trapping diagrams for the vertical LCL flow with lift

For a vertically aligned channel ($G_z = 0$) the migration function can be calculated approximately:

$$f(\eta) \approx \tau \left(\frac{3R}{2} - 1 \right) \frac{9\varepsilon^2 J_h}{16\tilde{\psi}'(\eta)} q(\eta; \beta, \gamma_x) + O(\tau\varepsilon^2) + O\left(\delta^3(\tau\varepsilon)^{3/2} \right)$$

and $q(\eta; \beta, \gamma_z) = (\eta+\beta)(\eta^2-1)^2 - \gamma_x\sqrt{|\eta|}\text{sgn}(\eta)$, where $\gamma_x = \dfrac{8\sqrt{3}G_x}{3\varepsilon^2 J_h}C_L\sqrt{\tau R}$ and $\beta = (\|\phi_2'\|_h^2 - \|\phi_1'\|_h^2)/\|h'\|_h^2$ is the corrugation asymmetry parameter (difference between wall corrugations related to aperture variations, introduced in Chapter 2). The corrugation-induced and lift-induced migration have opposite directions: corrugations make heavy particles focus in the center of the channel and lift forces make them migrate towards the walls. Using the same procedure as in the previous chapter we construct a trapping diagram in $\beta - \gamma_x$ axes, by solving the equations $q(\eta; \beta, \gamma_x) = 0$, $q_\eta'(\eta; \beta, \gamma_x) = 0$ numerically on a grid of β. The resulting trapping diagrams for light and heavy particles are shown in Fig. 4.2.

Four different regimes are possible. When gravity is directed against the flow (Zone I) lift force works in the same direction as the inertial forces: heavy particles go to a single attractor and light particles migrate to the walls (see Fig. 4.3, A'). When gravity is co-
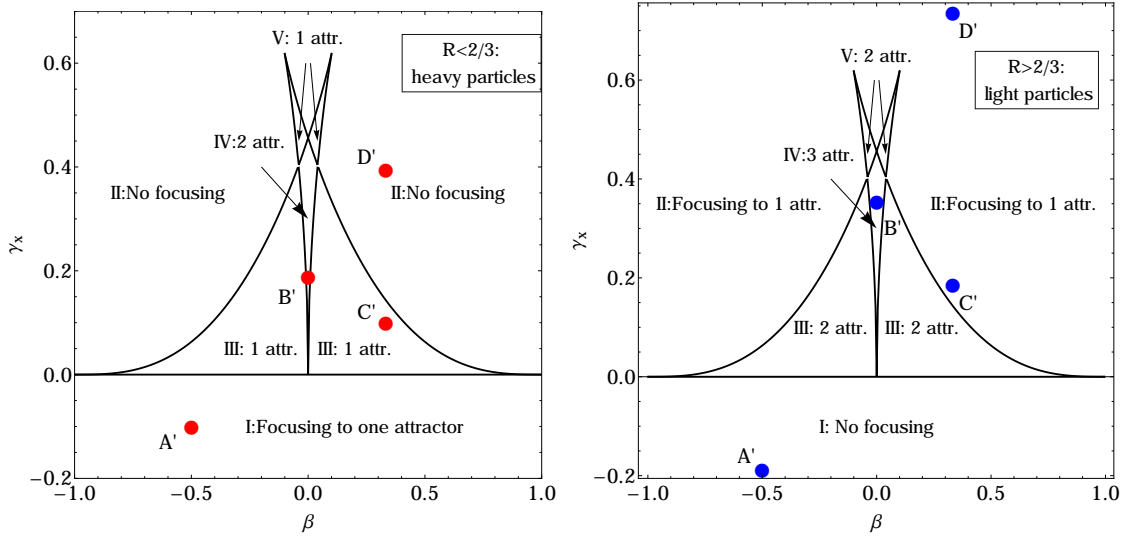
Figure 4.2: *Trapping diagrams for a vertically aligned channel:* γ_x *is the rescaled gravity, and* β *is the corrugation asymmetry factor.*

directed with the flow (Zone II) and is large enough to override the effect of corrugation, heavy particles always lag the flow and therefore go to the walls; light particles are focused to the central line (see Fig. 4.3, D'). For small β and moderate γ_x (Zone IV) the lift force works against focusing and is balanced at some distance from the center. This makes the attractor for heavy particles split into two branches (see Fig. 4.3, B'). For light particles there is always an attractor in the center, and in Zone IV two additional ones appear at some distance from the walls (see Fig. 4.3, B'). As we increase the gravity number γ_x the attractors disappear one after another (through Zone V to Zone II). The same happens if we increase the corrugation asymmetry factor β while keeping γ_x constant (through Zone III to Zone II, see Fig. 4.3, C').

To verify this trapping diagram, the Maxey-Riley equations with lift (Eq. (4.1)) have been solved numerically for $\tau = 0.01$, $\delta = 0.2$, $\varepsilon = 0.5$ and different geometries and gravity numbers. The test cases are shown on the trapping diagram in Fig. 4.2 and the resulting particle clouds are provided in Fig. 4.3. Unlike the horizontal case, the positions of particle attractors and their critical gravity numbers depend on the size and density of the particle (because γ_x depends on τ and R). This is why the cases A', B', C', D' for heavy and light particles do not coincide on the diagram.
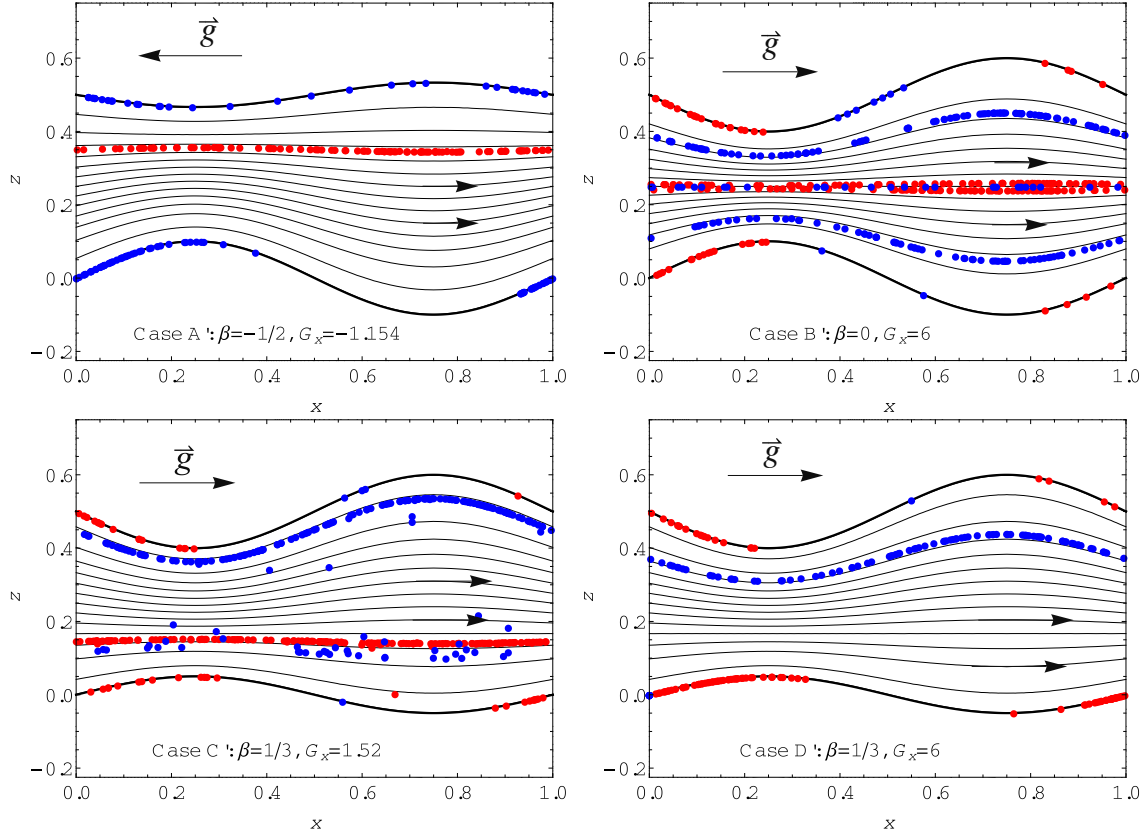
Figure 4.3: *Particle clouds at $t = 200$ illustrating different focusing regimes. Red particles are heavier than the fluid ($R = 2/7$), blue particles are lighter than the fluid ($R = 1$). Cases A', B', C' and D' correspond to points on the trapping diagrams Fig. 4.2.*

4.4 Particles with finite response times: lift-induced chaos

In the previous sections we neglected the lift force due to particle lead and lag caused by inertia and corrugations (the $L_I(\eta)$ term in the Poincaré map). This was justified in presence of gravity, because this term is much smaller than the gravity-induced lift. In the absence of gravity this term would modify the attractor positions only slightly. However, for finite response times τ it can lead to completely different behavior.

In this section we consider the mirror-symmetric channel and the Maxey-Riley equations with lift and without gravity:

$$\frac{d\vec{x}_p}{dt} = \vec{v}_p$$
$$\frac{d\vec{v}_p}{dt} = -\frac{1}{\tau}(\vec{v}_p - \vec{u}_f) + \frac{3R}{2}\frac{D\vec{u}_f}{Dt} - \vec{F}_L(\vec{x}_p, \vec{v}_p) \tag{4.7}$$

where $\vec{F}_L = \dfrac{2C_L\sqrt{R}}{\sqrt{3}\sqrt{\tau}}|\eta(\vec{x}_p)/h(x)|^{1/2}\mathrm{sgn}(\eta)(\vec{v}_p - \vec{u}_f) \cdot \vec{s}(\vec{x}_p))\vec{n}(\vec{x}_p)$ is Saffman's lift force defined earlier.

Numerical results for this model are provided in Fig. 4.4, which shows the Poincaré sections (at the end of each corrugation period) for several particles released at different initial positions η_0 at the inlet of the channel. They give an idea of typical particle behavior at different τ. At small τ the asymptotic theory predicts two attractors at some small distance from the center of the channel[2]. The two branches of the asymptotic attractor are clearly visible at $\tau = 0.001$ (Fig. 4.4, top). As we increase τ, these attractors experience a series of period-doubling bifurcations, finally leading to chaos.

The corresponding bifurcation diagram is provided in Fig. 4.5. Calculation of branching parameters for this diagram shows that they are close to Feigenbaum constants[3] :

$$\frac{\Delta\tau_1}{\Delta\tau_2} = 4.33, \quad \frac{\Delta\eta_1^\infty}{\Delta\eta_2^\infty} = 2.589$$

and confirms that this is indeed the classical period-doubling cascade.

Note that a similar behavior has been observed by Domesi and Kuhlman [19] (see Fig. 4.6) for inertial particles in a periodic stationary cellular flow, given by the streamfunction $\psi(x, y) = A\sin(x)\cos(y)$. Particles are governed by the simplified Maxey-Riley equations with gravity in the x direction (and without lift). Despite the difference in flow and particle motion models, the mechanism is not very different: a particle moving close to the axis of symmetry experiences a spatially periodic force, of which x- and y-components change sign in coordination and make the particle cross the axis many times (due to inertia). In the cellular flow both components of this periodic force are due to drag. In our case there is no cross-channel component of fluid velocity, but it is the lift force that plays a similar role.

---

[2]They can be found by equilibrating the focusing migration function $P(\eta)$ (see Eq. (4.4)) and the lift-induced migration due to corrugations $L_I(\eta)$ (see Eq. (4.6)) (this term has been neglected in Chapter 4 due to the presence of gravity).

[3]Feigenbaum constants [23] are $\displaystyle\lim_{i\to\infty}\frac{\Delta\tau_i}{\Delta\tau_{i+1}} = 4.669...$ and $\displaystyle\lim_{i\to\infty}\frac{\Delta\eta_i^\infty}{\Delta\eta_{i+1}^\infty} = 2.509...$
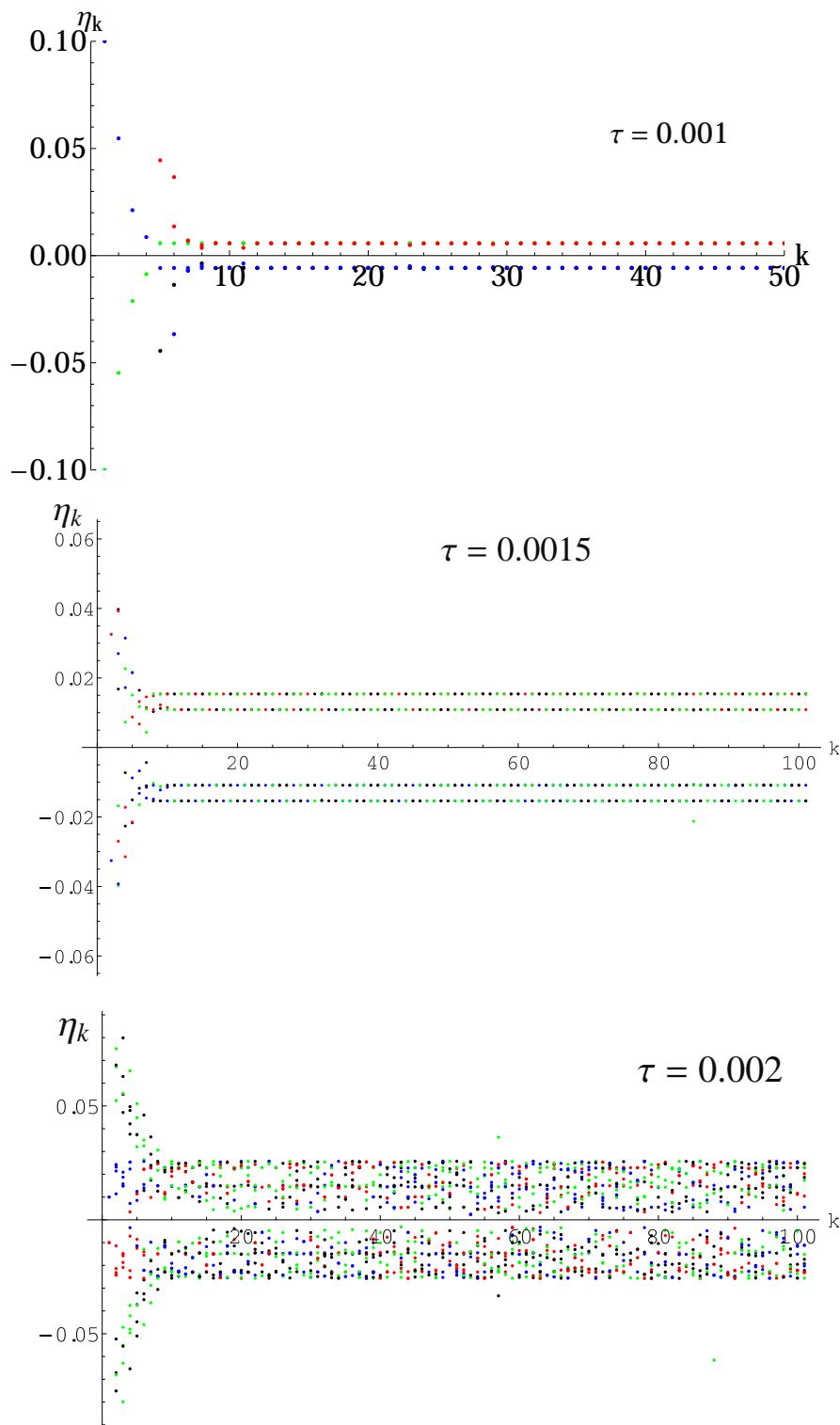
Figure 4.4: *Poincaré sections for several particles at different values of τ (Maxey-Riley equations with lift), marked by different colors. Upper graph: two attractors of unit period. Middle graph: two attractors with double period. Lower graph: chaotic dynamics.*
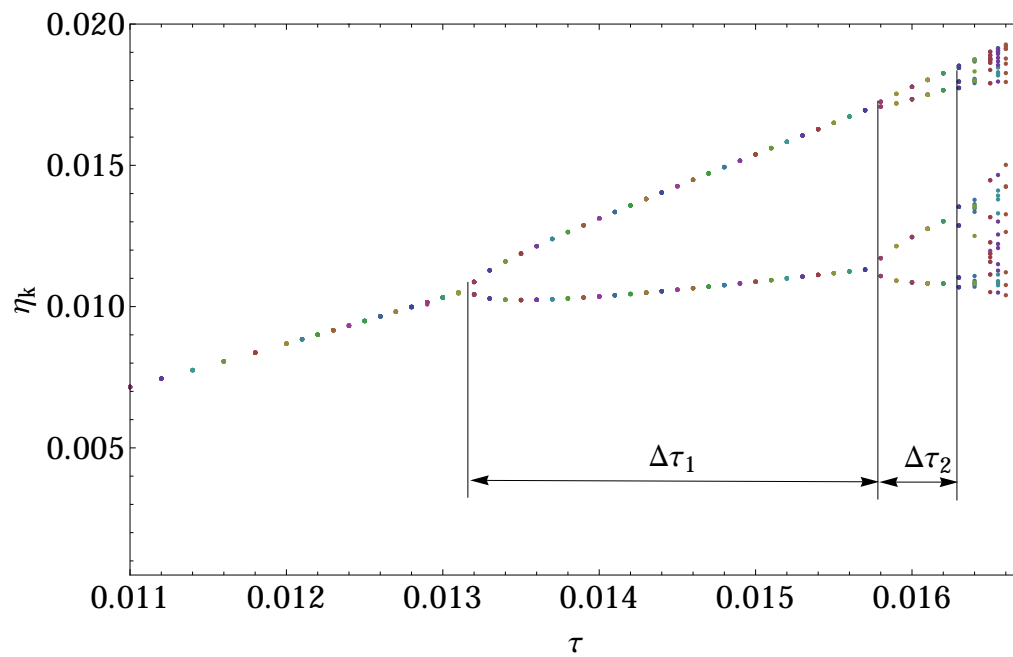
Figure 4.5: *The period-doubling diagram for Maxey-Riley equations with lift in the mirror-symmetric channel.*
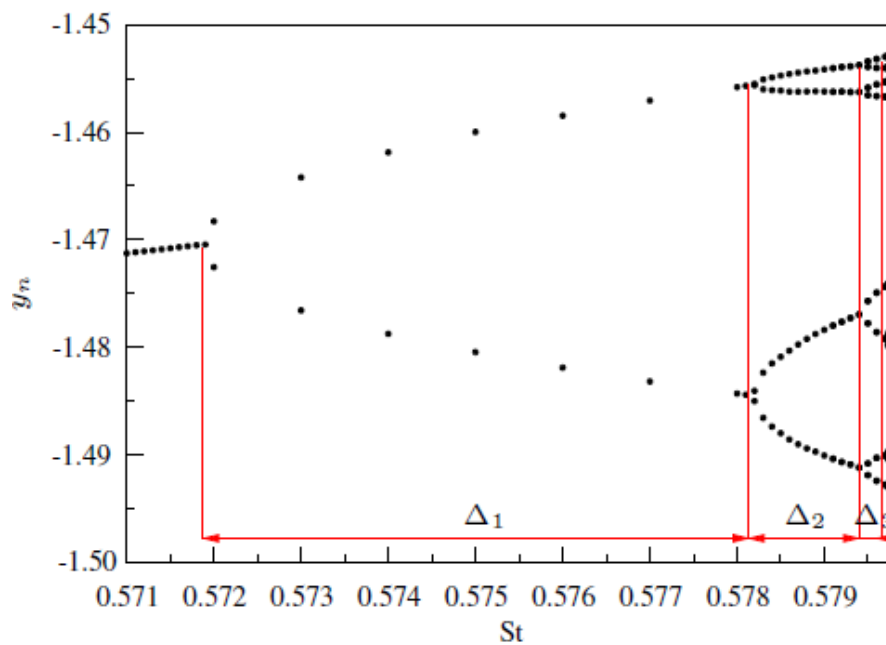

Figure 4.6: *Bifurcation diagram for sedimenting particles in the cellular flow (results from [19]).*

4.5 Second-order local approximation for the lift

Saffman's formula for the lift if formally valid only when the particle is far both from the walls and from the center of the channel, where the curvature of the velocity profile becomes important. In this section we take into account the parabolicity of the velocity profile, by using the lift based on approximation the flow around the particle by unbounded parabolic flow. This approximation has been proposed by Asmolov in [3] (we willl call it "Asmolov's lift" throughout the section).

Consider a unidirectional parabolic flow $\vec{U} = (U(Z), 0)$ and a particle moving in with a velocity V_p different from that of a fluid. In the coordinate system moving with the particle the undisturbed flow takes the following form:

$$U(Z') = V_s + \frac{dU}{dZ} Z' + \frac{d^2 U}{dZ^2} Z'^2,$$

where $Z' = Z - Z_p$ and $Z_p(t) = const$, because particle velocity is parallel to the flow.
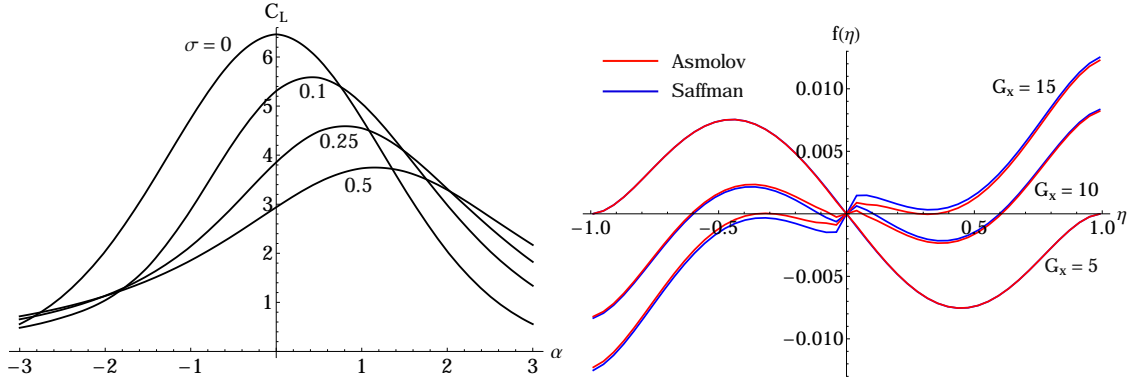
Figure 4.7: *Lift coefficient for the unbounded parabolic flow $C_L(\alpha, \sigma)$ (left). Migration functions $f(\eta_k) = \eta_{k+1} - \eta_k$ with Saffman's lift $C_L = 6.46$ and Asmolov's lift $C_L(\alpha, \sigma)$ (right).*

Following Section 4.2, we define the local variables (x', z') in the coordinate system translating with the particle: $x' = (\vec{x} - \vec{x}_p) \cdot \vec{s}$ and $z' = (\vec{x} - \vec{x}_p) \cdot \vec{n}$, where $(\vec{s}(\vec{x}_p), \vec{n}(\vec{x}_p))$ is the Frenet frame of the fluid streamline at point $\vec{x}_p$. In these variables the flow is almost unidirectional in z'. In non-dimensional variables rescaled by local shear rate

$\zeta = z'\sqrt{\text{Re}_K}$ this parabolic flow takes the following form (see [3]):

$$\bar{v}_K = \alpha + \zeta - \sigma\zeta^2,$$

where $\alpha = v_s\kappa^{-1/2}\text{Re}_H^{1/2}$ and (taking into account the gap of the channel) $\sigma = 4\kappa^{-3/2}\text{Re}_H^{-1/2}$, where $\kappa = -\dfrac{8\eta_p}{3h(x)}$ is the non-dimensional local shear rate at the particle position. Note that this definition of α is equivalent to $\alpha = \text{Re}_s/\sqrt{\text{Re}_K}$ with Re_K based on the local shear rate at the particle position.

The lift force can be written using the Saffman's formula with a modified coefficient $C_L(\alpha, \sigma)$ which now depends on two local parameters: α and σ. This coefficient is plotted in Fig. 4.5 (left) as a function of α for different value of σ ($C(\alpha, \sigma)$ is provided in [3] in the form of an interpolation table for $\alpha \in [-4; 4]$, $\sigma \in [-2; 2]$). We can see that even for small α (strong shear limit) the value of C_L depends strongly on σ. The case $\alpha = 0, \sigma = 0$ corresponds to simple shear flow and gives the Saffman's formula with $C_L(0, 0) = 6.46$.

To estimate the influence of parabolicity we compare the migration functions $f(\eta)$ calculated using the Saffman's lift coefficient C_L^0 and Asmolov's lift coefficient $C_L(\alpha, \sigma)$. Typical migration functions for a mirror-symmetric channel are provided in Fig. 4.5 (right). As expected, Saffman's formula gives a good approximation of the lift force when particles that are far both from the walls and from the center of the channel. In the center of the channel deviations become more important and we can see also that Saffman's formula slightly overestimates the lift force is overestimated (indeed, for the lift coefficient we always have $C_L(\alpha, \sigma) < C_L^0$). Therefore, the critical gravity numbers found in this chapter using Saffman's lift give an lower estimate for the real ones.

4.6   Conclusion

In this chapter we considered the influence of the lift force on particle focusing in the LCL flow, assuming that the channel Reynolds number Re_H is high (but the corrugation Reynolds number is small $\text{Re}_H\varepsilon < 1$). Under this assumption it is possible to approximate the lift force using local parameters of the flow and include it into Maxey-Riley equations

as an additive force.

For a horizontally aligned channel the lift-induced migration is always small compared to inertial forces: no significant change in particle behavior is expected. In a vertically-aligned channel gravity-induced lift and inertial forces work in opposite directions. This leads to appearance of multiple attractors and a complex structure of the trapping diagram. In contrast with purely inertial focusing (considered in Chapter 3), the attractor positions now depend on the size and density of the particle, which implies a possibility of hydrodynamic sorting in vertical channel.

We have also shown that for particles with finite response times addition of Saffman's lift force to Maxey-Riley equations leads to chaotic particle dynamics. We have constructed the bifurcation diagram for this case and have shown that transition to chaos happens through the classical Feigenbaum period-doubling tree.

To take into account the effect of the parabolicity, an advanced formula for the lift has been implemented (proposed by Asmolov in [3] and based on the approximation of the flow far from the walls by unbounded parabolic flow). Comparison of the resulting migration functions showed, that for small τ the difference between Saffman's and Asmolov's models is visible only in the very center of the channel. Therefore, we can hope that in the range of validity of the asymptotic model, Saffman's formula for the lift is sufficient.

However, in the central zone there is a significant difference between Saffman's and Asmolov's approximations for the lift. Therefore, the choice of lift can affect the chaotic particle behavior observed in the previous section. The influence of the lift model on particle dynamics at finite response times requires an additional study and has been left as a perspective to this thesis.

The asymptotic results obtained in this chapter concern only a very special case of high Reynolds numbers, when the influence of the walls is negligible in the core flow, so that the flow around the particle can be approximated as unbounded. For $\mathrm{Re}_H = O(1)$ this hypothesis is no longer valid. In this case lift-induced migration of non-neutrally buoyant particles in Poiseuille flow has been carefully investigated by A. Hogg [33] (in strong-shear limit $\mathrm{Re}_s \ll \mathrm{Re}_K^{1/2}$). He calculated the velocities of lift-induced migration for vertical and horizontal channels depending on particle position inside the channel for
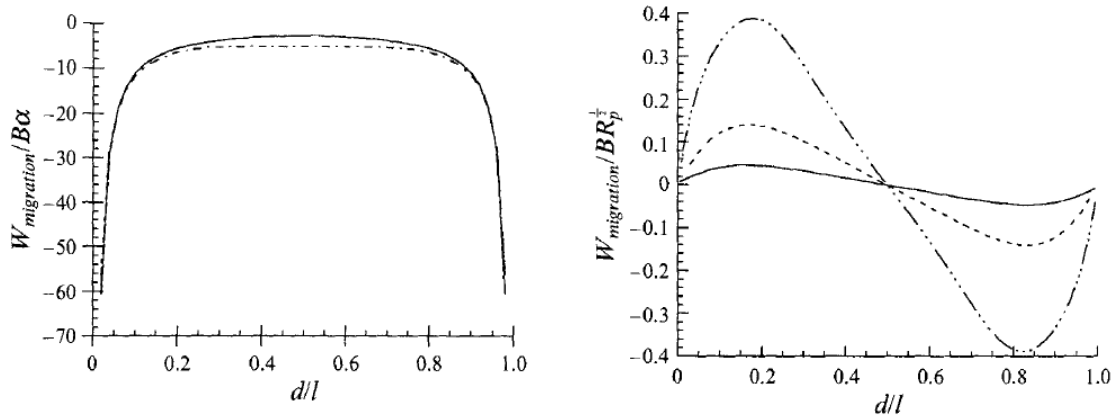
Figure 4.8: *Lift-induced migration velocity for a sedimenting particle with $Re_s \ll Re_K^{1/2}$ in a horizontal (left) and vertical (right) channels with Re_H ranging from 0.01 to 100. In the straight channel $W_{migration}$ corresponds to the migration function $f(\eta)$, and d/l corresponds to η. Results of A. Hogg [33].*

different channel Reynolds numbers Re_H, taking the walls into account when calculating the perturbed flow around the particle. Typical results for horizontal and vertical channels are provided in Fig. 4.8. The direction of lift coincides with one predicted by Saffman's formula, but the value of the lift coefficient decreases as the particle approached the wall and turns into zero on the wall itself. For the LCL flow we should expect the same kind of behavior, at least when particle migration due to corrugations are small compared to lift.

Chapter 5

Particle trapping in vortex pairs

In this chapter we study trapping of heavy particles ($R = 0$) in a different flow (interacting vortex pairs). This is a complementary study that has been carried out to check whether heavy particle trapping could happen also in non-periodic flows. Indeed, even if particle dynamics is dissipative, the phase space in this case is unbounded, so that the existence of an attractor is not guaranteed: particles are likely to be centrifuged to infinity. We observe that attractors do exist, in the form of either trapping points or limit cycles. The text of this chapter has been published in form of a letter [48].

5.1   Introduction

Particle accumulation is rather unexpected for heavy particles in vortical flows. Indeed, heavy particles are generally centrifuged away from vortical zones under the effect of their inertia. In this chapter we show that heavy particles can be trapped by vortex pairs, provided the particle response time and the vortex strength ratio lie in an appropriate range.

We have chosen the flow composed of two interacting vortices, as it was shown [1] that heavy particles released in a vortex pair with identical strengths can have 5 equilibrium positions in the reference frame rotating with the vortex pair, and that two of these positions are asymptotically stable : they can attract particles. These equilibrium posi-

tions result from the balance between the hydrodynamic force, which drives the particle towards the center point of the vortex system, and the centrifugal force which thrusts the particles outward. In the following sections, particle motion in a vortex pair with unequal strength is examined for all values of the vortex strength ratio.

5.2   Flow and particle motion equations in the co-rotating frame

We consider and incompressible and inviscid flow generated by a system of two point vortices with circulations Γ_1 and Γ_2, located at A_1 and A_2. Elementary vortex dynamics show that the distance $2d$ between the vortices remains constant, and that they rotate with a constant angular velocity $\Omega = (\Gamma_1 + \Gamma_2)/(8\pi)$ around a point I, satisfying $\Gamma_1 \overrightarrow{IA_1} + \Gamma_2 \overrightarrow{IA_2} = \vec{0}$, provided $\Gamma_1 + \Gamma_2 \neq 0$. In the reference frame rotating with the vortex pair the flow is steady, and vortices remain fixed. In non-dimensional form, using $1/\Omega$ for time
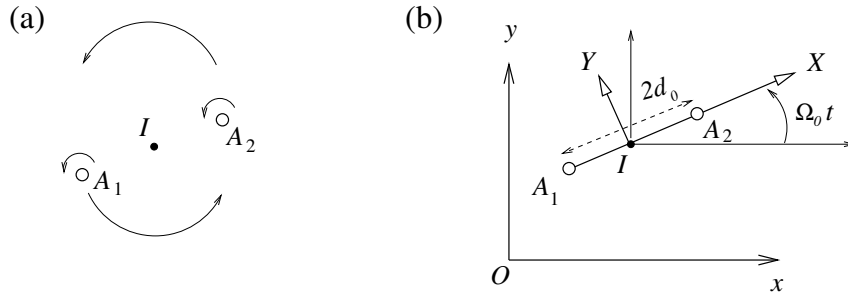

Figure 5.1: *Laboratory frame Oxy and rotating frame IXY.*

and d for lengths, the vortex positions in this frame are :

$$\vec{x}_1 = \left(-\frac{2}{\gamma + 1}, 0\right), \quad \vec{x}_2 = \left(\frac{2\gamma}{\gamma + 1}, 0\right), \quad \gamma = \Gamma_1/\Gamma_2$$

where the coordinate system (x, y) is centered at I, with Ix parallel to $A_1 A_2$ (Fig. 5.1). The fluid velocity field reads $\vec{V}_f(\vec{x}, \gamma) = \left(\frac{\partial \Psi}{\partial y}, -\frac{\partial \Psi}{\partial x}\right)$, where Ψ is the streamfunction in the co-rotating frame which can be written as :

$$\Psi(\vec{x}) = \gamma \Phi(\vec{x} - \vec{x}_1) + \Phi(\vec{x} - \vec{x}_2) + |\vec{x}|^2/2,$$

with $\Phi(\vec{x}) = -\frac{2}{1+\gamma} \ln |\vec{x}|$. The vorticity is constant and equals -2 everywhere, except at the vortex centers. Figs. 5.2 and 5.3 shows typical relative streamlines $\Psi = constant$ for various strength ratios γ.

Particles are assumed to be non-interacting, non-brownian, much heavier than the fluid, and with a low-Reynolds number. Clearly, the first approximation is no longer valid when particles tend to accumulate (see for example Medrano *et al.* [46]). However, we will use it for the sake of simplicity in this paper, and keep the effect of particle interactions as a perspective to this work. The simplest motion equation of these low-Reynolds number heavy particles reads, in non-dimensional form :

$$\tau \frac{d^2 \vec{X}_p}{dt^2} = \vec{V}_f(\vec{X}_p) - \frac{d\vec{X}_p}{dt} + \tau \left(\vec{X}_p - 2\vec{e}_z \times \frac{d\vec{X}_p}{dt} \right) \tag{5.1}$$

where $\vec{X}_p(t) = (x_p, y_p)$ denotes the particle position at time t, $\vec{e}_z$ is the unit vector along the z axis, and τ is the non-dimensional response-time of the particle (Stokes number). For spherical particles with mass m_p and radius a the Stokes number reads $\tau = \Omega m_p/(6\pi\mu a)$, where μ is the fluid viscosity. The last two terms in equation (5.1) are the (non-dimensional) centrifugal and Coriolis pseudo-forces respectively. Because particles are much heavier than the fluid, Eq. (5.1) is valid even if the Stokes number τ is not small, as added mass force, pressure gradient of the undisturbed flow, lift and Basset force are negligible.

5.3 Particle trapping conditions

Introducing a new vector variable $\vec{z} = (x_p, y_p, \dot{x}_p, \dot{y}_p)$, equation (5.1) can be rewritten as a system of first order equations:

$$\begin{cases} \dot{z}_1 = z_3 \\ \dot{z}_2 = z_4 \\ \dot{z}_3 = -z_3/\tau + z_1 + 2z_4 + u_x(z_1, z_2, \gamma)/\tau \\ \dot{z}_4 = -z_4/\tau + z_2 - 2z_3 + u_y(z_1, z_2, \gamma)/\tau, \end{cases} \tag{5.2}$$

where $\vec{V}_f = (u_x, u_y)$. In vector form this set of equations writes $d\vec{z}/dt = \vec{F}(\vec{z}, \gamma, \tau)$. To find the conditions of particle trapping, we search for attracting equilibrium points of (5.2): $\vec{F}(\vec{z}, \gamma, \tau) = \vec{0}$. If all the eigenvalues of $\nabla\vec{F}$ have negative real parts, then $\vec{X}_{eq}$ is asymptotically stable. It can be shown (see Appendix B) that the eigenvalues of $\nabla\vec{F}$ at the equilibrium point only depend on the jacobian $J = u_{x,x}u_{y,y} - u_{y,x}u_{x,y}$ (the comma indicates spatial derivation) of the velocity field at this point, and the stability criterion is $-\tau^2 < J < 1$. For our velocity field the condition $J < 1$ is automatically satisfied. Let $\vec{X}_{eq}$ be an equilibrium point :

$$\vec{f}(\vec{X}_{eq}, \gamma, \tau) = \vec{X}_{eq} + \vec{V}_f(\vec{X}_{eq}, \gamma)/\tau = 0.$$

By virtue of the implicit functions theorem, $\vec{X}_{eq}$ depends smoothly on (γ, τ), unless $\det(\nabla\vec{f}|_{X_{eq}}) = 0$. Because $\det(\nabla\vec{f}|_{X_{eq}}) = J/\tau^2 + 1$, this condition coincides exactly with the boundary of the stability domain. Hence, the point $\vec{X}_{eq}$ will exist and remain stable until (γ, τ) reaches some critical value defined by the system of equations:

$$\begin{cases} \vec{X}_{eq} + \vec{V}_f(\vec{X}_{eq}, \gamma)/\tau = 0 \\ J(\vec{X}_{eq}, \gamma) + \tau^2 = 0. \end{cases} \tag{5.3}$$

This is a system of 3 equations for 4 variables $(\vec{X}_{eq}, \tau, \gamma)$, which defines a family of curves in a four-dimensional space. The projection of these curves on the (τ, γ)-plane splits it into domains, within which the number (and stability properties) of equilibrium points doesn't change. It is therefore sufficient to investigate the stability of equilibrium points for just one set of parameters (γ, τ) from each domain to get the full picture.

To find these critical curves we took a grid covering $\gamma \in (-1; 1]$ and for each γ solved the system (5.3) numerically. The resulting trapping diagram is shown in Fig.5.4.

As expected, for $\gamma = 1$ the critical value of τ coincides with one obtained analytically for identical vortices [1] : $\tau = 2 - \sqrt{3}$. Numerical simulations of particle clouds have been run for the sets of parameters (A,B,C,D,E,F) marked on figure 5.4. At the initial state the particles were randomly distributed in a square $[-3; 3] \times [-3; 3]$ with the velocities equal to the velocity of the fluid. Figs. 5.2 and 5.3 present the resulting particle clouds
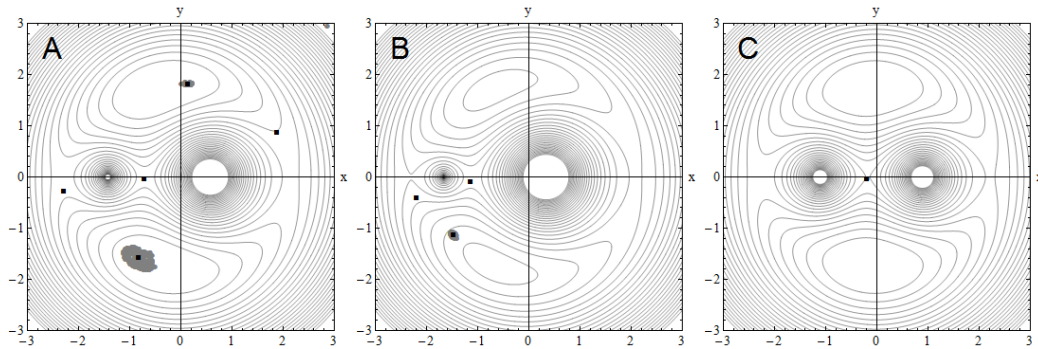
Figure 5.2: *Flow streamlines and particle clouds for co-rotating vortices with different sets of parameters : A:* $\gamma = 0.4$, $\tau = 0.1$ *; B:* $\gamma = 0.2$, $\tau = 0.2$ *; C:* $\gamma = 0.8$, $\tau = 0.4$.
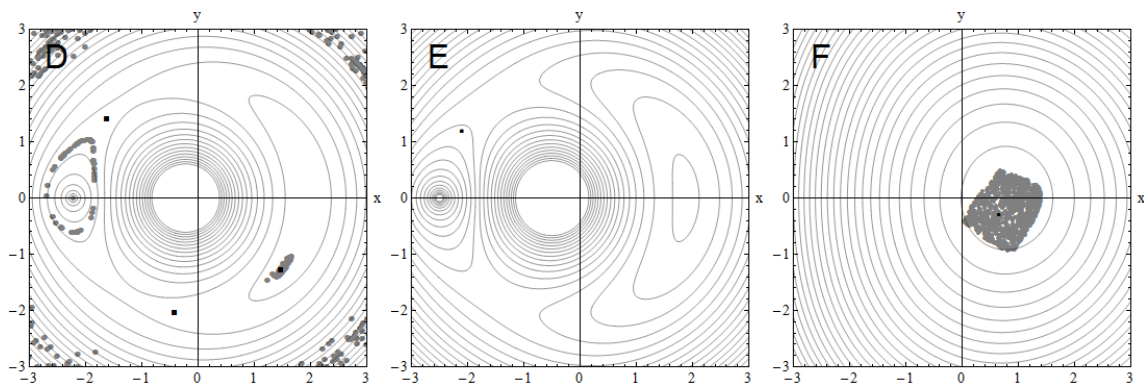

Figure 5.3: *Flow streamlines, particle clouds (gray points) and equilibrium positions (black squares) for contra-rotating vortices with different sets of parameters : D:* $\gamma = -0.1$, $\tau = 0.05$ *; E:* $\gamma = -0.2$, $\tau = 0.2$ *; F:* $\gamma = -0.8$, $\tau = 0.4$.

at $t = 50$ for points from A to E and at $t = 500$ for F (particles take much longer time to converge in this case). We observe that some particles converge to the attracting points predicted by the diagram, except in cases C and E, as expected.
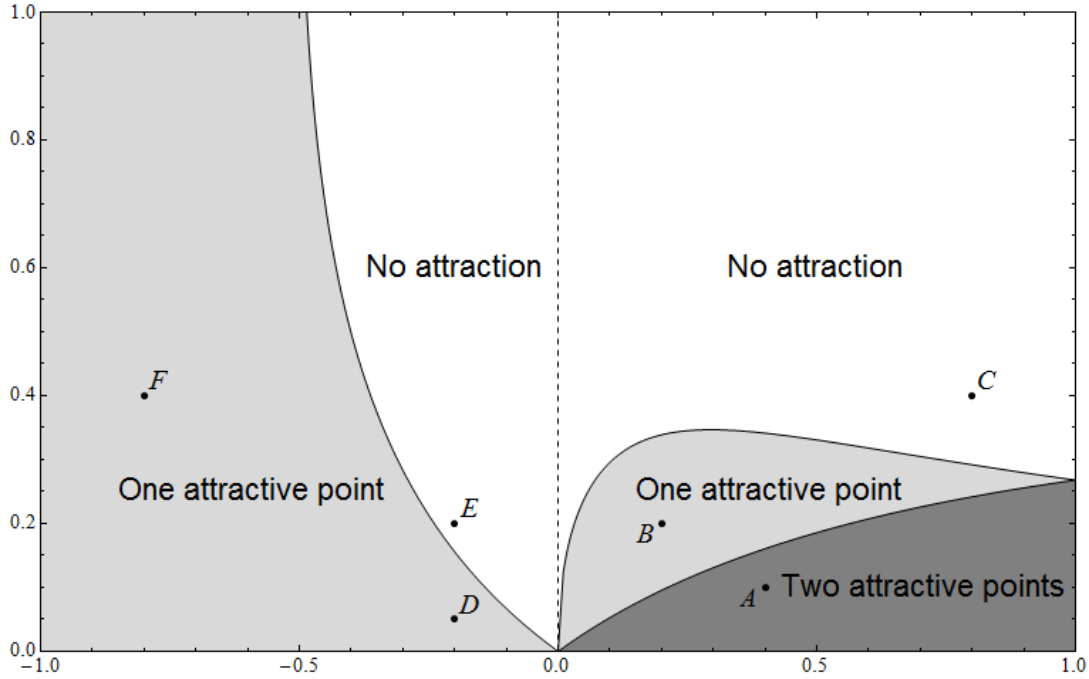

Figure 5.4: *Particle trapping diagram.*

5.4   Particle trapping inside a limit cycle

Figure 5.3D suggests that, apart from the attracting points, a limit cycle could exist for small τ and relatively small negative γ. The existence of a limit cycle can be predicted by using a criterion by Sapsis and Haller [57]. To adapt this criterion to our equations we repeat the procedure from these authors, introducing a slow time variable $\tau s = t - t_0$ and expanding the solution with respect to τ. This procedure leads us to the following inertial equation:

$$\frac{d\vec{X}_p}{dt} = \vec{V}_f(\vec{X}_p) + \tau \left[\vec{X}_p - 2\vec{e}_z \times \vec{V}_f - \nabla \vec{V}_f . \vec{V}_f \right].$$
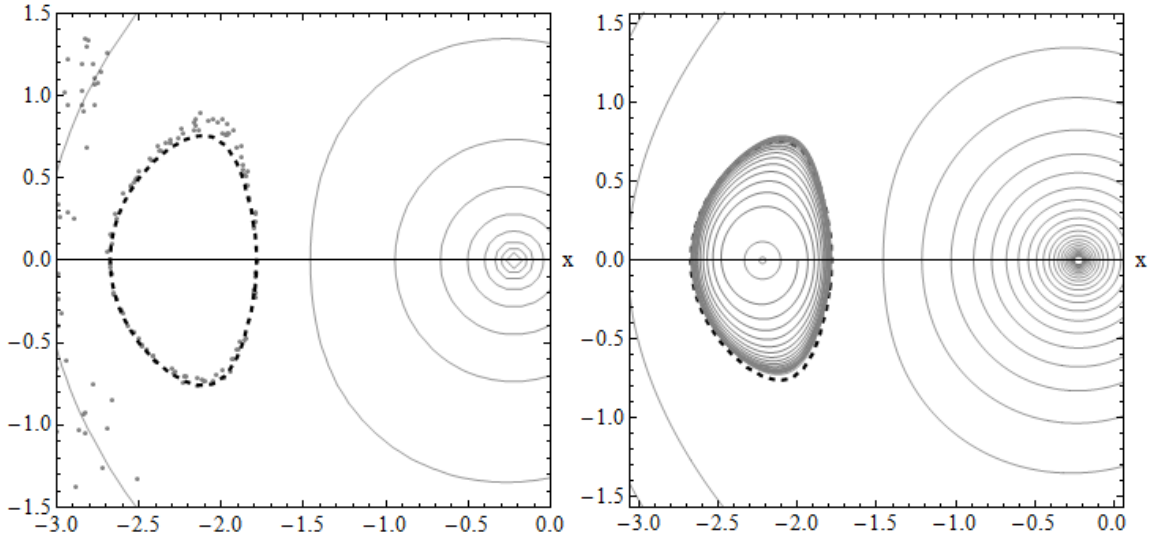
Figure 5.5: *Particle cloud at $t = 50$ for $\gamma = -0.1, \tau = 0.01$ (grey points) compared with the predicted limit cycle (dashed black line).*

Writing down the phase volume conservation condition, with the use of the equation above we get the following criterion :

$$I(S_0) = \int\limits_{S_0} \left[\vec{X}_p - 2\vec{e}_z \times \vec{V}_f - \nabla\vec{V}_f.\vec{V}_f \right] .\vec{n}dS = 0,$$
$$\frac{dI}{dn} < 0,$$

where $\vec{n}$ is the outer normal to S_0, S_0 is a streamline of the fluid velocity field $\vec{V}_f$, being also a level-line of the stream function Ψ. Now the problem is to find a value Ψ_0 such that $I(S_0(\Psi_0)) = 0$. This is a one-dimensional root-finding problem, which can be solved by applying the simplest bisection method, which doesn't require any additional information on I. The value of I at any given Ψ is obtained by numerical integration along the corresponding streamline. For $\gamma = -0.1$ this procedure converges to the value of $\Psi_0 \approx -0.761$. The simulation carried out for particles with $\tau = 0.01$ confirm that the limit cycle indeed lies quite close to this streamline (Fig. 5.5). With the increase of τ the limit cycle diverges from this curve and finally merges with a neighbouring unstable equilibrium point.

5.5   Conclusion

We have shown that inviscid vortex pairs can permanently trap heavy particles, provided the vortex strength ratio and the particle response time lie in the grey zones of the trapping diagram shown in Fig. 5.4. Trapping can occur in the vicinity of various attracting points rotating with the vortex pair, where the centrifugal force balances the Stokes drag, for both co-rotating or contra-rotating vortices. In the latter case a limit cycle has been observed and confirmed by using Sapsis & Haller's method [57]. Trapping leads to large collision rates and could be of interest to understand the detailed dynamics of various particle-laden flows where vortex pairing is known to occur. For example, anti-cyclonic vortices in protostellar disks are known to trap particles, with the help of the Coriolis force due to the disk rotation (see for example Chavanis [13]). The analysis of the behavior of particles during the pairing of anticyclonic vortices could therefore be a topic of interest.

Chapter 6

Conclusion

Single-phase and particle-laden flows through a thin periodic fracture have been investigated using asymptotic methods and dynamical system tools.

For single-phase flow in the fracture, an asymptotic solution in the limit of thin channel has been found for arbitrary wall shapes. This analytic approach permits to link the geometrical properties of the fracture to inertial corrections in Darcy's law. Corrections are cubic in flow rate for any channel and depend on two scalar geometric factors: one of them is responsible for aperture variation and the other one reflects the corrugation of the mean profile of the channel.

In the case of particle-laden flows, the dynamics of inclusions in this asymptotic velocity field has been investigated using Poincaré maps. As expected, inertial effects make particles focus to a single attracting trajectory. This effect persists in the presence of transverse gravity, provided the Froude number is above some critical value.

This leads to two different regimes of particle transport in a horizontal flow. When gravity dominates over hydrodynamic forces, all particles are deposited on the walls. When inertia is strong enough to balance out the gravity, particles focus to some attractor inside the channel. In this case a considerable number of particles can avoid sedimentation and travel long distances on the attractor (permanent suspension). The full trapping diagram has been obtained, that predicts focusing/sedimentation regime depending on the Froude number and on geometric factors. Particle behavior is sensitive to the geometry of the channel: aperture variation affects focusing rates and the corrugation asymmetry

determines the position of the attracting streamline. The sedimentation length depends on both of the parameters.

In a vertical channel the influence of the lift force on particle migration is non-negligible and has to be taken into account. Indeed, in a downward flow heavy particles lead the fluid and the lift force pushes them to the walls: lift effect works against the corrugation-induced focusing. This leads to the appearance of multiple attractors, and to complex trapping diagrams: multiple particle attractors appear, the position of which depends on the density of the particles. The predictive power of these diagrams is limited by the quality of the lift approximation.

Numerical simulations confirm the asymptotic results for particles with small response times: they do focus to the attractor predicted by the theory. However, with the increase of the particle response time a series of bifurcations occurs with the attractor splitting into multiple well-separated branches. This effect can lead to hydrodynamic sorting of particles with different size or density. Including the lift force into motion equations for finite response times leads to an even more complex behavior: in the absense of gravity particles can undergo chaotic motion through a period doubling cascade.

For dust particles in an unbounded and non-periodic flow (vortex pair), where the existence of the attractor is not guaranteed, trapping points have been shown to exist. A full trapping diagram has been obtained, showing that any pair of vortices can trap particles, independently of their strength ratio and the direction of rotation. For contra-rotating vortices, the existence of a limit cycle has been proved theoretically and confirmed by numerical simulations.

Perspectives

The most important perspective of this work is experimental verification of the predicted focusing effect. The simplest measurable parameter of the model is the deposition length of the particles: it can be observed visually and predicted theoretically by Eq. (3.22). The supercritical regime ($G > G_{cr}$) can be visually discovered by the presence of a clear zone in the lower part of the channel. Indeed, if an attractor exists, there exists also a repulsor (see Fig. 3.6). All particles below this latter will be deposited in a finite time, while no particles from the upper zone will appear (none of them can cross the repulsive

streamline). However, some rough estimates (see the Conclusion to Chapter 3) suggest the focusing conditions in the laboratory scale fracture are difficult to achieve in a horizontal flow, unless the viscosity of the fluid is large. A horizontal synthetic fracture with wavy walls has already been built in LAEGO (and a vertical fracture is in project), and the first tests for single-phase and particle-ladden flows have been performed by H. Stokes during her Master's project in 2011. In these test the presence of recirculation zones has been detected in the working range of parameters (in full accordance with previous studies [62]). This leads us immediately to the next perspective of this thesis.

In this thesis only small and moderate Reynolds numbers of the channels have been considered. At higher Reynolds numbers the appearance of the recirculation zones can significantly change particle behavior in the flow. In particular, particles could be trapped in recirculation zones under certain conditions. To investigate the possibility of such trapping the single-flow model used in this thesis should be revisited (the asymptotic solution of Chapter 2 is no longer valid in presence of recirculation).

Another important perspective is generalization of the theory to the case of non-periodic (disordered) and non-smooth fractures. The results of the Chapter 2 can be applied to non-periodic fractures directly (periodicity was not implied there). However, singularities of the wall shapes will lead to singularities in the Navier-Stokes equations and to complex mechanisms of fluid behavior (see Panfilov *et al.* [52]). For particle-laden flows (Chapter 3) periodicity is crucial both for the focusing phenomenon itself, and for the methods applied to its study. In a non-periodic fracture there would be no focusing to a single trajectory, but some more complex clustering effects should be present. In this case clustering can be quantified by considering the evolution of the distance between neighboring particles (Lyapunov exponents) or by investigating the statistical properties of the particle velocity field (measuring the cross-channel momentums of particle distribution).

Finally, a model of particle motion in the vicinity of the walls should be developed. A combined effect of the gravity, the wall-induced lift force and the ionic particle-wall interaction forces can lead to non-trivial behavior of particles in these zones, especially when the wall shapes are not smooth.

Appendix A

Particle focusing in potential flow

In this appendix we consider particle focusing in a potential flow through a corrugated channel. Particle transport in such a flow has been studied by Fernandez de la Mora in [24], where he solved particle motion equations explicitly (for small corrugation amlitude). Ferndndez de la Mora considered channels with both mirror-symmetric and parallel walls and showed that aerosol particles ($R = 0$) cluster in both cases with essentially the same compression rate. Here we calculate the Poincaré map for this flow and confirm his results theoretically for weakly-inertial particles. Following Fernandez de la Mora [24] we considered two basic geometries:

$$\text{(a) mirror-symmetric: } \Psi(x, z) = U_0 z + A \cdot \sinh(kZ) \sin(kX),$$
$$\text{(b) parallel: } \Psi(x, z) = U_0 z + A \cdot \cosh(kZ) \sin(kX).$$

where U_0 is the mean flow velocity, A is the corrugation amplitude, k is the frequency of corrugation (in [24] the case (a) is called "symmetric", and the case (b) "antisymmetric"). In non-dimensional variables ($L = 2\pi/k$) the velocity field takes the following form:

$$\begin{aligned}(a) \quad & u_x^M(x, z) = 1 + \delta \cdot \cosh(2\pi z) \cos(2\pi x), \\ & u_z^M(x, z) = -\delta \cdot \sinh(2\pi z) \cos(2\pi x). \\ (b) \quad & u_x^P(x, z) = 1 + \delta \cdot \sinh(2\pi z) \cos(2\pi x), \\ & u_z^P(x, z) = -\delta \cdot \cosh(2\pi z) \cos(2\pi x).\end{aligned}$$

where $\delta = Ak/U_0$ is the non-dimensional corrugation. The fluid trajectory starting at point (x_0, z_0) with $\Psi_0 = \Psi(x_0, z_0)$ can be approximated for small δ in the following way:

$$(a) \quad z_f^M(x) = \Psi_0 - \delta \sinh(2\pi z_0) \sin(2\pi x) + O(\delta^2),$$
$$(b) \quad z_f^P(x) = \Psi_0 - \delta \cosh(2\pi z_0) \sin(2\pi x) + O(\delta^2).$$

Substituting this into (3.5) and expanding into series of δ we get exactly the same leading-order term for mirror-symmetric and parallel flows:

$$I_0^{P,M}(z_0, G) \approx (3R/2 - 1)(G - \pi\delta^2 \sinh(4\pi z_0)) + O(\delta^3)$$

and essentially the same compression rate:

$$I_1^{P,M}(z_0) = \frac{dI_0^{P,M}}{dz_0} \left(\frac{\partial \Psi_{P,M}}{\partial z_0} \right)^{-1} \approx (3R/2 - 1)4\pi^2\delta^2 \cosh(4\pi z_0)). \tag{A.1}$$

This result is in accordance with observations of Fernandez de la Mora [24] and is very different from one obtained for the LCL flow (no focusing for parallel walls).
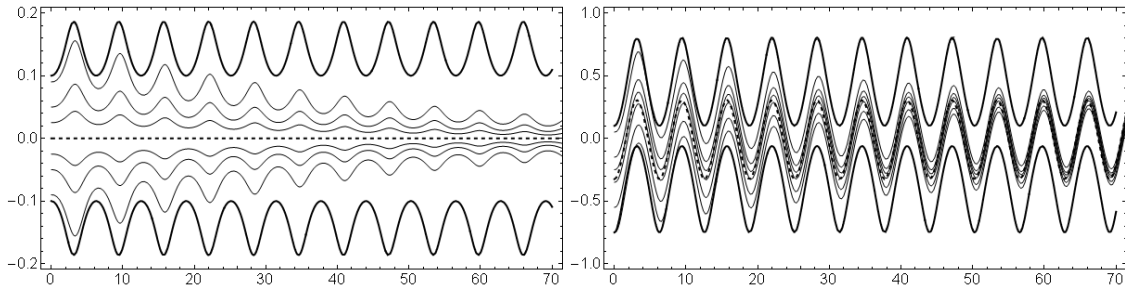

Figure A.1: Particle trajectories for mirror-symmetric (left) and parallel (right) flows ($\delta = 0.3, \tau = 0.25$).

In fact, one can easily show that (in the absence of gravity) in any unidirectional periodic flow with mirror-symmetry small heavy particles are attracted to the axis of symmetry (let it be $z = 0$). Indeed, if we calculate the integrals in (3.5) taking into account

that $u_z \equiv 0$ and $\dfrac{\partial u_x}{\partial z} \equiv 0$ on the axis of symmetry, we get:

$$I_0 = \tau \int\limits_0^1 \vec{V}_p^1(x,0) \cdot \vec{e}_z dx = 0,$$

$$I_1 = \tau \int\limits_0^1 \left(\frac{\partial}{\partial z}(\vec{V}_p^1(x,z) \cdot \vec{n}) \right) \Bigg|_{z=0} dx = 3\tau(3R/2 - 1) \int\limits_0^1 \left(\frac{\partial u_0}{\partial x} \right)^2 dx,$$

so that $\beta = 3 \int\limits_0^1 \left(\dfrac{\partial u_0}{\partial x} \right)^2 dx$, where $u_0(x) = u_x(x,0)$.

Substituting our velocity field we find that the first order-estimate for I_1 is exact for the mirror-symmetric flow:

$$I_1^M = (3R/2 - 1)4\pi^2\delta^2.$$

Therefore, in the potential flow model parallel and mirror-symmetric geometries can focus particles with same efficiency, which is in huge contrast with the results obtained for LCL flow (no focusing for parallel walls).

Appendix B

Stability condition of the equilibrium points in a vortex pair.

Consider the characteristic equation of (5.2), taking into account the properties of the flow (vorticity equals -2, divergence equals 0):

$$\lambda^4 + \frac{2}{\tau}\lambda^3 + \left(2 + 1/\tau^2\right)\lambda^2 + 1 + J/\tau^2 = 0,$$

where λ denotes any eigenvalue of $\nabla \vec{F}$. Using the change of variables $\zeta = \lambda + 1/2\tau$, we obtain a biquadrate equation:

$$16\tau^4\zeta^4 + 8\tau^2(4\tau^2 - 1)\zeta + 8\tau^2(2\tau^2 + 2J - 1) + 1 = 0$$

which has the following roots: $\zeta_\pm^2 = (1 - 4\tau^2)/4\tau^2 \pm \sqrt{-J}/\tau$. Consider two possible cases: $J < 0$ and $J > 0$.

When $J < 0$, $\zeta_\pm^2$ are both real and $\zeta_+^2 > \zeta_-^2$. Now if $\zeta_-^2 < \zeta_+^2$, all the roots $\zeta_\pm^{(1,2)}$ are imaginary, so $\mathrm{Re}[\lambda] = -1/2\tau$ and the equilibrium point is stable. If at least $\zeta_+^2 > 0$, then $\zeta_+^{(1,2)} = \pm\sqrt{\zeta_+^2}$ and $\max \mathrm{Re}[\lambda] = \sqrt{\zeta_+^2} - 1/2\tau$. After some simple manipulations we find that $\max \mathrm{Re}[\lambda] > 0 \Leftrightarrow J < -\tau^2$.

When $J > 0$ the roots of biquadrate equation are complex-conjugate: $\zeta_\pm^2 = 1/4\tau^2 - 1 \pm i\sqrt{J}/\tau = a \pm ib$. Using trigonometric representation and the Moivre formula, we find

that $\zeta_{\pm}^{(1)} = r^{1/2}(\cos\varphi/2 \pm i\sin\varphi/2)$ and $\zeta_{\pm}^{(2)} = -\zeta_{\pm}^{(1)}$, where $r = \sqrt{a^2 + b^2}$, $\cos\varphi = a/r$,

so

$$\max \text{Re}[\lambda] = |r^{1/2}\cos\varphi/2| - 1/2\tau.$$

Using the fact that $\cos^2\varphi/2 = (1 + \cos\varphi)/2$ we find that $\max\text{Re}[\lambda] > 0 \Leftrightarrow J > 1$. Combining these results, we obtain the stability criterion : the equilibrium point $\vec{X}_{eq}$ is stable if and only if $\tau^2 < J(\vec{X}_{eq}, \gamma) < 1$.

Bibliography

[1] J.R. Angilella. Dust trapping in vortex pairs. *Physica D: Nonlinear Phenomena*, 239:1789–1797 (2010).

[2] E. Asmolov. Lift force exerted on a spherical particle in a laminar boundary layer. *Fluid Dyn.* 24, 710-714 (1989).

[3] E. Asmolov. The inertial lift on a spherical particle in a plane Poiseuille flow at large channel Reynolds number. *J. Fluid Mech.* 381: 63-87 (1999).

[4] T. R. Auton, F. C. R. Hunt, and M. Prudhomme. The force exerted on a body in inviscid unsteady non-uniform rotational flow. *J. Fluid. Mech.*, 197, 241 (1988).

[5] P. Barge and J. Sommeriat. Did planet formation begin inside persistent gaseous vortices? *Astron. Astrophys.*, 295:L1–L4 (1995).

[6] G. Batchelor. An Introduction to Fluid Dynamics. Cambridge University Press, New York (1967).

[7] V. Borisov. Viscous liquid flow in a channel with sinusoidal walls, *Journal of Engineering Physics and Thermophysics*, 42(4), 399-401 (1982).

[8] S. R. Brown. Simple mathematical model of a rough fracture, *J. Geophys. Res.* 100(B4), 5941- 5952 (1995).

[9] D. J. Brush. Three-Dimensional Fluid Flow and Solute Transport in Rough-Walled Fractures. A thesis of University of Waterloo (2001).

[10] M. Buès, M. Panfilov, S. Crosnier, C. Oltean. Macroscale Model and Inertia-Viscous Effects for Navier-Stokes Flow in a Radial Fracture with Corrugated Walls *J. Fluid Mechanics*, v. 504, p. 41-60 (2004).

[11] F. Candelier and J.R. Angilella. Analytical investigation of the combined effect of fluid inertia and unsteadiness on low-Re particle centrifugation. *Physical Review E* 73, 047301 (2006).

[12] J. Cartwright, U. Feudel, G. Karolyi, A. De Moura, O. Piro, & T. Tel. Dynamics of finite-size particles in chaotic fluid flows. In *Nonlinear Dynamics and Chaos: Advances and Perspectives* (ed. M. Thiel). Springer-Verlag, Berlin (2010)

[13] P. H. Chavanis. Trapping of dust by coherent vortices in the solar nebula. *Astronomy and Astrophysics*, 356:1089–1111 (2000).

[14] H. Choi, D. Joseph. Fluidization by lift of 300 circular particles in plane Poiseuille flow by direct numerical simulation. *J. Fluid Mech.* 438 (2001).

[15] B. Chun, A. J. Ladd. Inertial migration of neutrally buoyant particles in a square duct: An investigation of multiple equilibrium positions. *Phys. Fluids*, 18(3), 031704 (2006).

[16] S. Cronier. Ecoulement dans une fracture de géométrie radiale - Influence d'une rugosité périodique. *Thèse de INPL* (2002).

[17] B. Dahneke. Aerosol beams. in: D.T. Shaw (Ed.), *Fundamentals of Aerosol Science,* NewYork: Wiley. (1978).

[18] Dino Di Carlo, Daniel Irimia, Ronald G. Tompkins, and Mehmet Toner. Continuous inertial focusing, ordering, and separation of particles in microchannels. *PNAS*, vol. 104, no. 48 (2007).

[19] S. Domesi and H. C. Kuhlmann. Particle motion in a spatially periodic flow. *Proc. Appl. Math. Mech.* 5, 593 - 594 (2005).

[20] O.A. Druzhinin and L.A. Ostrovsky. The influence of the Basset force on a particle dynamics in two-dimensional flows. *Physica D* 76, 34 - 43 (1994).

[21] G. Falkovich, A. Fouxon, M.G. Stepanov. Acceleration of rain initiation by cloud turbulence. *Nature*, 419(6903):151 (2002).

[22] H. Faxèn, "Der Widerstand gegen die Bewegung einer starren Kugel in einer zähen Flüssigkeit, die zwischen zwei parallelen ebenen Wänden eingeschlossen ist", Annalen der Physik 373 (10): 89-119 (1922).

[23] M. J. Feigenbaum. Quantitative Universality for a Class of Non-Linear Transformations. J. Stat. Phys. 19: 25-52, (1978).

[24] J. Fernàndez de la Mora. Aerodynamic focusing in spatially periodic flows:Two-dimensional symmetric and antisymmetric channels. *Journal of Aerosol Science*, 37, 323-339 (2006).

[25] M. Firdaouss, J.-L. Guermond and P. Le Quéré. Nonlinear corrections to Darcy's law at low Reynolds numbers, *J. Fluid Mech.* 343, 331 (1997).

[26] P. Forchheimer. Wasserbewegung durch Boden. *Zeit. Ver. Deut. Ing.*, (45): 1781-1788 (1901).

[27] R. Gatignol. The Faxén formulae for a rigid sphere in an unsteady non-uniform Stokes flow. *J. Méc. Théor. Appl.*, 1, 143–160 (1983).

[28] D. R. Gossett and Dino Di Carlo. Particle Focusing Mechanisms in Curving Confined Flows *Anal. Chem.* 81, 8459-8465 (2009).

[29] J. Guckenheimer and P. J. Holmes. Nonlinear Oscillations, Dynamical Systems, and Bifurcations of Vector Fields. Springer-Verlag, New York (1983).

[30] G. Haller & T. Sapsis. Where do inertial particles go in fluid flows? *Physica D*, 237 573-583 (2008).

[31] E. Hasegawa, H. Izuchi. On steady flow through a channel consisting of an uneven wall and a plane wall. *Bull Jap. Soc. Mech. Eng.*, 26, 514 (1983).

[32] B. P. Ho and L. G. Leal. Inertial migration of rigid spheres in two-dimensional unidirectional flows. *J. Fluid Mech.*, 65 : pp 365-400 (1974).

[33] A. J. Hogg. The inertial migration of non-neutrally buoyant spherical particles in two-dimensional shear flows. *J. Fluid Mech.* 212, 285-318 (1994).

[34] R. H. A. Ijzermans and R. Hagmeijer. Accumulation of heavy particles in N-vortex flow on a disk. *Phys. Fluids*, 18:063601 (2006).

[35] G. W. Israel, and S. K. Friedlander. *Journal of Colloid and Interface Science,* 24, 330 (1967).

[36] D. Lo Jacono, F. Plouraboué, A. Bergeon, Weak-inertial flow between two rough surfaces. *Phys. Fluids*, 17, 063602 (2005).

[37] P.K. Kitanidis, B.B. Dykaar, Stokes Flow in a Slowly Varying Two-Dimensional Periodic Pore,*Transport in Porous Media*, 26, 89 (1997).

[38] T. Koyama, I. Neretnieks, L. Jing, "A numerical study on differences in using Navier-Stokes and Reynolds equations for modeling the fluid flow and particle transport in single rock fractures with shear"*International Journal of Rock Mechanics and Mining Sciences*, 45 (7), 1082 (2008).

[39] Y. Lucas, M. Panfilov, M. Buès. High velocity flow through fractured and porous media: the role of flow non-periodicity. *European Journal of Mechanics, B/Fluids*, 26, 295-303 (2007).

[40] J.P. Matas, J.F. Morris, E. Guazzelli. Lateral Forces on a Sphere. *Oil Gas Science and Technology*, 59(1), 59-70. (2004)

[41] M.R. Maxey, The motion of small spherical particles in a cellular flow field, *Phys. Fluids* 30, 1915-1928, (1987)

[42] M.R. Maxey. The gravitational settling of aerosol particles in homogeneous turbulence and random flow fields. *J. Fluid Mech.*, 174:441–465(1987).

[43] M. Maxey, S. Corrsin. Gravitational Settling of Aerosol Particles in Randomly Oriented Cellular Flow Fields. *J. Atmos. Sci.*, 43, 1112-1134 (1986).

[44] M.R. Maxey and J.J. Riley. Equation of motion for a small rigid sphere in a nonuniform flow, *Phys. Fluids* 26, 883-889 (1983).

[45] J.B. McLaughlin. Inertial migration of a small sphere in linear shear flows, *J. Fluid Mech.* 224, 261-274 (1991).

[46] R. Medrano, A. Moura, T. Tel, I.L. Caldas, and C. Grebogi. Finite-size particles, advection, and chaos: A collective phenomenon of intermittent bursting. *Phys. Rev. E*, 78:056206 (2008).

[47] C.C. Mei and J-L. Auriault, Mechanics of heterogeneous porous-media with several spatial scales, *Proc. R. Soc. London, Ser. A* , 426, 391 (1989).

[48] T. Nizkaya, J.R. Angilella and M. Buès. Note on dust trapping in vortex pairs with unequal strengths. *Physics of Fluids* 22, 113301 (2010).

[49] T. Nizkaya, J.R. Angilella and M. Buès. Transport et accumulation de particules inertielles dans une fracture de rugosité périodique. 20-ème Congrès Français de Mécanique, Besançon - 29 Aout au 2 Septembre 2011.

[50] K. S. Novakowski. The analysis of tracer experiments conducted in divergent radial flow fields. *Water Resour. Res.*, 28(12), 3215-3225, (1992).

[51] K. S. Novakowski and P. A. Lapcevic. Field measurement of radial solute transport in a fractured rock. *Water Resour. Res.*, 30(1), 37-44, (1994).

[52] M. Panfilov, C. Oltean, I. Panfilova, M. Buès. High velocity flow through fractured and porous media: the role of flow non-periodicity. *C. R. Mecanique,* 331, 41-48 (2003)

[53] J. Peng and J. O. Dabiri. Transport of inertial particles by Lagrangian coherent structures: application to predator-prey interaction in jellyfish feeding. *J. Fluid Mech.* vol. 623, pp. 75-84. (2009).

[54] F. Plouraboué, P. Kurowski, J. P. Hulin, S. Roux, and J. Schmittbuhl. Aperture of rough cracks. *Phys. Rev. E*, 51 (3), 1675-1685 (1995).

[55] A. Robinson. On the motion of small particles in a potential field of flow, *Communications on pure and applied mathematics (Vol. IX, pp. 69-84)* (1956).

[56] J. Rubin, C.K.R.T. Jones, and M. Maxey. Settling and asymptotic motion of aerosol particles in a cellular flow field. *J. Nonlinear Sci.*, 5:337–358 (1995).

[57] T. Sapsis & G. Haller. Clustering Criterion for Inertial Particles in 2D Time-Periodic and 3D Steady Flows, *Chaos*, 20 017515 (2010).

[58] P.G. Saffman. The lift on a small sphere in a viscous flow. *J. Fluid Mech.* 22, part 2, 385-400 (1965).

[59] G. Segré, A. Silberberg. Behaviour of rigid macroscopic spheres in Poiseuille flow. Part 2. Experimental results and interpretation. *J. Fluid Mech.* 14, 136-157 (1962).

[60] J.A. Schonberg, E.J. Hinch. Inertial migration of a sphere in Poiseuille flow. *J. Fluid Mech.* 203, 517-524 (1989).

[61] M. Sommerfeld. Analysis of collision effects for turbulent gas-particle flow in a horizontal channel: Part I. Particle transport. *International journal of multiphase flow*, 29(4): 675-699 (2003).

[62] K. D. Stephanoff, I.J. Sobey, B.J. Bellhouse. On flow through furrowed channels. Part 2. Observed flow patterns. *J. Fluid Mech.* **96**, 27 (1980).

[63] P. Tanga, A. Babiano, and A. Dubrulle, B. Provenzale. Forming planetesimals in vortices. *Icarus*, 121:158–170 (1996).

[64] Taylor, G. Dispersion of soluble matter in solvent flowing slowly through a tube, *Proc. R. Soc. London*, Ser. A, 219: 186 (1953).

[65] S. Tsangaris, & E. Leiter. On laminar steady flow in sinusoidal channels. *Journal of Engineering Mathematics*, 18(3214), 89 (1984).

[66] P. Vainshtein, M. Fichman, K. Shuster and C. Gutfinger. The effect of centerline particle concentration in a wave tube. *Journal of Fluid Mechanics* 306, pp. 31-42 (1996).

[67] M. Van Dyke. Slow Variations in Continuum Mechanics. *Adv. Appl. Mech.*, 25 (1987).

[68] P. Vasseur and R. G. Cox. The lateral migration of a spherical particle in two-dimensional shear flows. *J. Fluid Mech.*, 78 : pp 385-413 (1976).

[69] R. D. Vilela and A. E. Motter. Can aerosols be trapped in open flows ? *Phys. Rev. Let.*, 99(264101) (2007).

[70] M. Wilkinson, B. Mehlig. Caustics in turbulent aerosols. *Europhysics Letters*, Vol. 71, N. 2, pp. 186-192 (2005).

[71] M. Wilkinson, B. Mehlig and V. Bezuglyy. Caustic Activation of Rain Showers, *Phys. Rev. Lett.*, 97, 048501 (2006).

[72] H. Zhou, R. E. Khayat, R. J. Martinuzzi & A. G. Straatman. On the validity of the perturbation approach for the flow inside weakly modulated channels. *International Journal for Numerical Methods in Fluids*, 1159 (2001).

[73] R. Zimmerman, G. Bovarsson, Hydraulic conductivity of rock fractures. *Transport in Porous Media*, 23 (1) (1996).